NASA Contractor Report 177598

Tilt Rotor Hover Aeroacoustics

Charles David Coffen

June 1992

National Aeronautics and
Space Administration

NASA Contractor Report 177598

Tilt Rotor Hover Aeroacoustics

Charles David Coffen, Cornell University, Ithaca, NY

June 1992

National Aeronautics and
Space Administration

Ames Research Center
Moffett Field, California 94035-1000

TABLE OF CONTENTS

LIST OF FIGURES

Introduction

Tilt rotor aircraft have great potential for civil aviation applications because of their ability to emulate both helicopters and turboprop aircraft. The tilt rotor may become an efficient mode of commuter transportation by reducing air traffic congestion at major airports via its ability to land and take off in densely populated urban centers. To be successful in this role, the tilt rotor must prove itself to be a 'good neighbor' by meeting FAA standards for noise pollution. In effect, the future of the civilian tilt rotor may be determined by the aircraft's ability to operate quitely in take off, landing and the conversion corridor.

The development and commercialization of tilt rotor aircraft will offer a dynamic new dimension to the improvement of air travel. While the concept of Vertical and Short Take Off and Landing (VSTOL) aircraft is not new, the recent developments in materials technologies, propulsion, and fly by wire systems has made the tilt rotor a technological reality. The maturing of this technology has the potential to produce sweeping changes in the aircraft industry as the demand increases for more specialized commercial aircraft. The jumbo jet as the industry work horse may be replaced by specialized aircraft optimized for well-defined mission performance. This change is already apparent in the renewed interest in supersonic trans-pacific flight and a recent increase in demand for low speed commuter aircraft. Tilt rotor aircraft may help redefine the current world wide air traffic patterns by their ability to operate efficiently in both hover and

forward flight. This makes the tilt rotor ideally suited as a short-to -medium range transport, shuttling passengers to and from densely populated areas. Also, the tilt rotor offers an economic boost to the helicopter industry which will have to adapt to the shrinking demand for military helicopters. The helicopter industry has the opportunity to expand its civil aircraft market by taking the lead in developing this new application of rotary technology. The potential for tilt rotor aircraft is limited only by technological development.

Aeroacoustics, the study of aerodynamically generated sound, has always been important to the growth of the modern aircraft industry. Without past aeroacoustic improvements, commercial jets would not be tolerated. Unacceptably high noise levels in the 1960's resulted in protests by people living near airports. Since then a major emphasis has been on lowering the noise emitted by aircraft. In fact, the Federal Aviation Administration has strict guidelines on aircraft noise emissions, and some airports have even stricter rules limiting the hours and frequency with which certain aircraft may take off and land. This makes an aircraft's far field acoustics a design issue to be considered in the early stages of development.

The tilt rotor is no exception. The far field acoustic signature must be considered in the early design stages in order to develop a commercially viable and competitive aircraft.

However, the design for reduced noise is difficult for any rotor craft as the noise mechanisms are quite complex and not yet completely understood. The difficulty of this analysis stems from the relatively large number of noise mechanism which may be

important for a given design. These mechanisms result from aerodynamic interactions between the rotor, the wake and the air frame. Reducing one mechanism may increase another. Also, various mechanisms affect different parts of the acoustic spectrum. As a result, one needs to understand an array of aeroacoustic mechanisms in order to design quieter aircraft.

Tilt rotor aircraft have several novel features which profoundly affect their aeroacoustic characteristics and therefore, noise reduction potential. Their rotor and rotor/wake aerodynamics are different from either helicopters or conventional aircraft as they operate in and between various helicopter and airplane flight modes. Tilt rotors derive their additional operational modes from their ability to adjust nacelle tilt and balance the required lift between the rotors and wings. Additional adjustments can be made by changing the cyclic pitch and elevators. These additional degrees of freedom create a wide envelope of operations which can be optimized for performance and noise radiation. For example, descent can be accomplished with high or low nacelle tilt, high or low glide slope, and various airspeeds for each condition.

Unfortunately, the wide range of operational geometries and conditions result in almost all aeroacoustic mechanisms being a dominant noise source in some flight regime for some observer angle.

Operational parameters relevant to tilt rotor aeroacoustics include the different paths of the tip vortices in the wake, high disk loading, blade phasing between the two rotors, noise directionality affects due to the orientation of the nacelles with respect to

observers, dynamic blade loadings associated with high blade twist and rapidly changing flow conditions. Perhaps most importantly, the unique tilt rotor aerodynamics results in strong unsteady rotor-wake-body interactions which causes high noise levels in the acoustic far field.

Recently, many studies have been conducted on the broad subject of tilt rotor aeroacoustics. Large amounts of experimental data have been reported which provides analysts with an abundance of high quality data for study and comparison to predictions.

This study is comprised of three main investigations: hover aerodynamics, discrete noise, and broadband noise. The aerodynamics of a hovering tilt rotor are examined experimentally using a 1/12 scale model. The recirculating fountain flow is of primary interest as it has been found to cause an important noise mechanism. The results of the hover flow experiments are used to develop and validate aerodynamic models which are used as inputs to noise prediction codes. Two sets of predictions are developed, one for discrete frequency noise and one for broad band noise. These predictions are compared to experimental data for the XV-15 in hover. Many of the results presented in this thesis have be previously reported in the literature[1,2,3,4].

Chapter I

Relevant Aeroacoustic Theory

Aeroacoustics is the study of aerodynamically generated sound. In the case of tilt rotor sound radiation, which is studied here, the noise is a result of the interaction between the rotor blades and the flow field. This problem can be generalized to the study of the sound field generated by a surface moving through a fluid. In this case, the moving surface is a lifting rotor blade moving in a circular path.

1.1 Ffowcs Williams and Hawkings Equation

The interaction between a moving surface and a fluid can generate sound in several ways. The most obvious mechanism for a lifting rotor is that the surface imparts a force on the fluid due to lift and drag. The force distributed on the surface can be thought of as a pressure on the fluid. If the force varies in time, an unsteady pressure field is generated in the fluid. This phenomenon is known as aerodynamic noise. Another mechanism is due to the fact that the moving surface displaces a volume of fluid equivalent to its own volume as it moves through the flow field. This volume displacement is equivalent to a change in momentum of the fluid. The rate of change of momentum is dimensionally the same as a force acting on the fluid and therefore may generate sound. The last mechanism by which a moving surface may generate sound is by disturbing the flow such that the flow field is no longer

continuous or steady. Examples include shock formation, turbulence and separated flow about surfaces.

These physical mechanisms can be analyzed using some results of Ffowcs Williams and Hawkings[5]. They derived an exact expression for the sound field generated by a surface moving through a moving or stationary fluid. The result is called the Ffowcs Williams and Hawkings equation. The method is sketched as follows:

First consider a volume, V, of fluid with flow velocity u_i. Divide the volume into two regions, 1 and 2, with a surface discontinuity, S, to be identified with a solid body's surface which is moving with some velocity, v_i. Now assume some function, f=0, defines the surface of discontinuity, S, in such a way that f<0 in region 1 and f>0 in region 2. Thus $\delta(f)$, the one dimensional delta function, will be zero everywhere except where f=0. This leads to the the generalized mass equation 2.5 of reference 5.

$$\frac{\partial \overline{\rho}}{\partial t} + \frac{\partial(\overline{\rho u_i})}{\partial x_i} = [\rho(u_i - v_i)]_{(1)}^{(2)} \delta(f) \frac{\partial f}{\partial x_i}. \qquad (1.1)$$

The overbar denotes that the variable is a generalized variable valid throughout V, and u_i is the component of fluid velocity in the x_i direction. The representation $[\ ]_{(1)}^{(2)}$ implies the difference of the contents between regions 2 and 1. This equation shows that satisfying mass conservation between regions 1 and 2 requires a distribution of mass sources on the boundary S. The strength of these sources is the difference between the mass flux requirement

of each region. The generalized momentum equation, equation 2.6 of reference 5, is written in a similar manner:

$$\frac{\partial(\overline{\rho u_i})}{\partial t} + \frac{\partial(\overline{\rho u_i u_j} + \overline{p_{ij}})}{\partial x_j} = [p_{ij} + \rho u_i(u_j - v_j)]_{(1)}^{(2)} \delta(f) \frac{\partial f}{\partial x_j} \tag{1.2}$$

p_{ij} is the compressive stress acting on the fluid. Note that if the surface of discontinuity, S, is removed, these two equations reduce to continuity and momentum equations for compressible inviscid flow.

These forms of the continuity and momentum equations can be applied to sound generation by a moving surface by taking region 1 to be the region of the fluid inside S. Inside this control volume, the fluid is assumed to be at rest, with density ρ_0 and pressure p_0. p_{ij} has the same mean value, $p_0\delta_{ij}$, on either side of the surface and therefore its derivative is zero. Redefine p_{ij} to be the difference of the stress tensor from its mean value. Then $p_{ij} = 0$ in region 1 where the fluid is at rest. For an impermeable moving surface of discontinuity such as a rotor blade, $u_n = v_n$ where n is the unit normal out of the surface from region 1 to 2. Thus in region 2 the mass and momentum conservation rules can be written as (equation 2.7 of reference 5):

$$\frac{\partial \overline{\rho}}{\partial t} + \frac{\partial(\overline{\rho u_i})}{\partial x_i} = \rho_0 v_i \delta(f) \frac{\partial f}{\partial x_i}, \tag{1.3}$$

$$\frac{\partial(\overline{\rho u_i})}{\partial t} + \frac{\partial(\overline{\rho u_i u_j + p_{ij}})}{\partial x_j} = p_{ij}\,\delta(f)\,\frac{\partial f}{\partial x_j}. \qquad (1.4)$$

The inhomogeneous wave equation, equation 2.8 of reference 5, for sound generated by the moving surface is found by eliminating $\overline{\rho u_i}$ from the above two equations.

$$\left(\frac{\partial^2}{\partial t^2} - \frac{\partial^2}{\partial x_i^2}\right)\left(\overline{\rho-\rho_0}\right) = \frac{\partial^2 \overline{T_{ij}}}{\partial x_i \partial x_j} - \frac{\partial}{\partial x_i}\left(p_{ij}\,\delta(f)\frac{\partial f}{\partial x_j}\right) + \frac{\partial}{\partial t}\left(\rho_0 v_i\,\delta(f)\frac{\partial f}{\partial x_i}\right) \qquad (1.5)$$

The dependent variable has been changed to the generalized density perturbation, $\overline{\rho-\rho_0}$, which is a measure of the acoustic sound amplitude. $\overline{T_{ij}}$ is the Lighthill stress tensor, $T_{ij} = \rho u_i u_j + p_{ij} - c^2(\rho-\rho_0)\delta_{ij}$, outside the surface and zero within the surface. Sound generation due to the $\overline{T_{ij}}$ term is generally related to high Mach number turbulent flows or to shock waves. It is not considered in this study of tilt rotor aeroacoustics as it is a less important mechanism for a hovering tilt rotor.

Equation 1.5 is an exact expression for the sound generation and propagation in a compressible inviscid fluid. This expression shows that sound is generated by a surface moving through a fluid by three mechanisms. The T_{ij} term represents acoustic quadrupoles distributed throughout the region exterior to the surface of discontinuity. This term includes such flow phenomenon as shocks and separated flow. The other two mechanisms are relevant to the tilt rotor noise mechanisms studied here. The p_{ij} term can be

interpreted as a distribution of acoustic dipoles on the surface of a discontinuity. Likewise, the $\rho_0 v_i$ term can be interpreted as surface distribution of acoustic monopoles. The dipole distribution is a result of the force acting on the fluid generated by the surface, and the monopole distribution is due to the displacement effect of the surface moving through the fluid. These effects require a source distribution which varies with time, space, or both in order to generate sound.

1.2 Solution to the Inhomogeneous Wave Equation

Equation 1.5 can be expressed more generally as an inhomogeneous wave equation of the form:

$$\frac{\partial^2 \rho}{\partial t^2} - \frac{\partial^2 \rho}{\partial x_i^2} = g(\underline{x},t) \qquad (1.6)$$

where ρ is redefined as the perturbation density, $\rho - \rho_0$. $g(\underline{x},t)$ is the forcing term and represents the right hand side of the Ffowcs Williams Hawkings equation, equation. 1.5. $\rho(\underline{x},t)$ can be found from this equation by using the Green's function method. The formal solution of the inhomogeneous wave equation is:

$$\rho(\underline{x},t) = \int_V dV \int_{-\infty}^{+\infty} g(\underline{x},t) \cdot G \; d\tau \qquad (1.7)$$

where G is the free space Green's function,

$$G = \frac{\delta\left(\tau - t + \frac{r}{c_0}\right)}{4\pi c_0^2 r}. \qquad (1.8)$$

V is the volume enclosing the fluid and can be considered to be of infinite extent. The observer distance, r, is the distance between the observer and source. The mean speed of sound, c_0, is based on ambient conditions. The variable τ is a dummy variable of integration and t is the observer time.

Using the properties of the Dirac delta function, the integration over τ can be carried out giving:

$$\rho(\underline{x},t) = \int_V \left[\frac{g(\underline{x},t)}{r}\right] dV. \qquad (1.9)$$

Here square brackets indicate evaluation of the argument at the retarded time, τ. $\tau = t - \frac{r}{c_0}$. Replacing $g(\underline{x},t)$ with the right hand side of equation 1.5 and recognizing that $\delta(f)$ is zero everywhere but on the surface of discontinuity gives:

$$4\pi c_0^2 \rho(\underline{x},t) = \frac{\partial^2}{\partial x_i \partial x_j} \int_V \left[\frac{T_{ij}}{r|1-M_r|}\right] dV(\eta) - \frac{\partial}{\partial x_i} \int_S \left[\frac{p_{ij} n_j}{r|1-M_r|}\right] dS(\eta)$$
$$+ \frac{\partial}{\partial t} \int_S \left[\frac{\rho_0 v_n}{r|1-M_r|}\right] dS(\eta). \qquad (1.10)$$

where v_n is the normal component of velocity of the surface of discontinuity S, M_r is the component of the source Mach number in the observer direction and V represents the volume of infinite extent surrounding S. The surface integrals are integrated with respect to the Lagrangian coordinates η which move with the surface S.

1.3 Application to Tilt Rotor Aeroacoustics

The far field acoustics of the tilt rotor due to direct surface (rotor) fluid interactions (force and displacement mechanisms) can be found by integrating:

$$4\pi c_0^2 \rho(\underline{x},t) = -\frac{\partial}{\partial x_i}\int_S \left[\frac{p_{ij}n_j}{r|1-M_r|}\right] dS(\eta) + \frac{\partial}{\partial t}\int_S \left[\frac{\rho_0 v_n}{r|1-M_r|}\right] dS(\eta). \tag{1.11}$$

over the surface of the rotor blade at the retarded times. The most popular method for doing this integration is a numerical integration over a collapsing sphere. Consider a sphere centered on the observer with some large radius. Collapse the sphere toward the observer such that the radius decreases at a rate equal to the speed of sound. The integrands contribute to the acoustic signal only when the surface of the sphere intersects the surface of discontinuity, S.

This integration technique presupposes that p_{ij}, $\rho_0 v_n$, the surface geometry, and the motion of the surface are known a priori.

Unfortunately, this is generally not the case. For the tilt rotor, p_{ij} is the pressure distribution on the surface of the rotor blade (due to lift and drag), and $\rho_0 v_n$ is the momentum flux due to the fluid displacement by the rotor blade. S is defined by the rotor blade geometry and while the motion for a hovering rotor is circular in general, it may have perturbation motions due to flapping, lead-lag, and feathering. For rotor noise in general, the terms of interest are referred to as:

blade loading noise: $$\frac{\partial}{\partial x_i}\int_S \left[\frac{p_{ij}n_j}{r|1-M_r|}\right] dS(\eta) \qquad (1.12)$$

blade thickness noise: $$\frac{\partial}{\partial t}\int_S \left[\frac{\rho_0 v_n}{r|1-M_r|}\right] dS(\eta) \qquad (1.13)$$

Consequently, the solution to the tilt rotor acoustics problem reduces to an aerodynamic and computational problem. The thickness noise is purely a function of the blade geometry and motion which are determined by the operating parameters of the rotorcraft. The geometry is assumed to be known and blade motions can be simplified in the hover configuration by neglecting aeroelastic effects.

The loading noise for a blade with constant lift translating in a fluid at rest is zero. For a rotating blade with constant lift, sound is radiated due to the acceleration of the steady force. The case of the hovering tilt rotor is complicated because the blade is rotating

through a 'random' turbulent flow field superposed on a time-mean flow field which is itself spatially varying due to the partial ground plane effect of the wing beneath the rotor. This results in a non-deterministic blade loading superposed on a spatially varying mean lift distributed over the surface of the moving blade.

The spatially varying mean loading, rotor geometry and rotor motions can be modelled mathematically based on aerodynamic theory and then used to evaluate the integrals of equation 1.11. Chapter II studies the aerodynamics of a hovering tilt rotor and Chapter III uses these results to develop the required mathematical models for evaluation of equation 1.11 based on mean quantities.

However, the random loading noise of the blade cannot be evaluated using the Ffowcs Williams and Hawkings equation directly. The random loading due to the turbulent flow field cannot be defined as a deterministic function of space and time. Other aeroacoustic methods must be used to calculate the random, or broad band, loading noise. In general, this problem is solved in the frequency domain by calculating the power spectral density of the acoustic pressure fluctuations. Tilt rotor broad band noise prediction methods are described in Chapter IV.

Chapter II
Tilt Rotor Hover Aerodynamics

This chapter details the results of flow visualization studies and inflow velocity field measurements performed on a 1/12 scale model of the XV-15 tilt rotor aircraft in the hover mode. The complex recirculating flows were studied visually using neutrally buoyant soap bubbles and quantitatively using hot wire anemometry. Still and video photography were used to record the flow patterns. This work was previously presented in a paper by Coffen, George, Hardinge, and Stevenson at the 1991 Technical Specialists Meeting of the American Helicopter Society[1].

2.1 General Tilt Rotor Aerodynamics

In the operation of a tilt rotor aircraft in hover, the presence of the wing and fuselage beneath the rotor affects the aerodynamics by introducing complex unsteady recirculating flows. The fundamental geometry of the tilt rotor aircraft, shown in figure 2.1a-b, consists of prop-rotors mounted on tiltable nacelles which are located at or near the tips of a fixed (non-tilting) wing. The prop-rotor is sufficiently large so that the benefits of low disk loading are gained for efficient hover flight. The prop-rotor is designed to provide the desired performance balance between the axial-flow hover requirement and the axial-flow airplane mode requirement[6,7,8]. The tilt rotor introduces a number of unique prop-rotor/airframe aerodynamic interactions that must be addressed to properly understand the significant performance

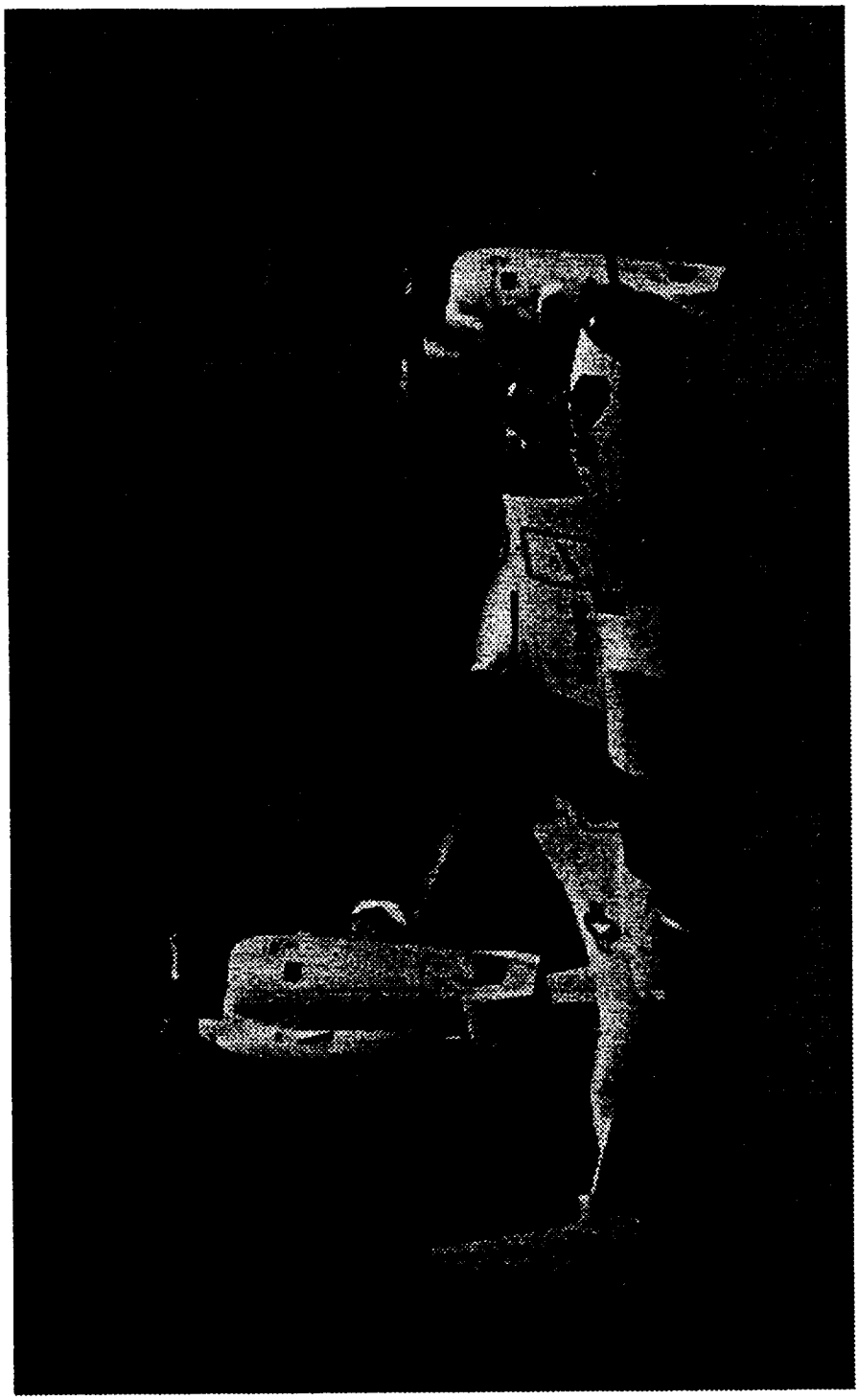

Figure 2.1a Tilt rotor hover configuration.

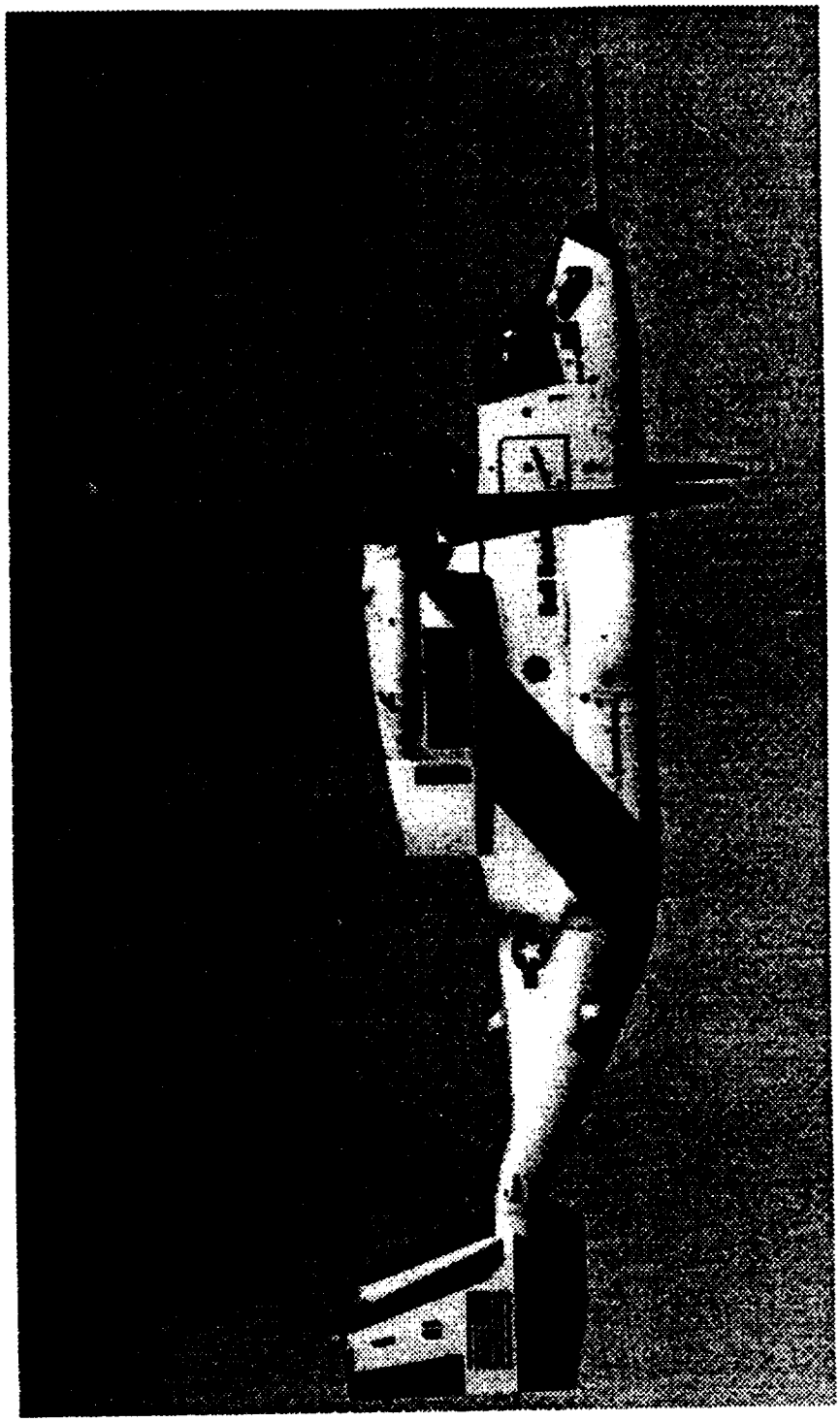

Figure 2.1b Tilt rotor forward flight configuration.

issues. In hover mode the wing and fuselage provide a partial ground plane in the near wake which causes the development of an inboard-bound spanwise flow over the wing and fuselage surface. At the aircraft's longitudinal plane of symmetry, the opposing flows collide, producing an unsteady "fountain flow" with upward velocity components which is then reingested by the rotors. Full analytical representation of this flow would require a three dimensional, time varying, turbulent, rotor/rotor, and rotor/airframe interaction model.

Some characteristics of tilt rotor flows have been studied both experimentally and analytically. Experimental tests on large and full scale models have been used to study the down load on the wing in the hover condition[9,10,11,12,13]. This problem is of great interest as 10%-15% of the rotor lift is needed to overcome the down force on the wing caused by the downwash flow over the wing. All of these tests used one wing and rotor and an image plane rather than a complete mock up. According to the study by Felker and Light[13] the size of the image plane can have a profound effect on the test results. One previous experimental study of the tilt rotor hover condition not limited to downwash and down loads was by Rutherford[14]. In this test smoke and tuft flow visualization techniques were used on a model consisting of a single wing and rotor. An image plane was used to simulate the two rotor/wing flow phenomena.

The study by Fejtek and Roberts[15] attempts to analytically study the flow of a tilt rotor XV-15 in hover by numerically solving the unsteady, thin layer compressible Navier-Stokes Equation.

While the results of this study are encouraging, not all the major features of tilt rotor hover flow are captured in the computation. In particular, this study included only a wing and rotor image system in the calculation. Attempts at modeling tilt rotor hover flow by assuming a plane of symmetry and disregarding the fuselage will be shown here to be insufficient.

While a full analytical representation may be desirable in the long term, a more expedient method is required for generating data needed for current aerodynamic and aeroacoustic calculations and design. Thus a 1/12 scale model (consisting of two rotors, wing, and fuselage) of the XV-15 tilt rotor was built in order to determine and quantify the complex flows about a hovering tilt rotor. This model enables the study of the unsteadiness and the side to side shifting of the fountain flow which were found to occur. These phenomena had not been previously explored as prior tests had relied on an image plane to simulate the tilt rotor hover configuration and had also excluded the fuselage. The present results show important flow phenomenon along and above the length of the fuselage. Also, attempts to model the flow analytically require accurate and complete experimental information for comparison and validation. Previous tests had not been adequate in this respect.

2.2 Experimental Setup

The scale of the model was determined by the size of the largest commercially available model propeller, which was 24 inch diameter with a pitch of 8 inches. Electric motors were chosen to power the model. No attempt was made to Mach scale the rotor tip

speed. As the rotor pitch and twist were scaled approximately, the ratio of tip speed to induced velocity will be approximately scaled. Most fixed speed electric motors operate at either 1700 or 3450 rpm. In order to obtain higher inflow velocities (less relative error for the measuring equipment available), a motor speed of 3450 rpm was chosen. Two 1.5 hp motors were used. The motors were uncoupled as coupled motors would have been difficult to implement and maintain. The uncoupled motors were operated at the same speed by controlling one motor's speed with a variac and matching speeds with a stroboscope. We do not expect that the lack of phase locking between the rotors will be significant as the rotor tip speed is much greater than the induced velocity giving many tip vortices and associated wake structures per unit axial length. The motors spin in opposite directions so that the blades rotate towards the tail as they pass over the wing, as in the actual aircraft. The motors are located approximately 7 inches below the wing, far enough below the rotors to be out of the flow yet not so far as to make shaft whirl a problem.

The wing and fuselage were both constructed using a styrofoam base covered with fiberglass, filler and paint. The horizontal and vertical tail were not installed in the tests reported here. The wing is removeable and has adjustable flaps and flaperons to allow for testing of various wing configurations. The model is mounted on a steel frame to withstand the lift of the rotors and reduce vibration. The model is supported by a wooden structure elevated above the floor such that the rotor plane is 60.75 inches above the ground. This corresponds to a hover height of

Figure 2.2 Photo of the 1/12 scale tilt rotor showing model, motors and mounting.

60.75 scale feet. Figure 2.2 shows the the experimental set up including the model, electric motors and test stand. The model was operated in an area of dimensions greater than 25 feet. The nearest significant objects in the room were approximately 10 feet away. The orientation and placement of the model in the room was found not to affect the observed and measured flow.

2.3 Flow Visualization

A bubble generator is a very effective tool for visualizing the complex flows of the model XV-15. The Model 3 Sage Action Incorporated Bubble Generator combines compressed air, helium, and a soap solution to produce neutrally-buoyant helium filled bubbles[16]. The bubbles follow the pathlines of the flow and are able to accurately trace the intricate flow patterns of the hovering tilt rotor. Rubber tubing and an aluminum tube wand were used to insert the bubbles at various locations in the flow. During the experiment, the room was darkened and a high intensity Varian arc lamp was used to illuminate the bubbles.

2.3.1 Results of Still Photographs

The flow around a hovering tilt rotor is extremely unsteady. Still photographs were used to capture various features of the flow. It must be noted that these are instantaneous visualizations. ASA 1600 film was used, with an f-stop of 5.6, and 0.25 to 1.0 second exposure times. Greater exposure times produced pictures with too many 'cluttered' pathlines and smaller exposure times did not allow enough light. Still photographs were taken of the front and side of

the model. Unless otherwise obvious, the bubbles were inserted in the longitudinal plane of symmetry. In order to view a two dimensional slice of the the flow patterns, the light source was situated perpendicular to the direction of the camera.

Figure 2.3 is a top view schematic of the model and indicates the aircraft axis and probe locations for the various experiments.

The images presented here are computer enhancements of the original stills which were digitized using a scanner. Figure 2.4 shows an unenhanced photo. Figure 2.5 is the same photo which has been inverted (negative image) to show the pathlines as black streaks on a white background. The contrast of the scanned images was improved to better define the bubble streaks. This process often caused a blurring of the model with the background. Also, light reflected off the model caused distracting shadows and in many cases obliterated the outline of the model. In order to reduce this annoying affect, the outline of the model was enhanced and the background edited to clarify the image and remove distracting shadows. In no cases were the bubble streaks or any part of the flow embellished or edited.

Figure 2.5 is a head on photo of the model with the bubbles being injected directly over the intersection of the longitudinal axis and the rotor/rotor axis. This figure clearly shows the recirculating fountain and indicates the height of the fountain to be approximately 1/2 the radius of the rotor. This figure also shows an unsteady stagnation point on the fuselage where the spanwise flows intersect and erupt up between the two rotors and are then reingested. Figure 2.6 emphasizes the reingestion part of the flow

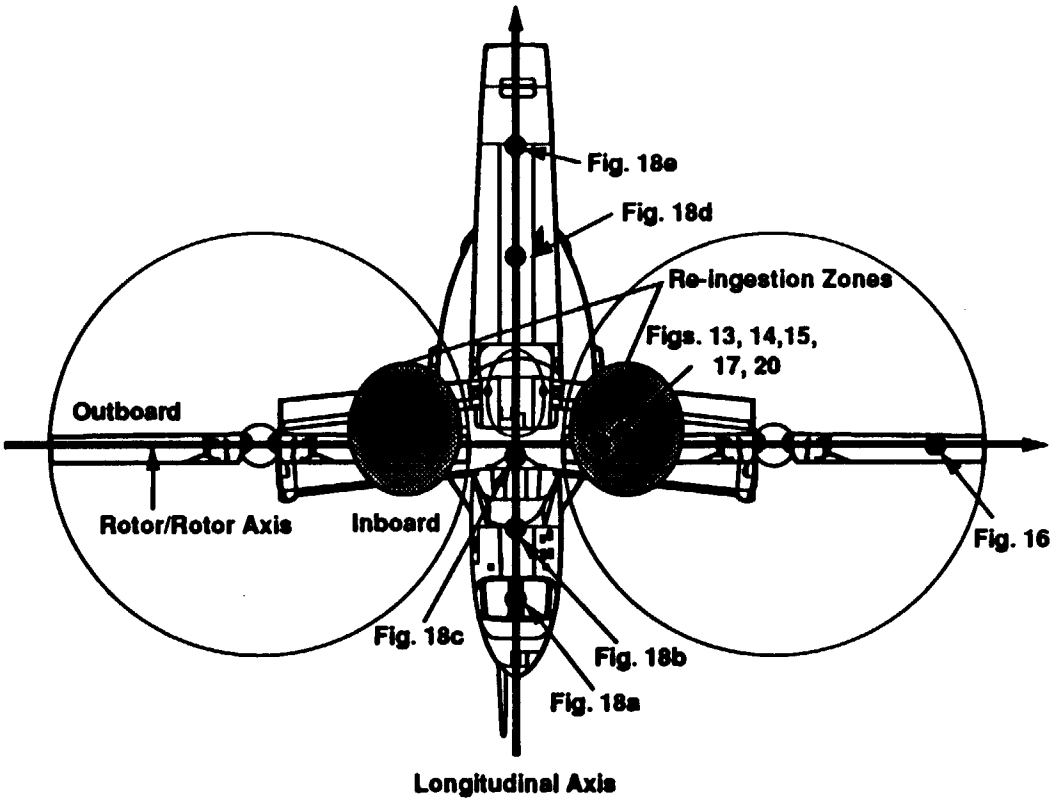

Figure 2.3 Schematic of model top view showing probe placements, axes, and approximate re-ingestion zones.

Figure 2.4 Unenhanced digitized photo of fountain flow. Viewer in front of model. Bubbles are injected over the center of the wing on the rotor/rotor axis. 1/2 second exposure time.

Figure 2.5 Computer enhanced digitized photo of fountain flow. Viewer in front of model. Bubbles are injected over the center of the wing on the rotor/rotor axis showing spanwise flow, fountain height, and recirculating flow. 1/2 second exposure time.

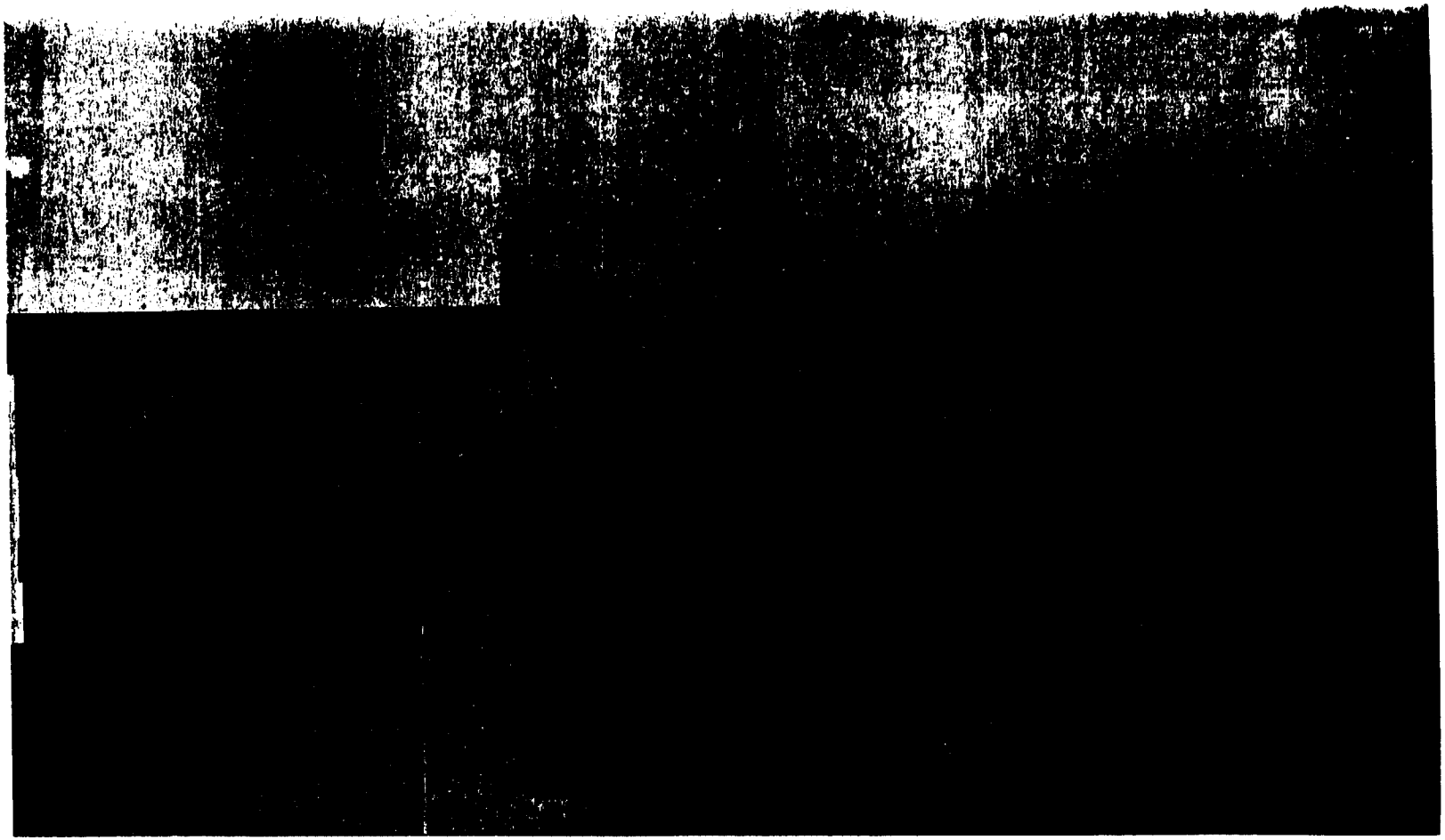

Figure 2.6 Computer enhanced digitized photo of fountain flow. Viewer in front of model. Bubbles are injected into the stagnation region on the center of the wing on the rotor/rotor axis showing up-flow between rotors and recirculating flow. 1/2 second exposure time.

Figure 2.7 Computer enhanced digitized photo of fountain flow. Viewer in front of model. Bubbles are injected into the stagnation region on the center of the wing on the rotor/rotor axis showing highly turbulent up-flow between rotors and recirculating flow. 1/2 second exposure time.

Figure 2.8 Computer enhanced digitized photo of fountain flow. Viewer in front of model. Bubbles injected right of center over the rotor/rotor axis showing the unsteady asymmetric nature of the fountain. 1/4 second exposure time.

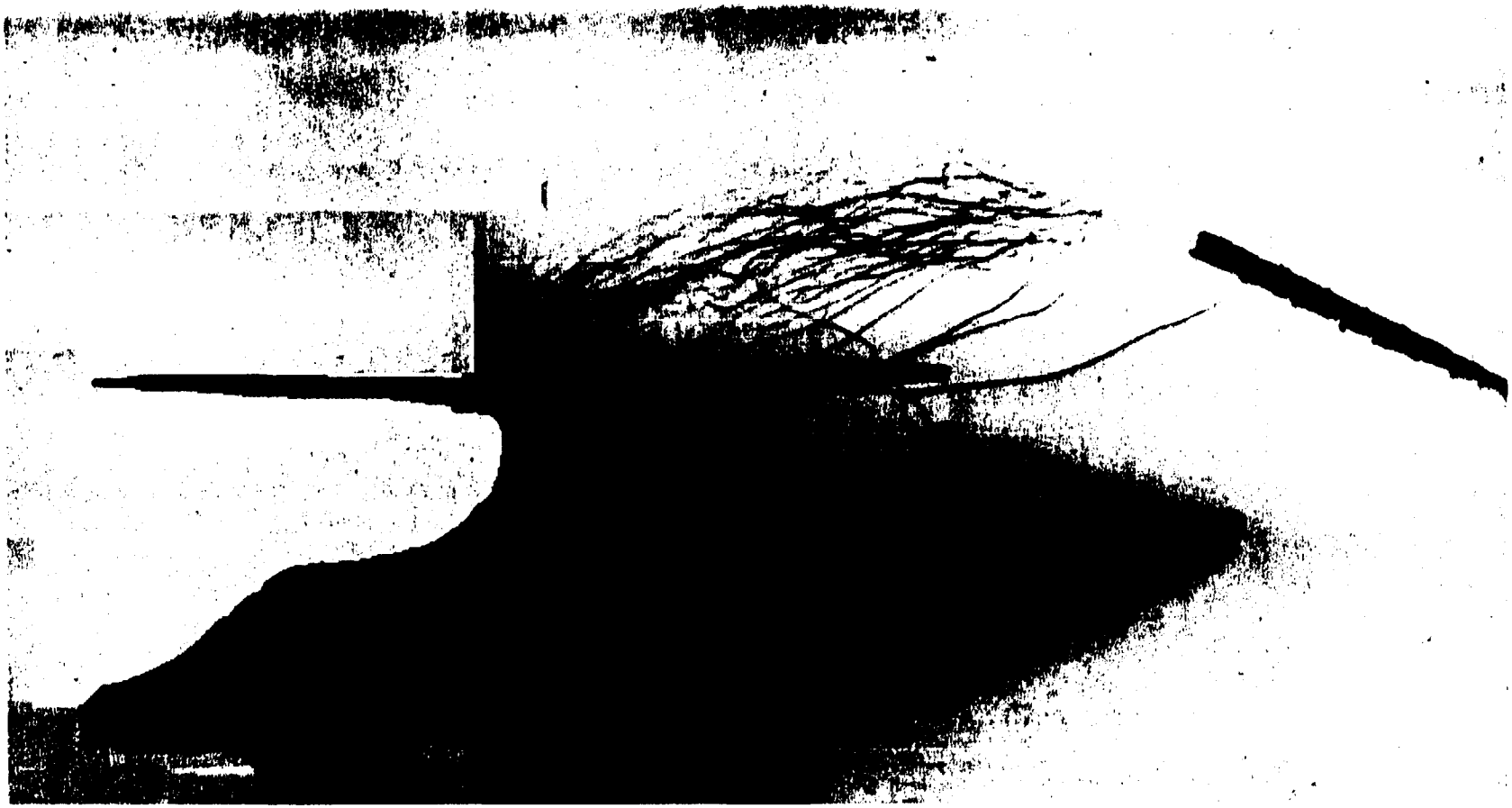

Figure 2.9 Computer enhanced digitized photo of fountain flow. Viewer to side of model. Bubbles are injected above rotor plane over the longitudinal axis showing the longitudinal recirculating flow. 1/2 second exposure time.

Figure 2.10 Computer enhanced digitized photo of fountain flow. Viewer to side of model. Bubbles are injected along the fuselage showing the turbulent up-flow over the length of the fuselage. 1/2 second exposure time.

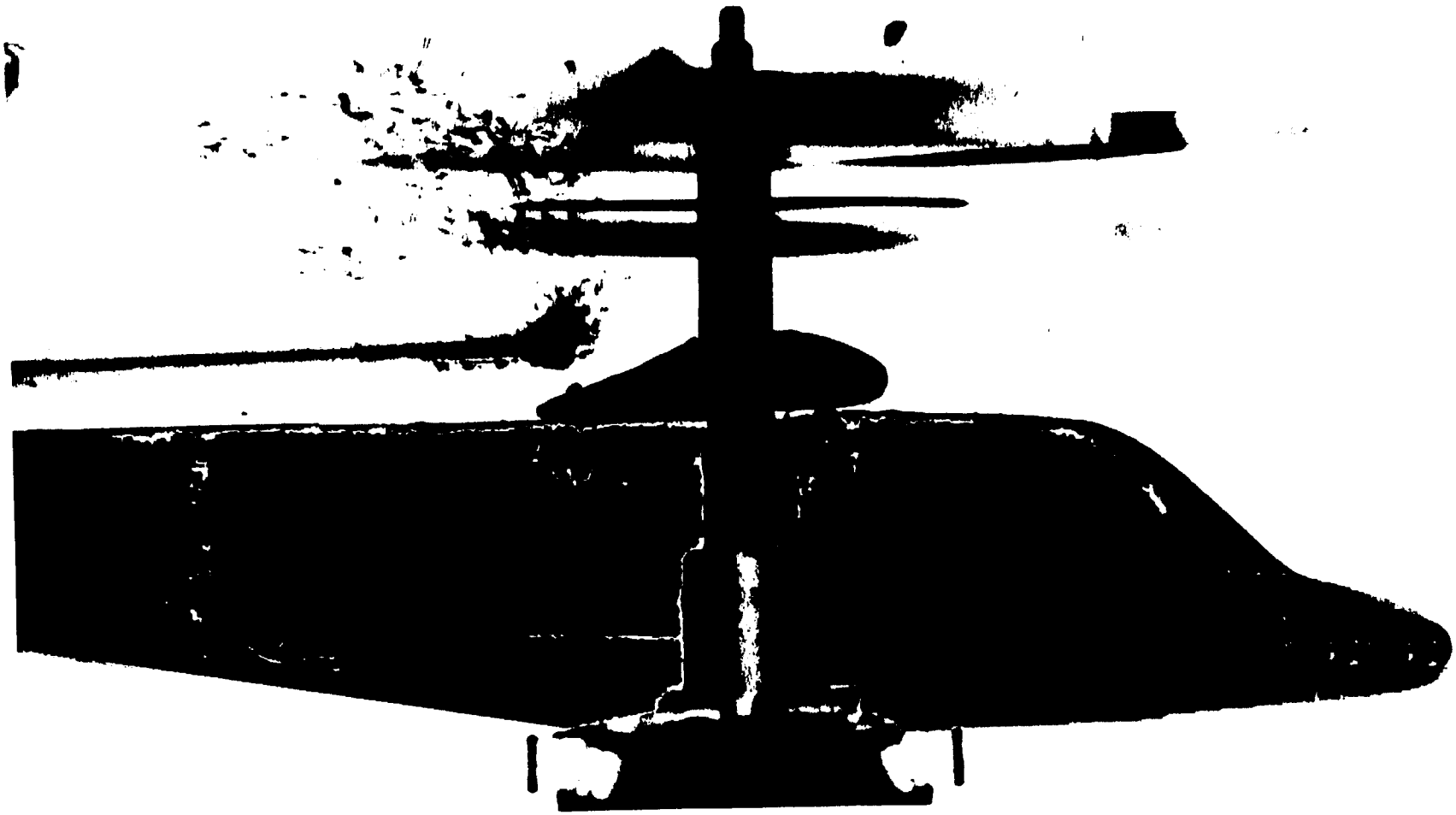

Figure 2.11 Computer enhanced digitized photo of fountain flow. Viewer to side of model. Bubbles are injected just above the wing on the longitudinal axis showing the recirculating flow being swept rearward.

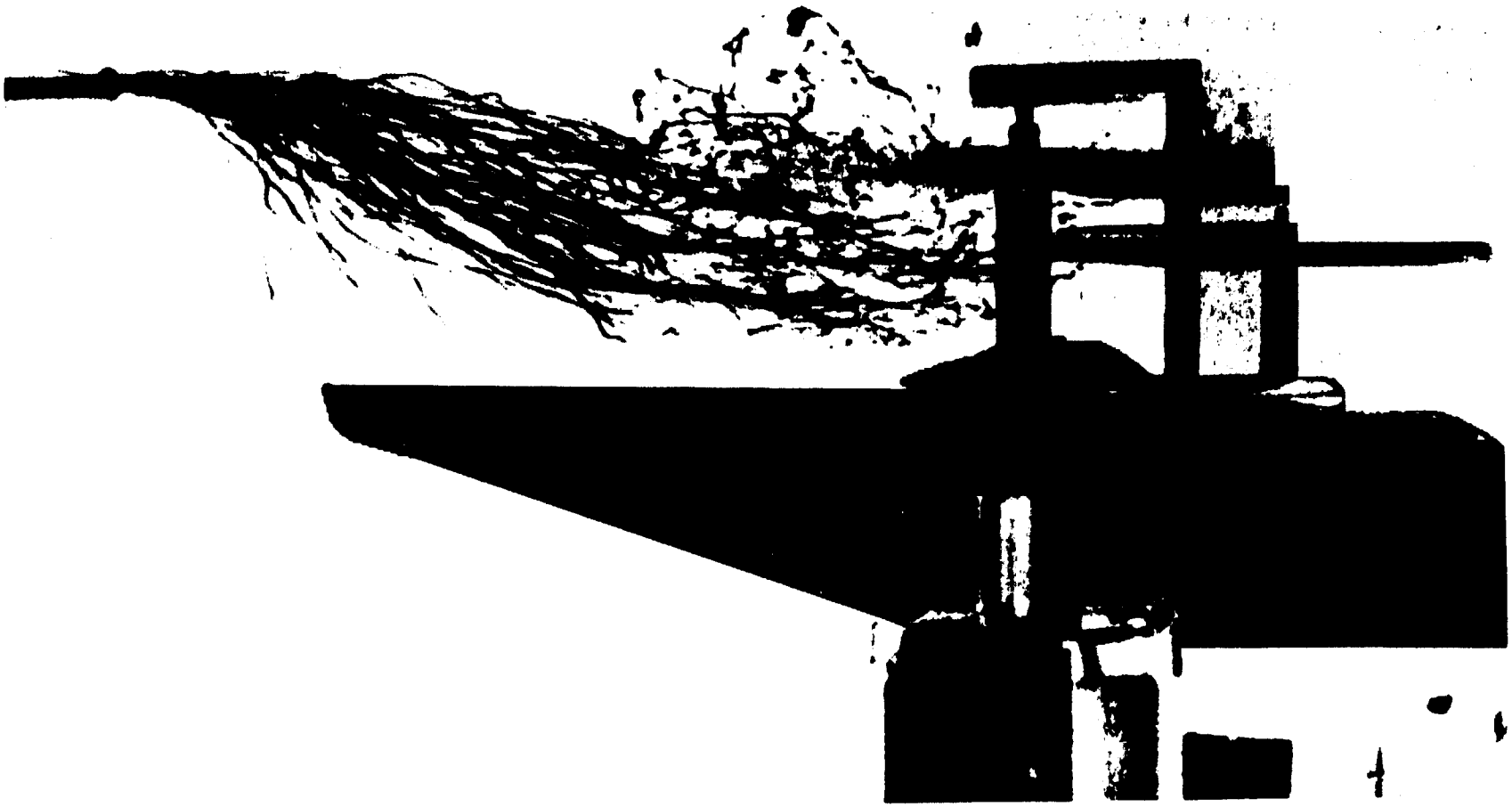

Figure 2.12 Computer enhanced digitized photo of fountain flow. Viewer to side of model. Bubbles are injected above the rotor plane, behind the tail and over the longitudinal axis, and show laminar inflow becoming turbulent as it encounters the fountain flow.

as bubbles inserted just above the unsteady stagnation point are convected up between the rotors where they are entrained into the induced flow and are reingested. Figure 2.7 indicates the extremely turbulent nature of the fountain flow near the unsteady stagnation point. Here bubbles are injected horizontally along the longitudinal axis. The random direction of the pathlines, the sharp lateral perturbations, and the fact that the bubbles are injected at the same location in the flow and follow completely dissimilar paths, all indicate the highly unsteady and turbulent nature of the fountain flow. Note that all of these images project the 3-D flow onto a plane and that information about the flow out of the plane is lost. Figure 2.8 shows bubbles being injected off center and shows the spanwise flow curling up before reaching the longitudinal axis. This figure also shows one bubble being convected from the center of the fountain into the interior of the rotor disk and another being convected into the opposite rotor. Presumably these events are due to particularly large turbulent eddies being ingested.

The next four figures, figures 2.9-2.12, illustrate the fountain flow from the side and clearly illustrate the multi-dimensional nature of the recirculating fountain flow. These aspects of the flow are difficult to explain as the images show several recirculation paths. Note that the model used in this study did not include a tail wing assembly which may have some minor influence on the fountain flow over the rear of the fuselage.

The pathlines of the bubbles over the rear of the fuselage depend strongly on their point of injection. Figure 2.9 shows bubbles being injected above the tail, over the longitudinal axis, and

above the rotor plane. The bubbles are swept horizontally along the longitudinal axis and are ingested into the rotors to both sides of the upflow shown in Figure 2.5. The bubbles pass through the rotor plane and travel back towards the tail along the fuselage. Here the bubbles recirculate upward above the rotor plane and are eventually reingested. Figure 2.10 shows the bubbles being injected along the fuselage near the tail. This photo differs from the one above in that the bubbles are injected below the rotor plane. The bubbles are lifted off the fuselage and are entrained in the recirculating flow along and above the fuselage. Figure 2.11 shows what happens when bubbles are injected over the wing, over the longitudinal axis, and below the the rotor. This probe placement is similar to that of figure 2.6 but the photo is from a different view. Here the bubbles are convected up between the rotors and are dispersed rearward and to one or the other side of the fuselage where they are reingested. Figure 2.12 demonstrates how the near laminar inflow becomes distorted and erratic as it interacts with the recirculating fountain flow over the fuselage. Unlike the coherent flow structures provided by the head on photos, these images do not indicate any distinct flow pattern which can be said to characterize the flow above the fuselage. Most likely, the entire region from the wing/fuselage intersection rearward on the fuselage represents an unsteady stagnation zone. This flow is characterized by low velocity highly turbulent flow. The flow along the fuselage tends to be entrained up between the two rotors and reingested through the rotors in a cyclical process. The pathlines are dependent on the point of origin, but it appears that bubbles

injected anywhere above the fuselage may eventually enter this stagnation zone and become reingested.

The most important conclusion that can be drawn from these photos is that the fountain is not a phenomenon which can be viewed or analyzed in two dimensions. This flow is multi-directional and includes spanwise flow along the wings and unsteady flow along the fuselage. Both of these components exhibit turbulent upward flow paths which result in reingestion of the flow.

2.3.2 Results of Video Recording

In order to record the strong time dependence of the flow, video recordings of the bubble pathlines were also made. Bubbles were inserted in various places in the flow to show various pathlines. The location of insertion point is very important for visualizing different flow phenomenon. One important feature of the video recordings is the availability of slow motion and frame-by-frame advance. The downwash velocities are fast enough to make it difficult for the human eye to see all there is to see in the video at standard speeds. The frame-by-frame advance shows 0.04 second intervals. Between frames, the pathlines disappear and new pathlines appear as bubbles move in and out of the stream of light. This demonstrates the gross unsteadiness in the flow and demonstrates the 3-dimensional nature of the flow. This is an important point because the recorded images show the fountain flow superimposed on a 2D plane. In fact, the fountain flow is omni-directional and must be studied from all angles in order to fully appreciate the complexity of the flow.

Another important phenomenon of the flow documented with video was the side-to-side switching of the fountain. This effect is most apparent when the model is viewed head on and bubbles are injected above the rotor plane. The recirculating flow is seen to switch randomly from side to side in time. The time scale of this phenomenon was measured to be anywhere from 0.04 seconds or less (frame advance time) to 0.75 seconds. The fluctuation is characterized by the fountain flow being reingested mostly into one of the two rotors. This switching indicates the unsteadiness of the stagnation region on and above the fuselage. The asymmetry of this phenomenon shows that modeling the fountain flow with one rotor and an image plane is inadequate for studying the time varying properties of the flow.

2.4 Hot Wire Experiments

Hot wire anemometry was another technique used to help characterize the fountain flow. These experiments were conducted with a single wire probe. Unless otherwise indicated, the wire was parallel to the plane of the rotor and was oriented parallel to the longitudinal axis. The anemometer was connected to a Macintosh based data acquisition system. Three experiments are reported. The first experiment was an attempt to characterize the unsteadiness of the flow by examining time traces of velocity measurements. For these measurements, a sampling rate of 4000 samples per second for one second was used. Another experiment was to measure the spectrum of turbulence due to the recirculating fountain. For this experiment the sampling rate was 30,000

samples per second. 2^{14} evenly spaced samples were used to find the spectrum. The last experiment was an attempt to quantify the mean and rms inflow velocities over the rotor plane. The mean velocity spatial variations are affected by the wing obstructing the rotor wake, and the rms velocity spatial variations are affected by the reingestion of the fountain turbulence. 625 locations one inch above the rotor plane were measured. A sampling rate of 40 samples per second for 15 seconds was used.

2.4.1 Time Traces

The unsteadiness of the location and turbulent intensity of the fountain flow is evident from time traces of velocity at various points in the flow. figure 2.13a-b compare two 0.13 second time series of inflow velocity measured 2 inches from the tip on the rotor/rotor axis and one inch above the rotor plane (in the fountain reingestion zone of the rotor). Refer to figure 2.3 for a schematic of the model and measurement locations. Based on the results of the flow visualization study, this location was chosen as a reference point because it is more or less centered in the reingestion area. These series show how the inflow can be either intermittently laminar, essentially showing only the blade passing, figure 2.13a, or very turbulent, figure 2.13b, due to reingestion of the wake. Figure 2.14 gives an example of the intermittency of the phenomenon as this sample shows a nearly laminar inflow broken by a 0.05 second burst of turbulence followed by a return to laminar flow. A study of a 4.0 second series, figure 2.15, did not indicate any discernable pattern in the period of intermittency. Figure 2.16 shows a time

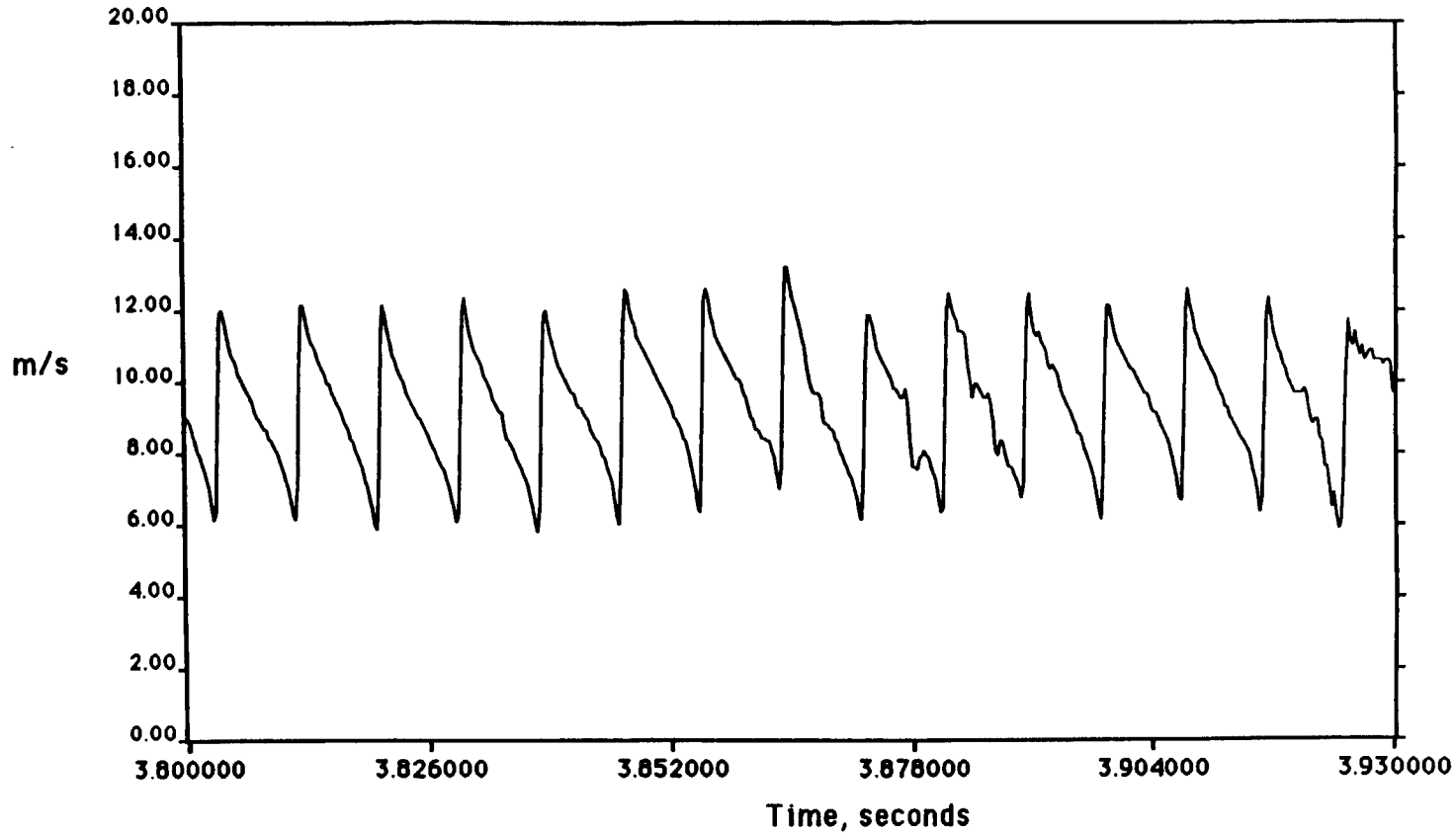

Figure 2.13a Time trace of inflow velocity in the fountain re-ingestion zone showing essentially laminar flow. Data taken with the hot wire parallel to the longitudinal axis, inboard, 2 inches from the rotor tip on the rotor/rotor axis, and 1 inch above the rotor plane.

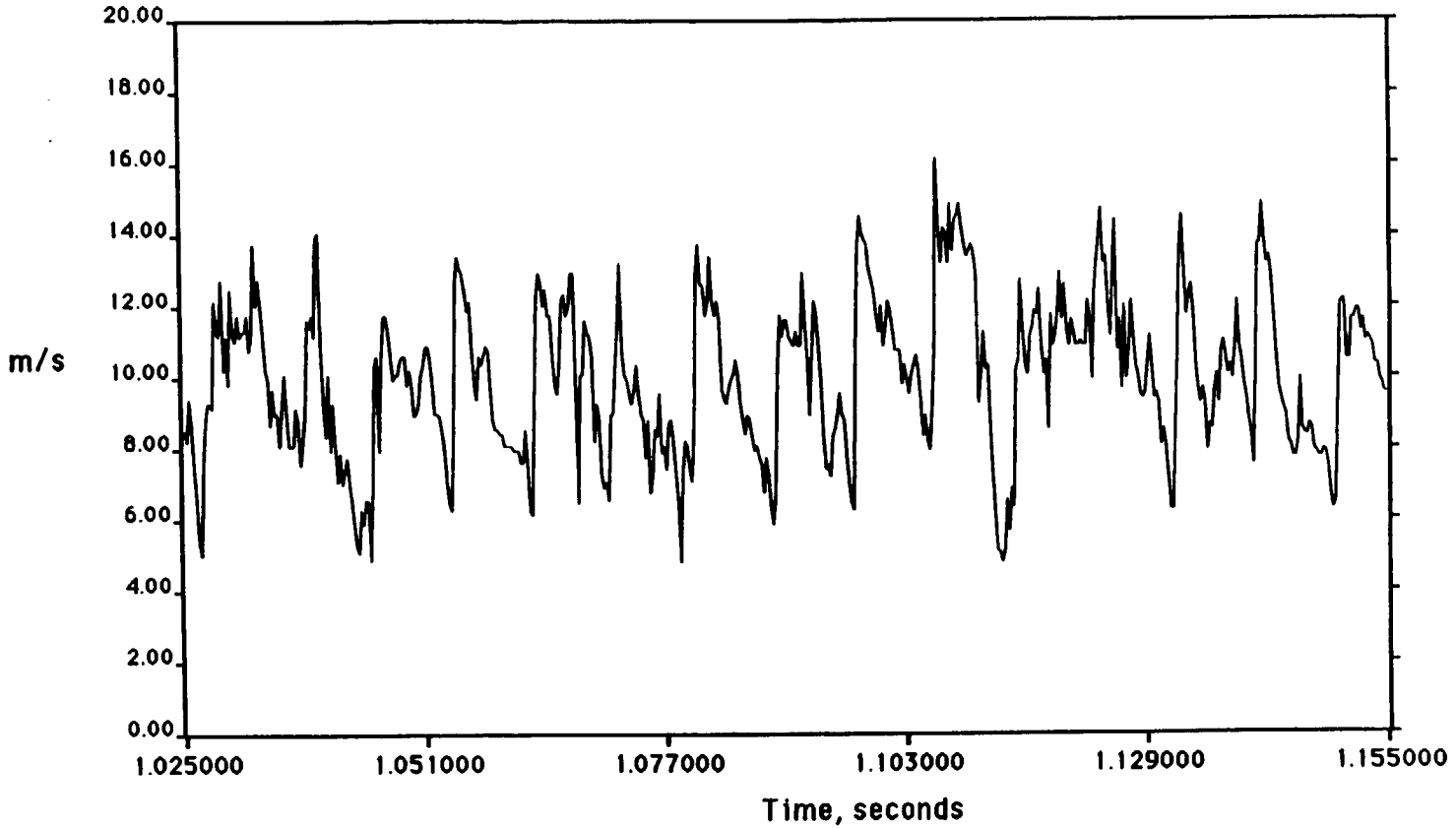

Figure 2.13b Time trace of inflow velocity in the fountain re-ingestion zone showing turbulent flow. Data taken with the hot wire parallel to the longitudinal axis, inboard, 2 inches from the rotor tip on the rotor/rotor axis, and 1 inch above the rotor plane.

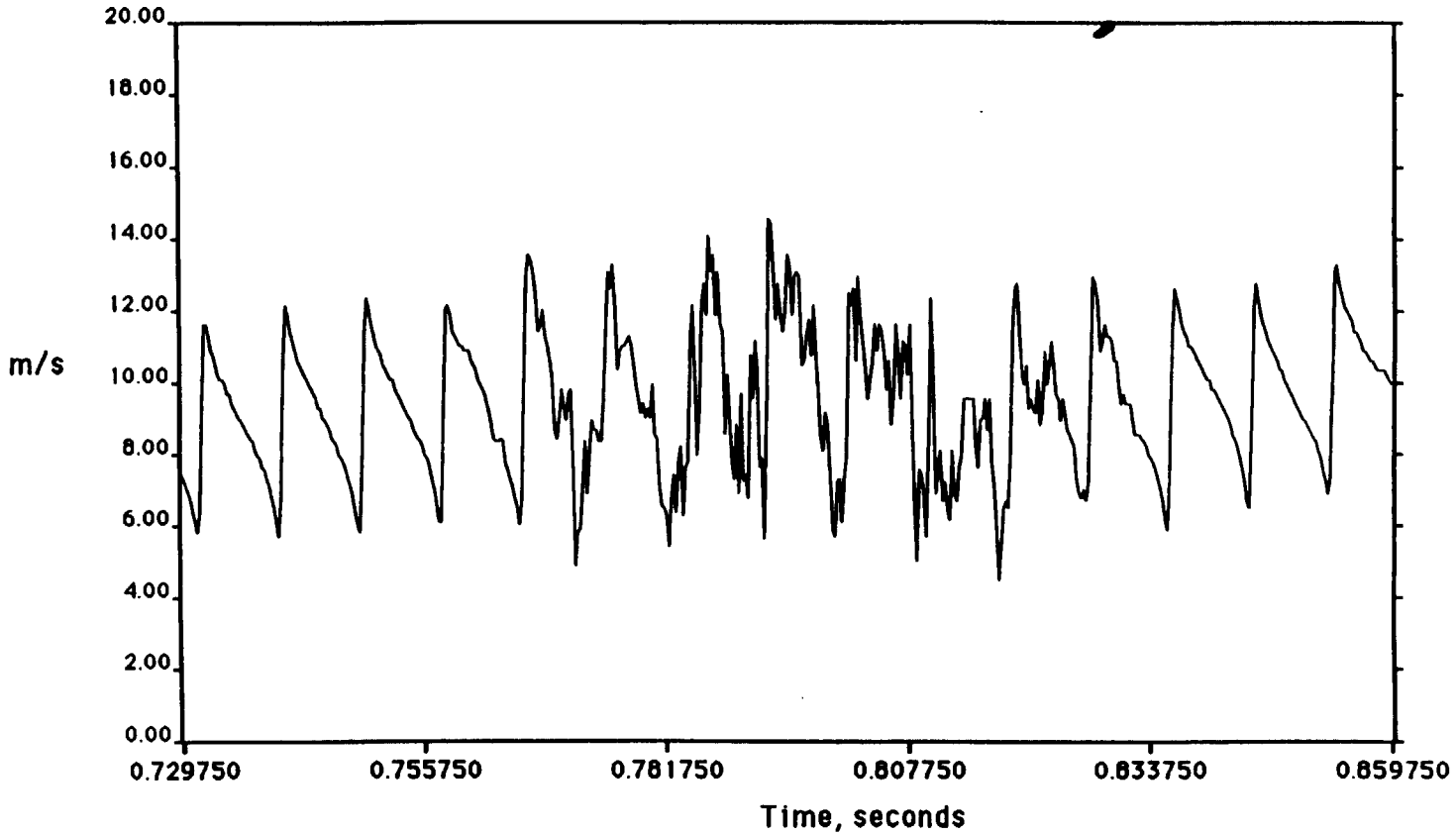

Figure 2.14 Time trace of inflow velocity in the fountain re-ingestion zone showing intermittently laminar and turbulent flow. Data taken with the hot wire parallel to the longitudinal axis, inboard, 2 inches from the rotor tip on the rotor/rotor axis, and 1 inch above the rotor plane.

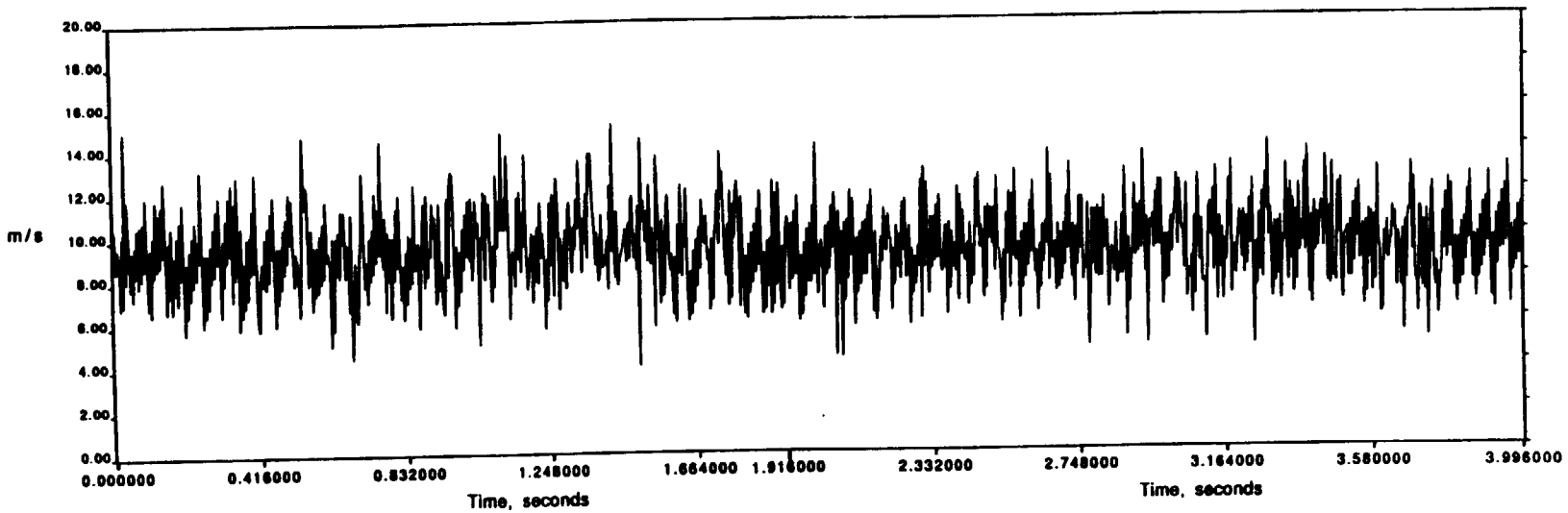

Figure 2.15 4 second time trace of inflow velocity in the fountain re-ingestion zone. Data taken with the hot wire parallel to the longitudinal axis, inboard, 2 inches from the rotor tip on the rotor/rotor axis, and 1 inch above the rotor plane.

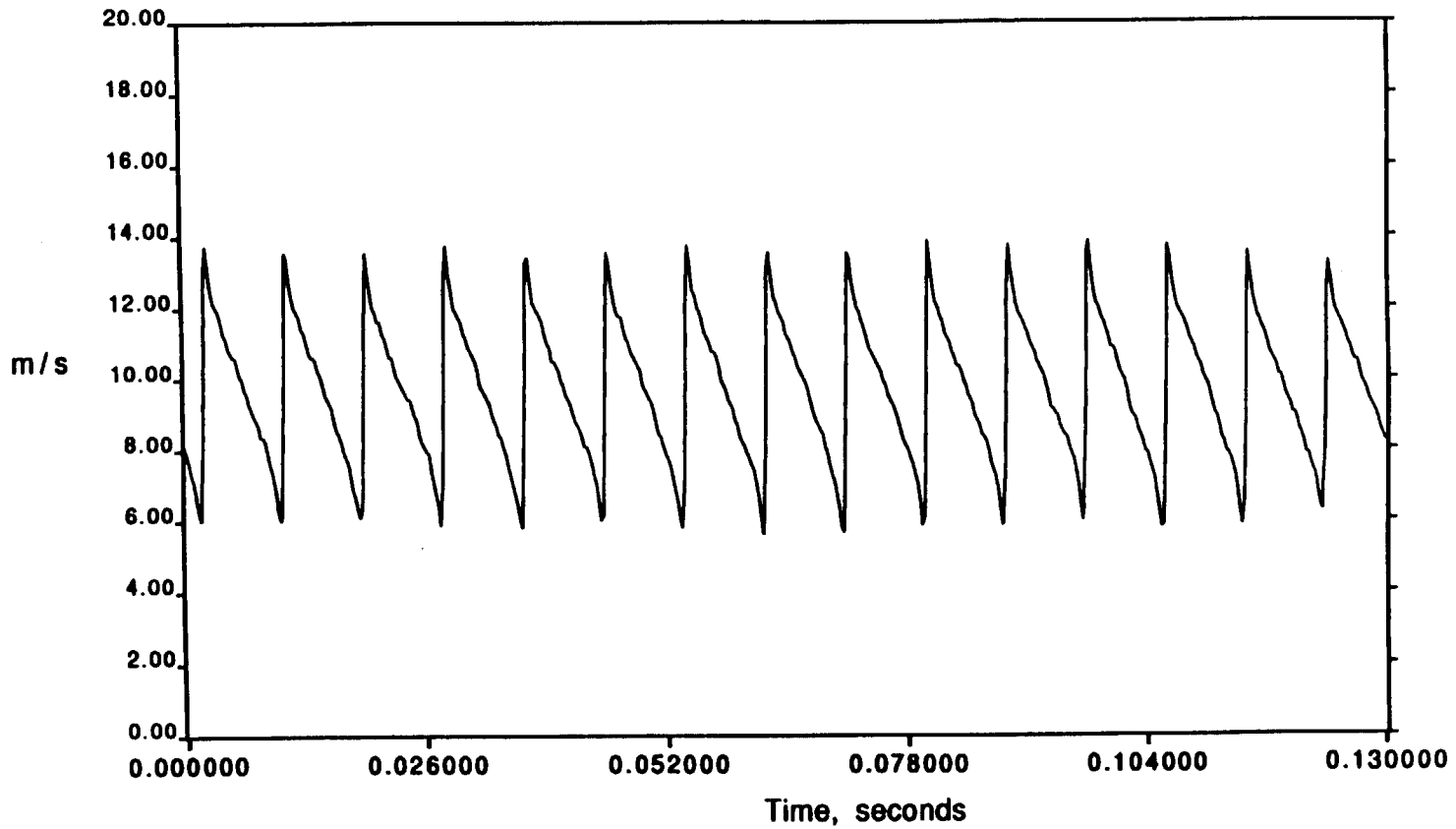

Figure 2.16 Time trace of inflow velocity over the outboard part of the rotor plane showing laminar flow unaffected by the fountain. Data taken with the hot wire parallel to the longitudinal axis, outboard, 2 inches from the rotor tip on the rotor/rotor axis, and 1 inch above the rotor plane.

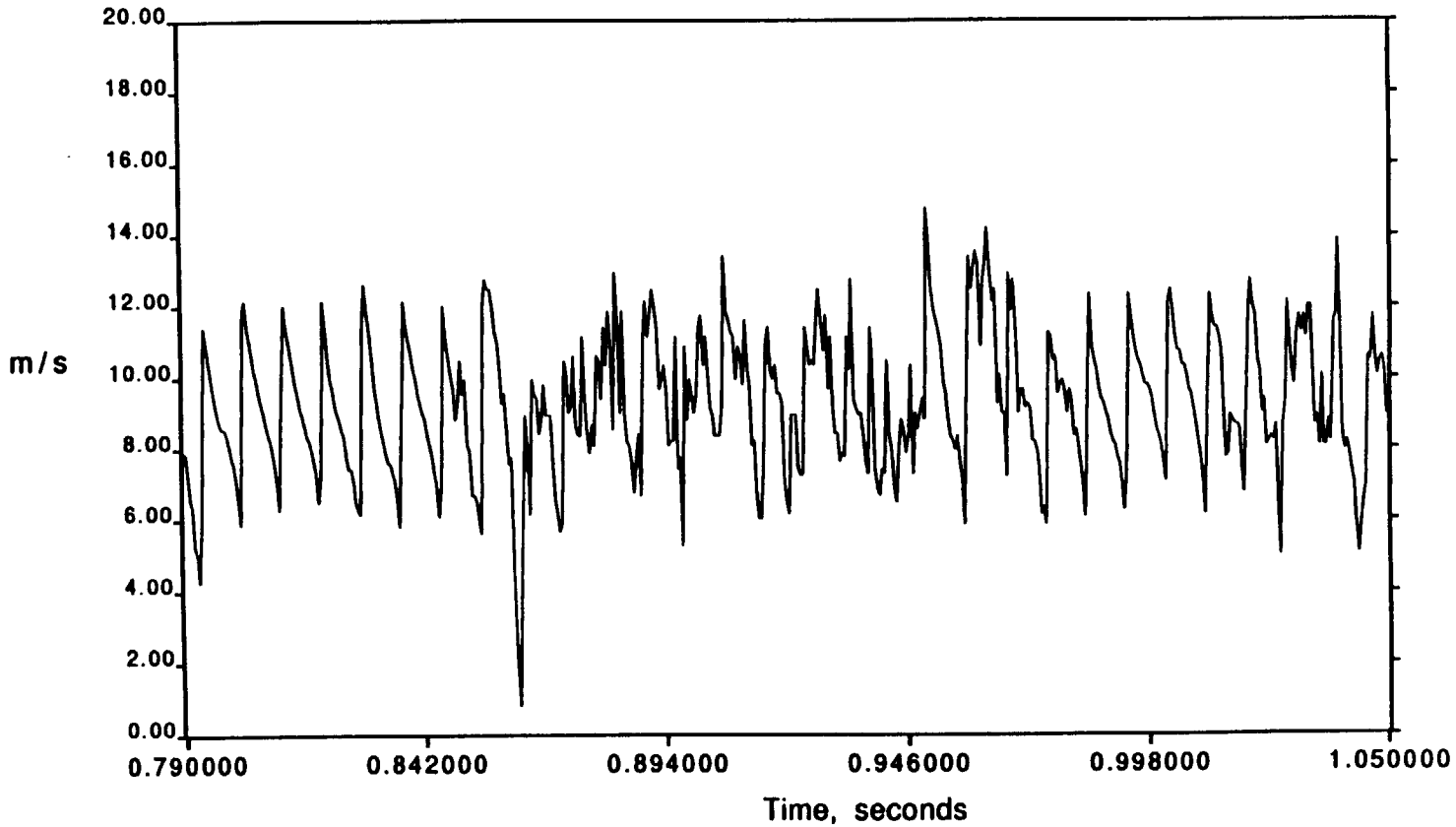

Figure 2.17a Time traces of inflow velocity in the fountain re-ingestion zone 1 inch above the rotor plane. Data taken with the hot wire parallel to the longitudinal axis, inboard, and 2 inches from the rotor tip on the rotor/rotor axis.

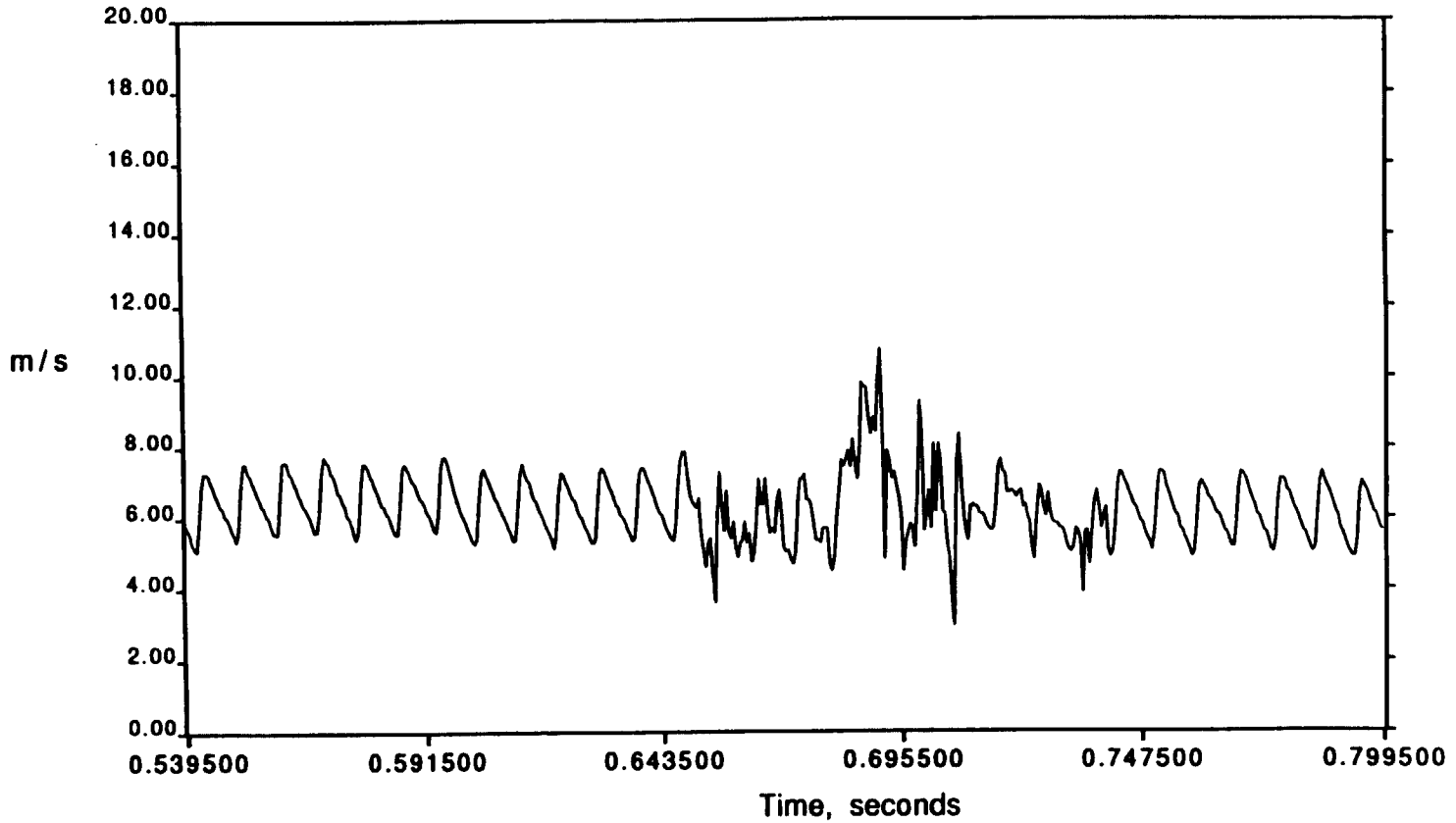

Figure 2.17b Time traces of inflow velocity in the fountain re-ingestion zone 3 inches above the rotor plane. Data taken with the hot wire parallel to the longitudinal axis, inboard, and 2 inches from the rotor tip on the rotor/rotor axis.

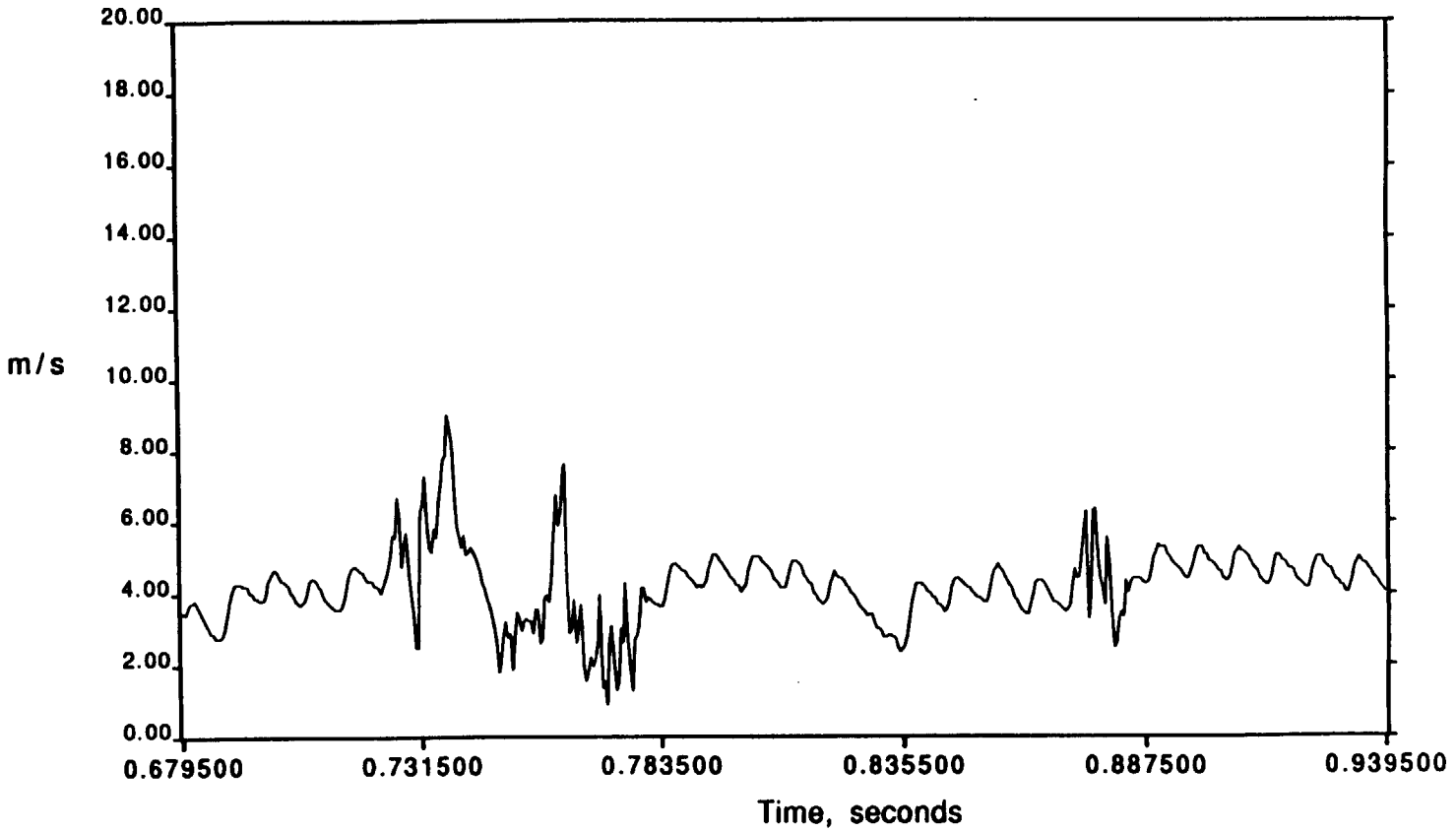

Figure 2.17c Time traces of inflow velocity in the fountain re-ingestion zone 5 inches above the rotor plane. Data taken with the hot wire parallel to the longitudinal axis, inboard, and 2 inches from the rotor tip on the rotor/rotor axis.

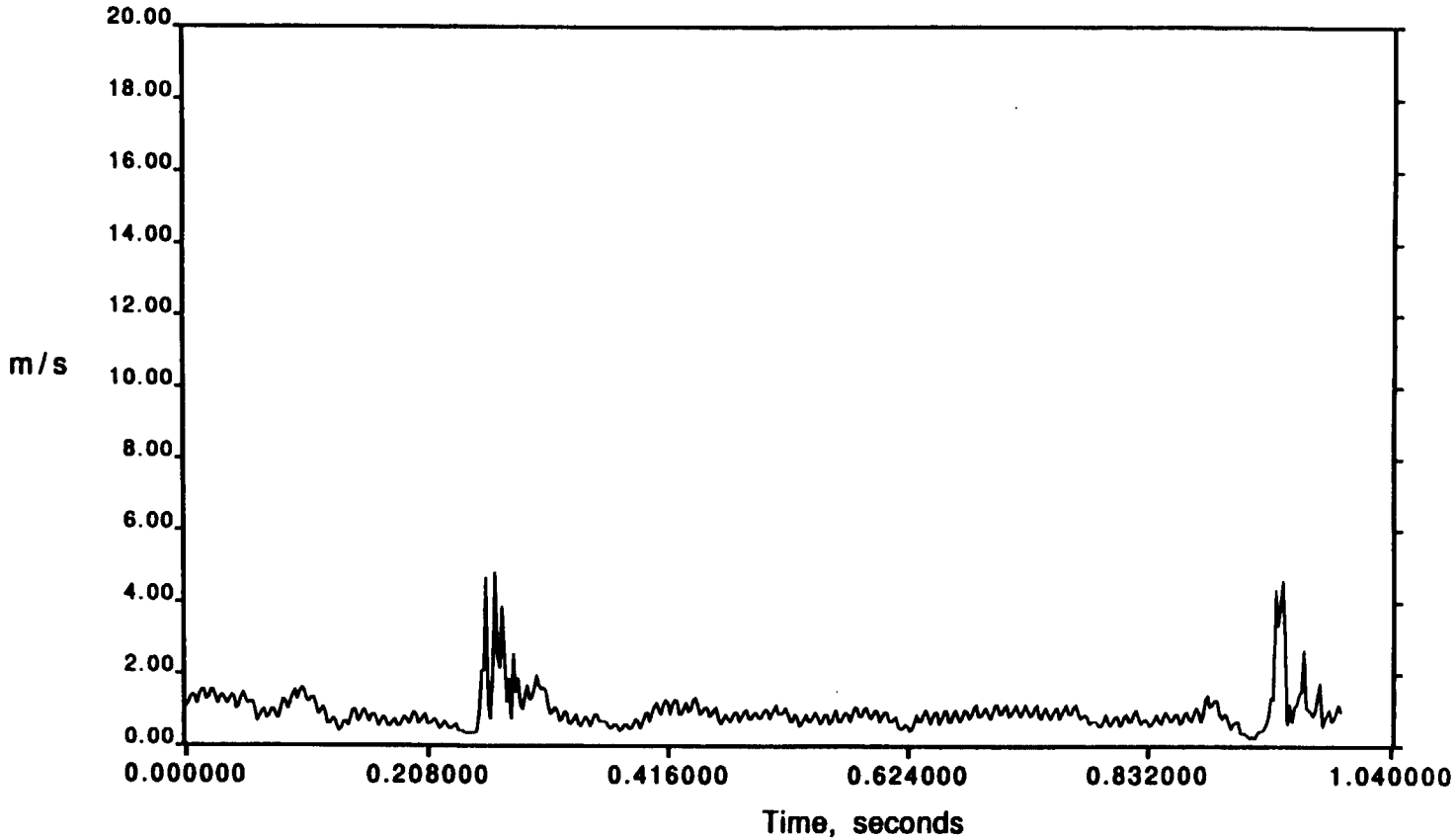

Figure 2.18a Time traces of velocity 7 inches forward of the rotor/rotor axis, 1 inch above the rotor plane. Hot wire oriented parallel to the longitudinal axis.

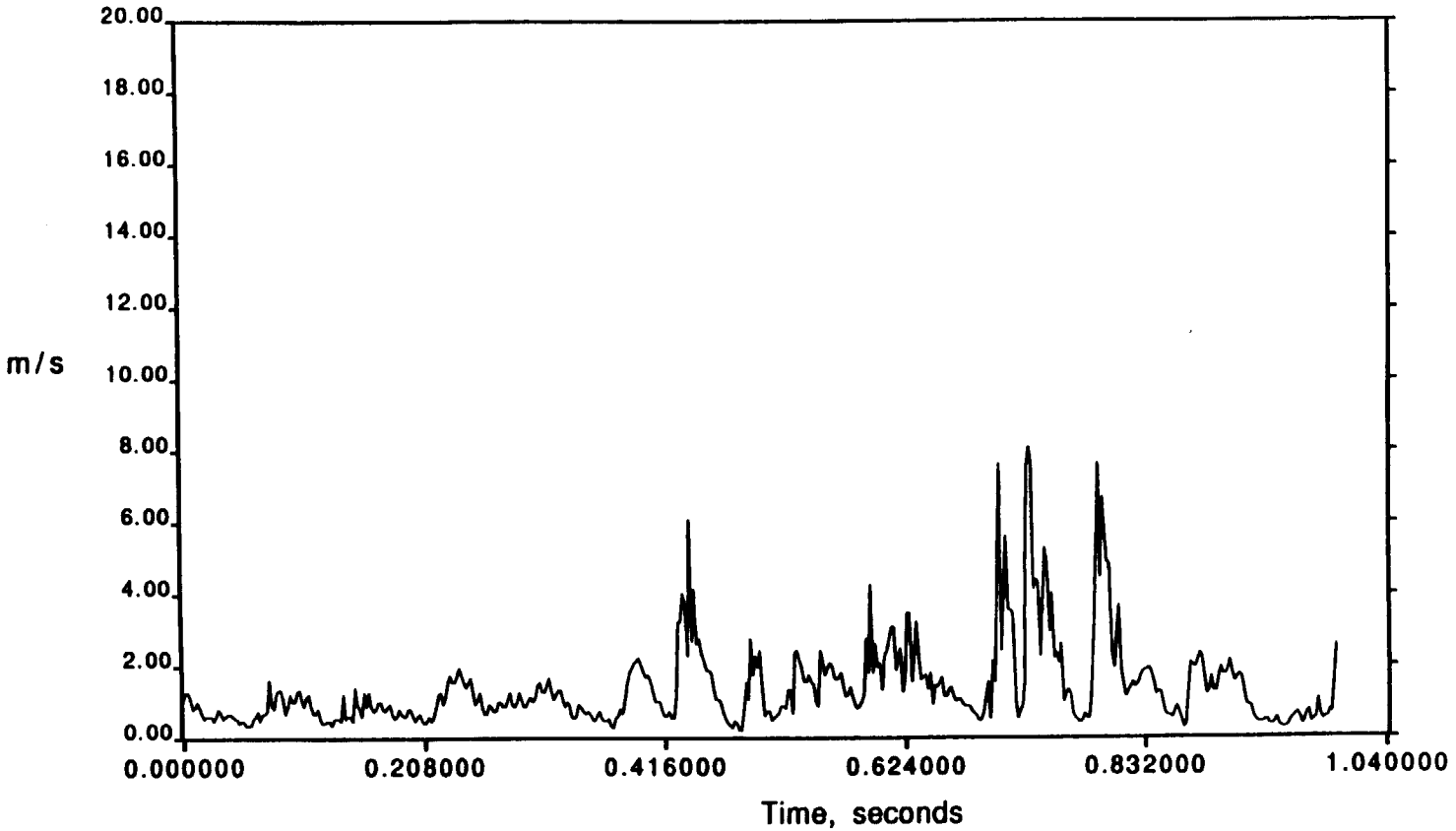

Figure 2.18b Time traces of velocity 5 inches forward of the rotor/rotor axis, 1 inch above the rotor plane. Hot wire oriented parallel to the longitudinal axis.

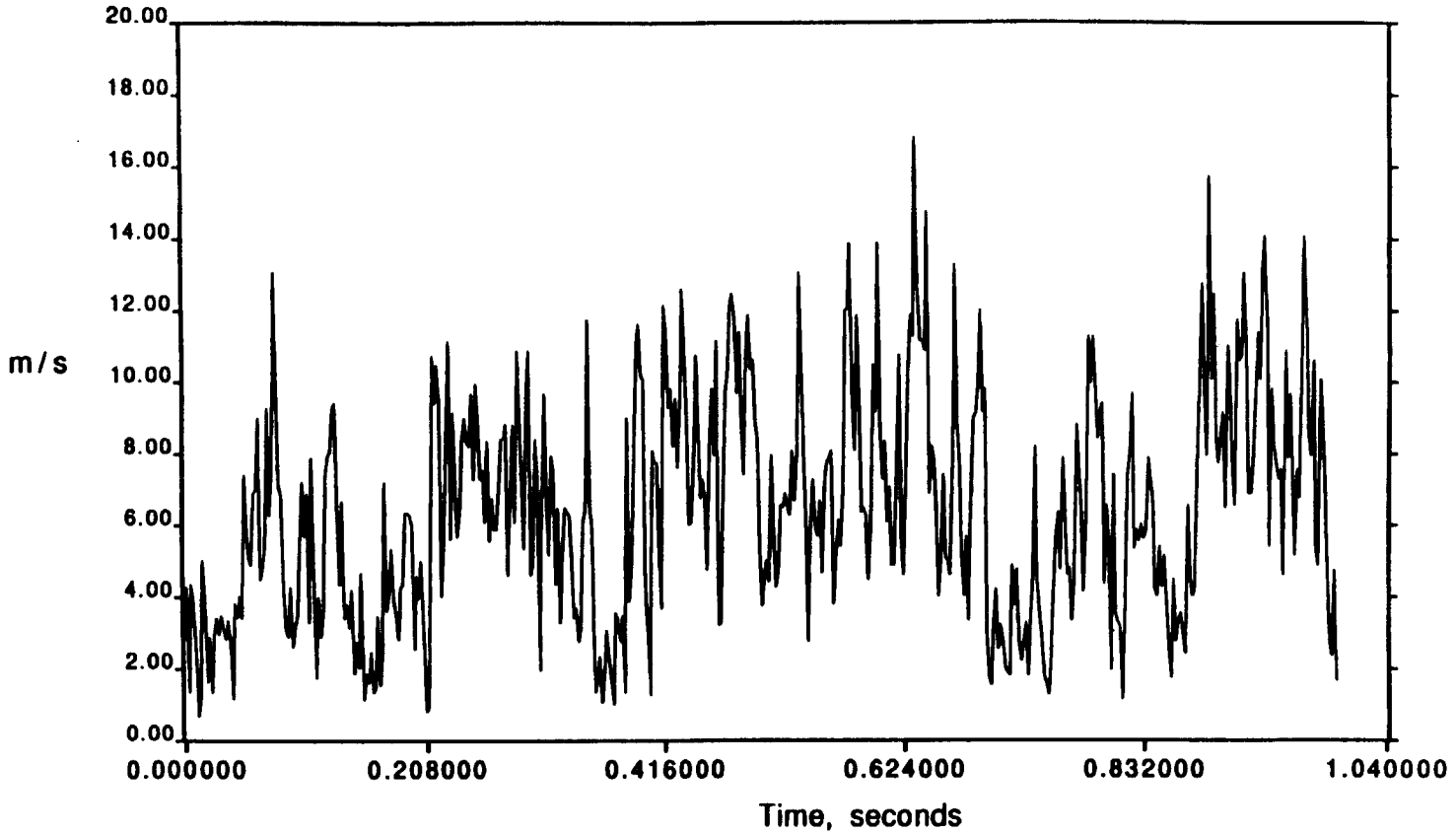

Figure 2.18c Time traces of velocity on the rotor/rotor axis, 1 inch above the rotor plane. Hot wire oriented parallel to the longitudinal axis.

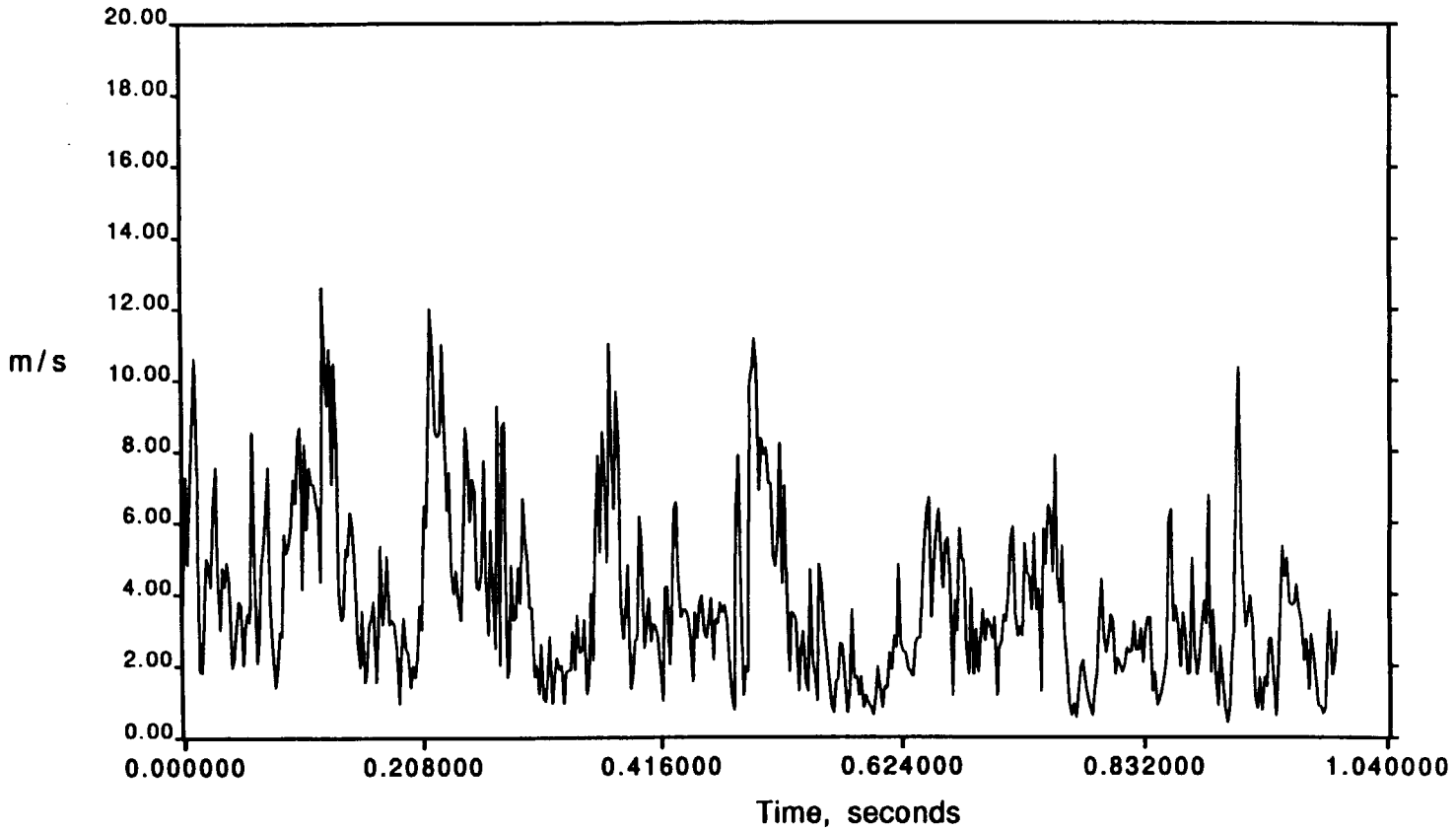

Figure 2.18d Time traces of velocity 8 inches rearward of the rotor/rotor axis, 1 inch above the rotor plane. Hot wire oriented parallel to the longitudinal axis.

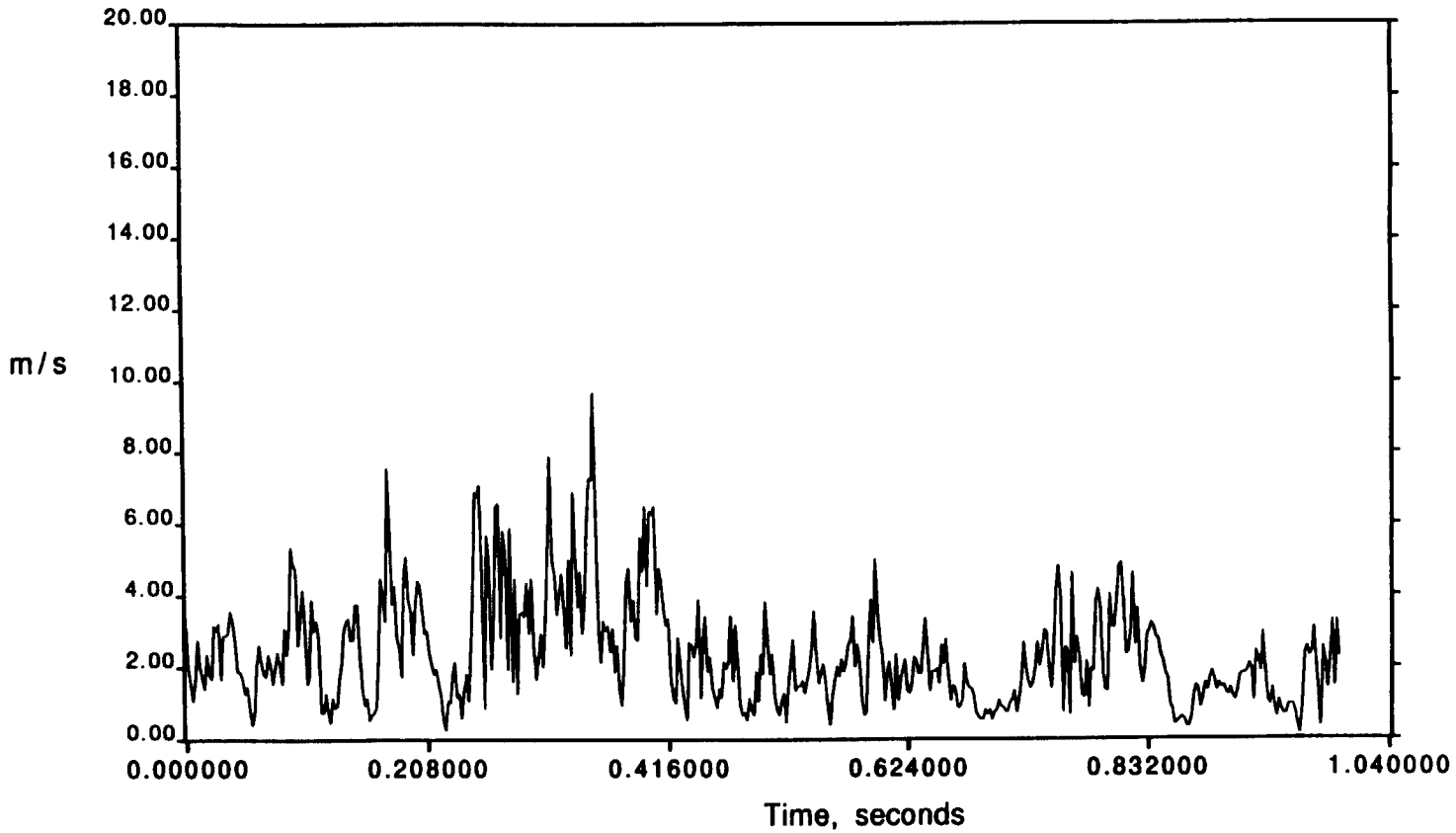

Figure 2.18e Time traces of velocity 12 inches rearward of the rotor/rotor axis, 1 inch above the rotor plane. Hot wire oriented parallel to the longitudinal axis.

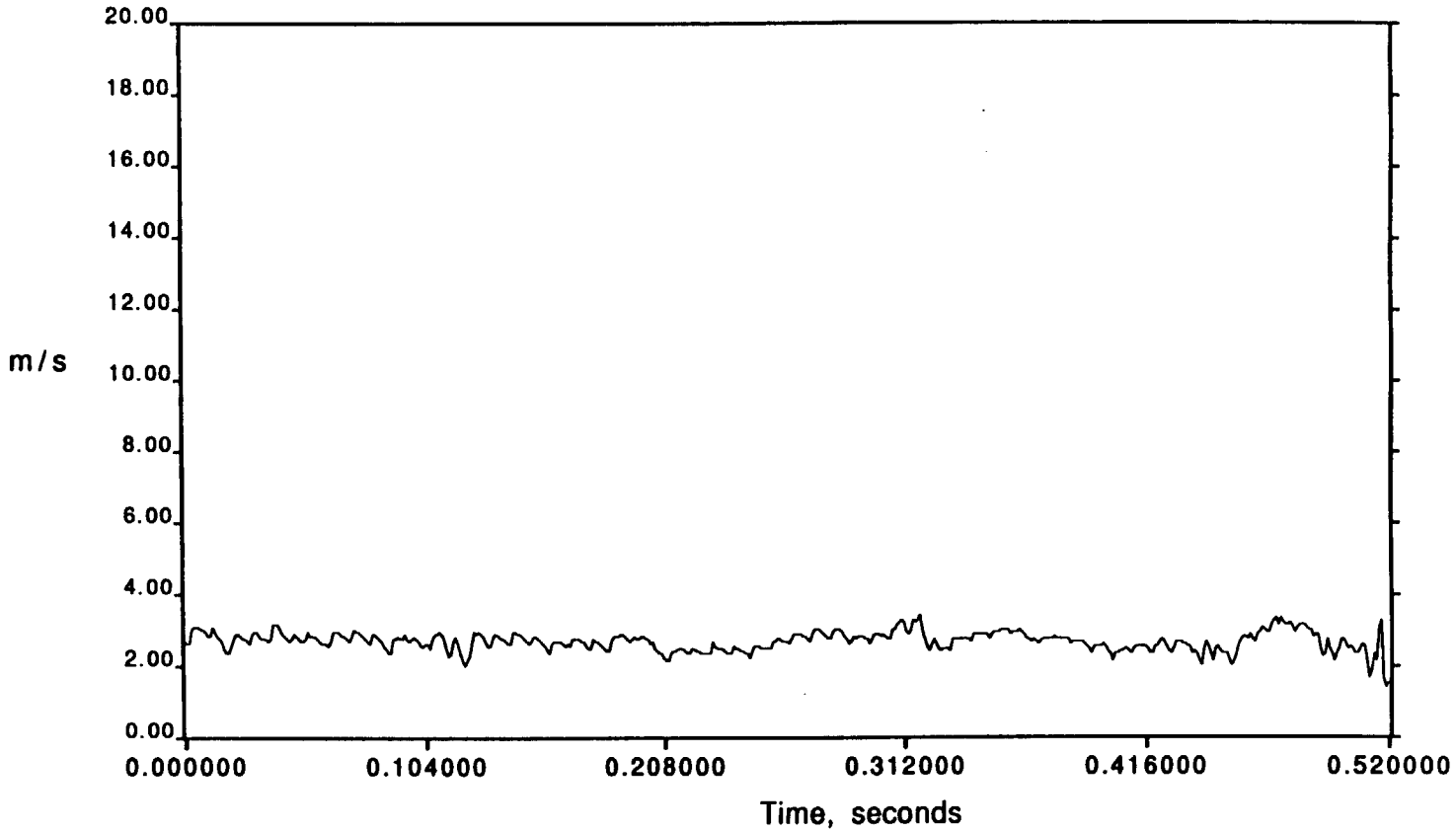

Figure 2.19a Time traces of velocity showing the effect of one and two rotors spinning. Hot wire 1 inch above the rotor plane on the intersection of the rotor/rotor and longitudinal axis. One rotor spinning showing very small velocity fluctuations.

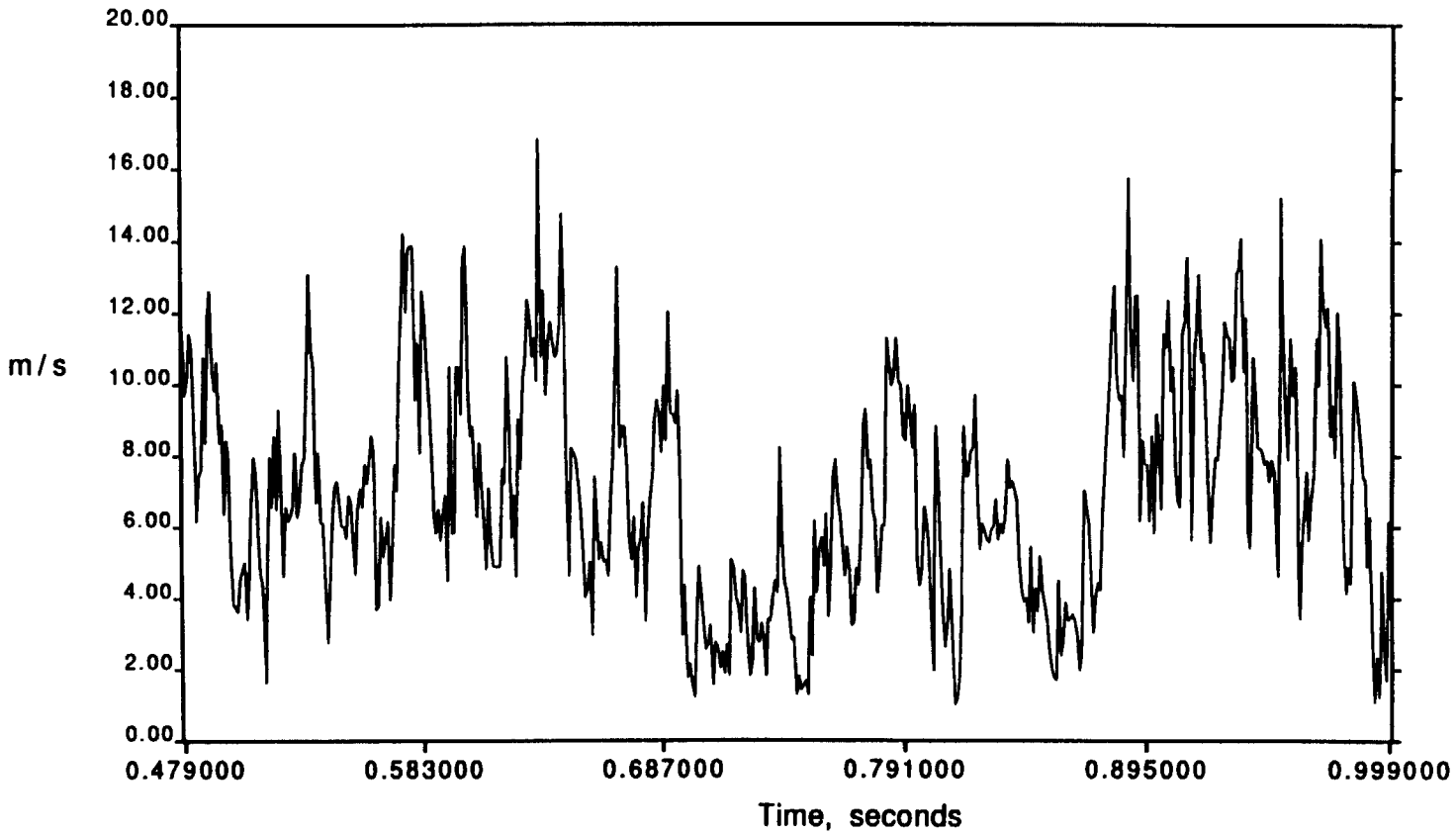

Figure 2.19b Time traces of velocity showing the effect of one and two rotors spinning. Hot wire 1 inch above the rotor plane on the intersection of the rotor/rotor and longitudinal axis. Two rotors spinning showing large velocity fluctuations.

trace over the outboard section of the rotor plane, one inch above the rotor and 2 inches from the tip on the rotor/rotor axis. Here the inflow is laminar and is undisturbed by the turbulent fluctuating recirculating fountain flow. Another interesting observation is that the peak inflow velocity due to the potential flow is 2 m/s greater in figure 2.16 than in figure 2.13a. This result is due to the wing obstructing the flow inboard and will be discussed in more detail below.

The height of the fountain was also studied by taking time traces at 1, 3, and 5 inches above the rotor plane at the point 2 inches inboard of the rotor tip on the rotor/rotor axis (in the fountain reingestion zone of the rotor). figures 2.17a-c show the progression of heights. The velocity fluctuations due to the potential flow associated with each blade passage decreases with increasing height. The amplitude of fluctuations due to the reingested fountain turbulence decreases from 1 to 3 inches above the rotor plane, but does not decrease as much between 3 and 5 inches above the rotor plane. The fluctuations are more rapid at the 1 and 3 inch heights than the 5 inch height. This indicates that the smaller turbulent eddies are reingested at a lower height and that only large scale eddies are recirculated to greater heights above the rotor plane. This result can also be seen in the flow visualization photos as the pathlines become less erratic as they travel higher above the rotor plane. This information may be useful for future attempts to ameliorate the fountain affect by reducing or eliminating its high frequency content.

Velocity versus time traces were also used to study the fountain flow above the fuselage. Figure 2.18a-e show series at five locations on the longitudinal axis one inch above the rotor plane. These figures show how the flow is recirculated preferentially to the rear of the aircraft. The velocity fluctuations fall off drastically as the probe is moved forward of the wing while remaining fairly constant as the probe is moved rearward. Figure 2.18e is of special interest as it shows large rapid fluctuations one rotor radius behind the wing/fuselage intersection. This shows that the longitudinal recirculating flow is not a minor or secondary affect and should be studied further as it may effect many operational characteristics such as hover performance, stability, and interior cabin noise.

Time traces were also generated for the case of the hot wire centered between the two rotors over the wing and one inch above the rotor plane with one and two rotors spinning. A comparison of these two half second traces, figure 2.19a-b, shows how the two rotors and wing and fuselage create a highly turbulent recirculating flow. The trace with one rotor running, figure 2.19a, only shows variations corresponding to the blade passage and some very mild disturbances of magnitude less than 1 m/s due to ambient room turbulence. With both rotors spinning, figure 2.19b, the recirculating flow causes fluctuations of magnitudes as great as 14 m/s.

2.4.2 Turbulence Spectra

The time traces described above are meant to provide a more qualitative view of the relative magnitudes and intermittency of the

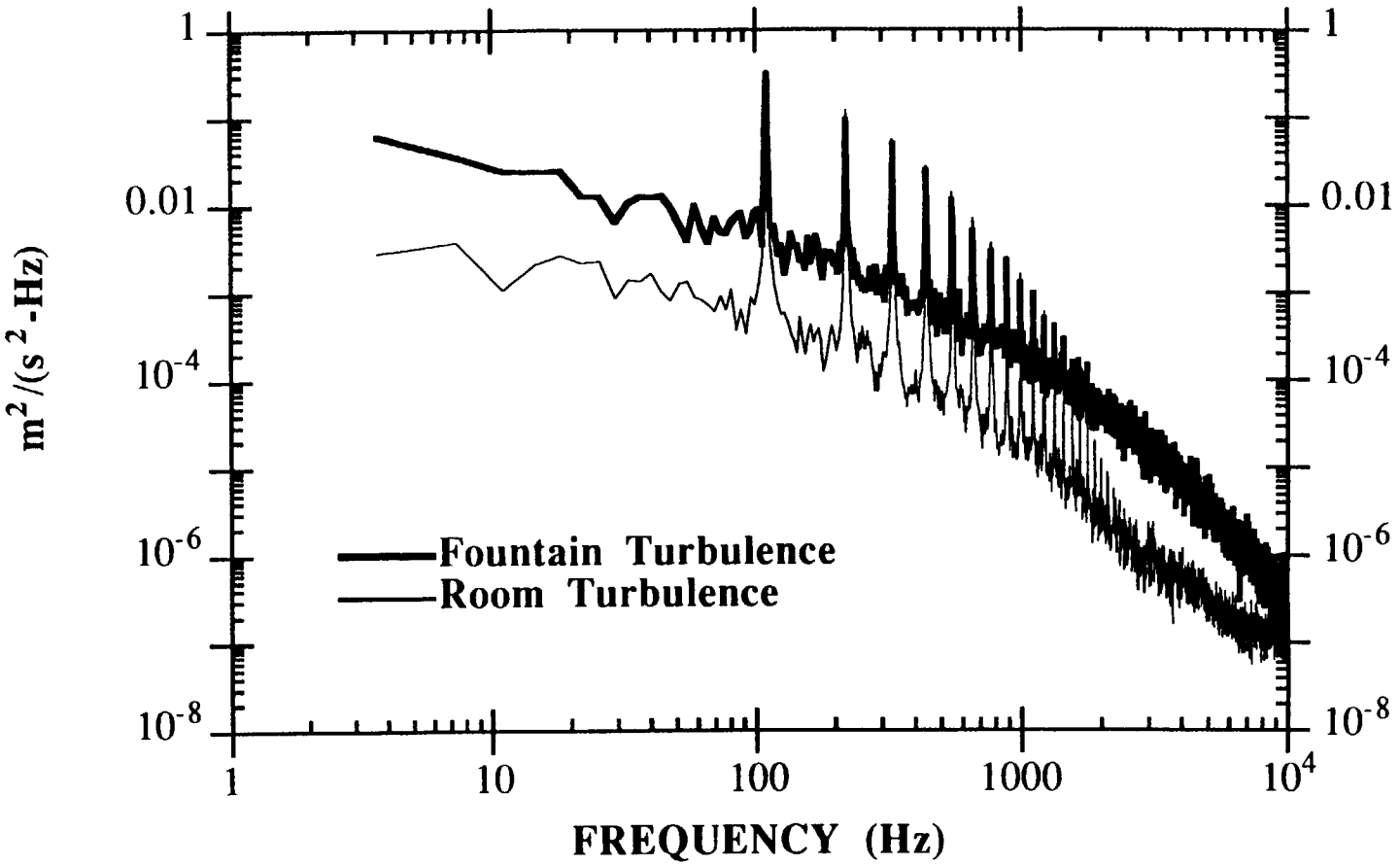

Figure 2.20 Comparison of power spectra (~2Hz Bandwidth) of inflow turbulence: fountain turbulence in the reingestion zone and ambient turbulence in the room. Data taken with the hot wire parallel to the longitudinal axis, inboard, 2 inches from the rotor tip on the rotor/rotor axis, and 1 inch above the rotor plane.

flow components measured by a single hot wire. Another experiment was to quantify the nature of the fountain turbulence. The spectrum of velocity squared was calculated from a stream of velocity measurements from a single hot wire. Figure 2.20 compares the power spectrum of inflow velocities measured by a single wire probe 1 inch above the rotor plane and 2 inches from the tip on the rotor/rotor axis in the reingestion zone. The top curve shows the turbulence due to the reingestion of the fountain flow. The lower curve is the power spectrum of the ambient inflow turbulence which was found by taking measurements with only one rotor spinning and the model removed from the experiment. Both spectra show the blade passing harmonics at integer multiples of approximately 113 Hz. This plot shows that there is 5 to 10 times more energy per unit frequency in the fountain turbulence than in the room turbulence for frequencies between 10 Hz and 2 kHz. This plot also shows that the spectral energy for the two cases becomes more similar at frequencies higher than 10 kHz. The greater low frequency content of the fountain inflow may be due to the intermittency discussed above while the increased high frequency velocity fluctuations are due to the reingestion of the turbulent recirculating fountain flow.

2.4.3 Mean and rms Inflow Velocities

Mean and rms velocities were also measured on an evenly spaced 25" by 25" square grid 1 inch above the rotor plane. Three grids of data were taken for the three Cartesian orientations of the hot wire. Reduction of this data was complicated by several factors.

A fully three dimensional turbulent flow cannot be quantified using a single wire hot wire unless some assumptions are made about the relative magnitudes of the velocity components. Also, the grid of hot wire measurements would have been better oriented in a cylindrical coordinate system as this would best fit the geometry of a hovering rotor. A Cartesian system was used as the available traverse was not appropriate for moving the probe with respect to radius and azimuthal angle. The data then had to be reduced in cylindrical coordinates. In order to do this, the theta component of mean velocity was assumed to be negligible compared to the radial and axial mean velocities. Another complicating factor was that the data was taken with a single wire probe which meant that data points had to be measured separately for each hot wire orientation. This leaves the possibility for error due to inexact probe placement for each set of measurements. Another source of error is that the rms values of velocity are sometimes more than 20% of the mean velocity which implies that King's Law is less accurate[17]. Future measurements will be conducted with an x-wire.

Figure 2.21a is a contour plot showing the axial component of inflow velocity measured without the wing and fuselage assembly. This plot shows the spatially uniform inflow that results when the wing does not obstruct the flow. Figure 2.21b is a contour plot showing the axial component of mean velocity over the rotor plane measured with the wing and fuselage assembly. Comparing to figure 2.21a, there is clearly a deficit in the inflow velocity over the wing. The deficit is recognizable by lighter shading over the wing and lower valued contours. As has been hypothesized previously,[18]

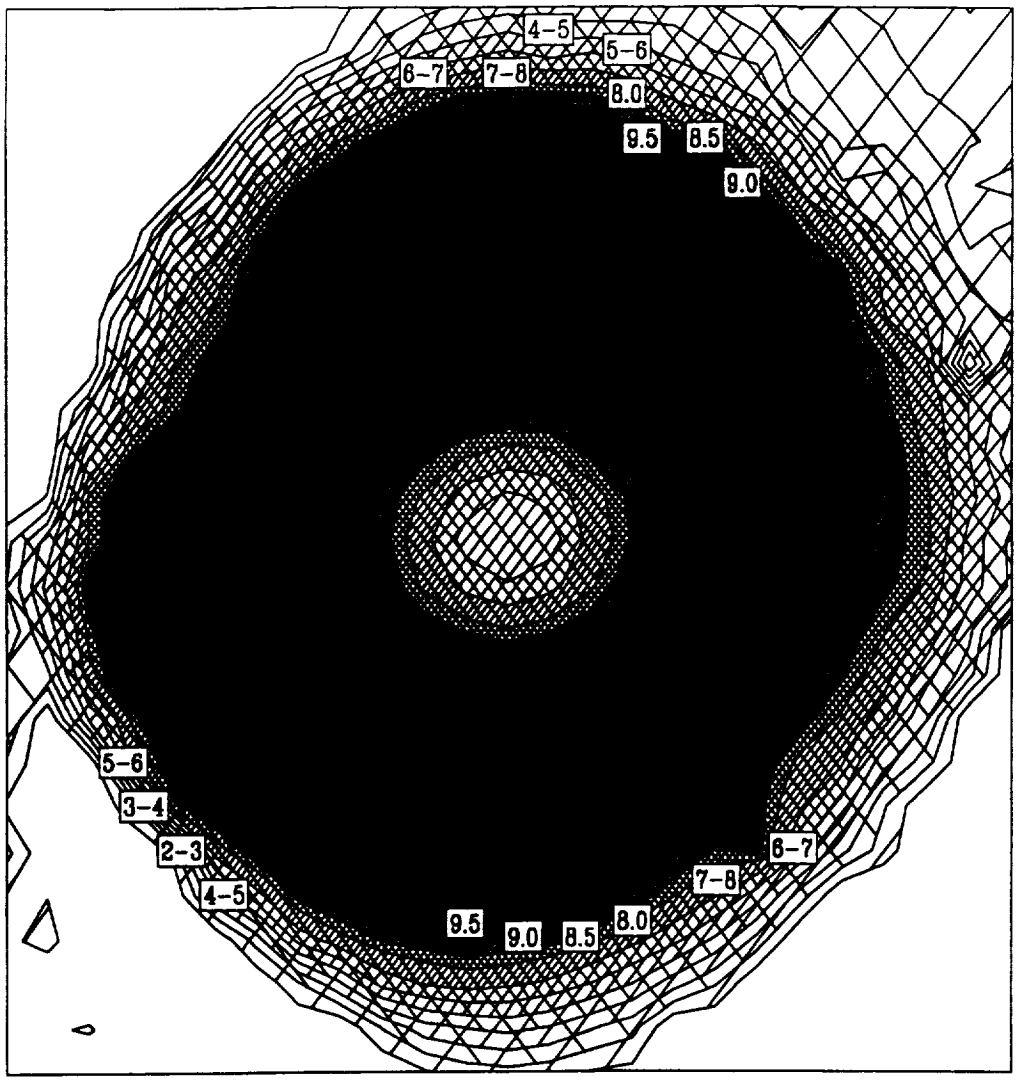

Figure 2.21a Axial component, V_z, of mean inflow velocity without wing and fuselage assembly. Square border indicates grid boundary. Plot shows port rotor, rotor spins clockwise, wing and body are to the right of the grid. Darker shading corresponds to higher velocity.

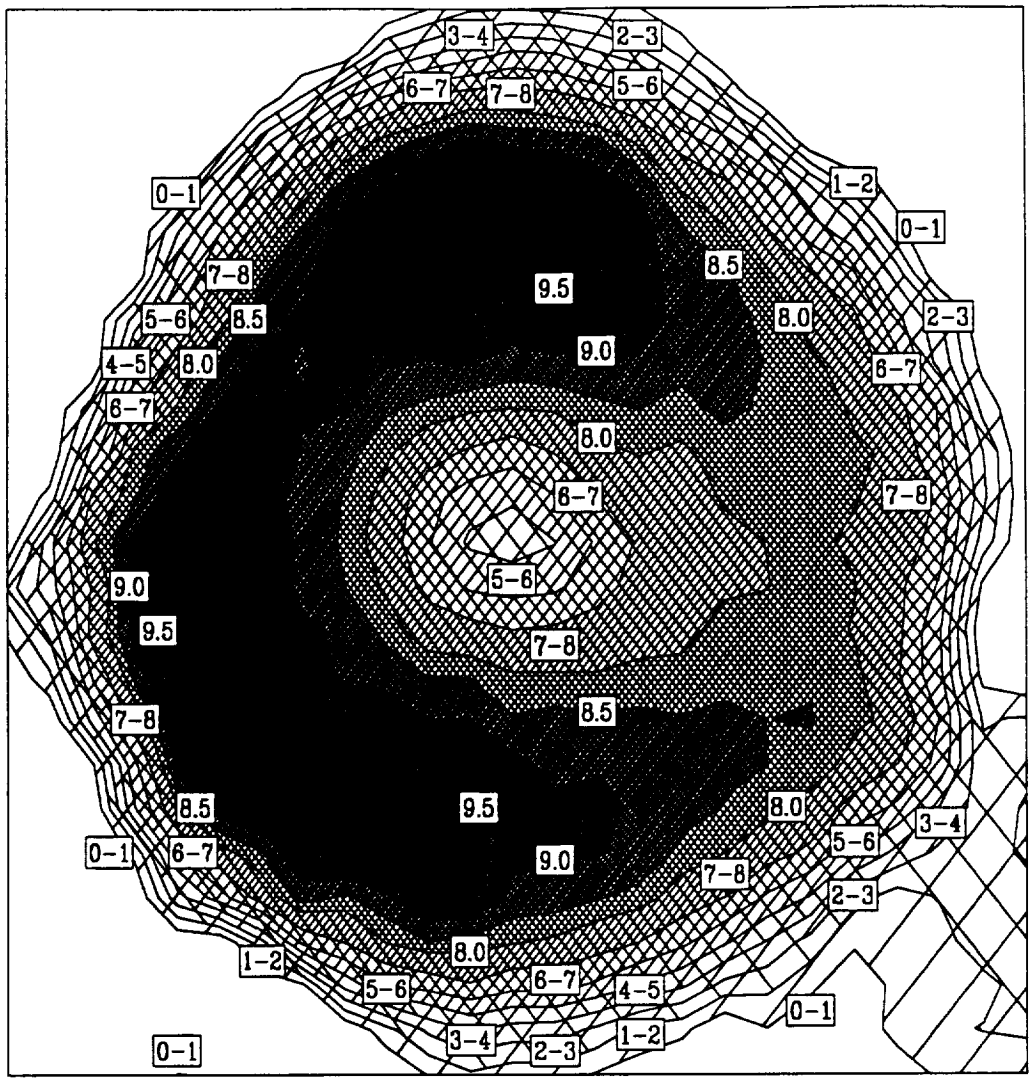

Figure 2.21b Axial component, V_Z, of mean inflow velocity with wing and fuselage assembly. Square border indicates grid boundary. Plot shows port rotor, rotor spins clockwise, wing and body are to the right of the grid. Darker shading corresponds to higher velocity. Note lighter shading over the wing.

this deficit is due to the wing obstructing the flow beneath the rotor. While these results are not accurate enough to precisely model the fountain flow, they are conclusive in showing this important phenomenon of tilt rotor hover flow.

Figure 2.22 is a plot of the rms velocity over the rotor plane. This contour plot uses values obtained from three orthogonal sets of hot wire data and plots the values of $\sqrt{V_x'^2 + V_y'^2 + V_z'^2}$. No attempt was made to reduce this data to component form for the following reason; While the turbulence is most likely isotropic at higher frequencies, the data was measured 1" above the rotor plane and therefore it also reflects the velocity fluctuations due to the potential flow field (blade passage). Thus we are unable to present the rms velocities by component as we are unable to precisely separate the potential flow velocity fluctuations from the velocity fluctuations due to the inflow turbulence. Qualitatively, the existence of the potential flow is not a problem as the turbulent velocity fluctuations in the reingestion zone are significantly greater than those caused by the potential flow field. This is apparent from figure 2.22 which shows the reingestion zone as a region of high rms velocities (darker shading) on the inboard section of the rotor. These high values are a result of the turbulent fountain flow recirculating into the inflow where it is measured as velocity fluctuations by the hot wire. This plot also shows higher rms values towards the rear of the grid which indicates that the flow is reingested in the rearward side of the rotor/rotor axis. This region of high rms velocities corresponds to the reingestion region observed in the flow visualization study.

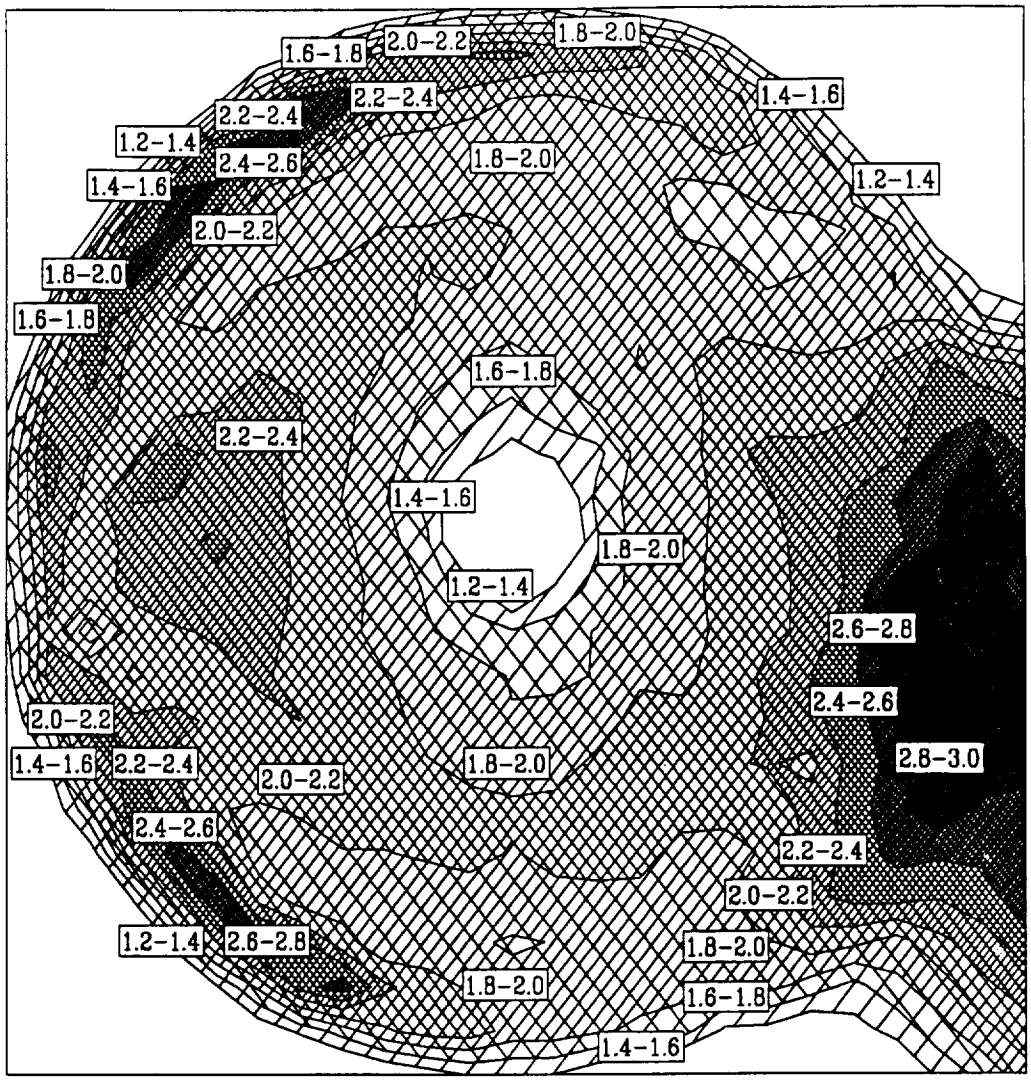

Figure 2.22 RMS, $\sqrt{V_z'^2 + V_r'^2 + V_\theta'^2}$, inflow velocity. Square border indicates grid boundary. Plot shows port rotor, rotor spins clockwise, wing and body are to the right of the grid. Darker shading corresponds to higher velocity. Note darker shading indicating the re-ingestion zone.

Chapter III
Discrete Noise Predictions Using WOPWOP

This chapter presents the methodology and results of noise prediction calculations carried out to study thickness and loading discrete frequency harmonic noise mechanisms of the XV-15 Tilt Rotor Aircraft in hover. In particular, the loading noise caused by the fountain/ground plane effect is investigated using WOPWOP[19], a rotor noise prediction program developed by NASA Langley.

3.1 WOPWOP Aeroacoustic Theory

WOPWOP is a noise prediction program developed by the NASA Langley Research Center to predict helicopter main rotor noise. WOPWOP calculates discrete frequency noise of helicopter rotors by employing the most advanced acoustic formulation of Farassat and allows for realistic helicopter blade geometry, motions and aerodynamic loadings. The blade geometry, motions and loadings must be input by the user through FORTRAN subroutines, and the accuracy of the output depends almost entirely on the accuracy of this input.

The theoretical basis for the WOPWOP code stems from the Ffowcs Williams and Hawkings equation discussed in Chapter I. Equation 1.11 is presented here with the following substitutions:

$$4\pi p'(\underline{x},t) = \frac{\partial}{\partial t}\int_{f=0}\left[\frac{\rho_0 v_n}{r|1-M_r|}\right]dS(\eta) - \frac{\partial}{\partial x_i}\int_{f=0}\left[\frac{l_i}{r|1-M_r|}\right]dS(\eta) \tag{3.1}$$

The density perturbation has been replaced by the acoustic pressure, $p' = c_0^2\rho$, the compressive stress tensor, $p_{ij}n_j$, has been replaced by the force per unit area on the fluid, l_i, and the surface of integration, S, is defined by some function, f = 0. The spatial derivative of the loading noise can be converted to a time derivative by starting with the formal solution of equation 1.5 and using the relation:

$$\frac{\partial}{\partial x_i}\left[\frac{\delta(g)}{4\pi r}\right] = -\frac{1}{c}\frac{\partial}{\partial t}\left[\frac{\hat{r}_i\delta(g)}{4\pi r}\right] - \frac{\hat{r}_i\delta(g)}{4\pi r^2} \tag{3.2}$$

prior to the integration of delta function in the $-\frac{\partial}{\partial x_i}\left(p_{ij}\,\delta(f)\frac{\partial f}{\partial x_j}\right)$ term. This gives the following result:

$$4\pi p'(\underline{x},t) = \frac{1}{c_0}\frac{\partial}{\partial t}\int_{f=0}\left[\frac{c_0\rho_0 v_n + l_r}{r|1-M_r|}\right]dS(\eta) - \int_{f=0}\left[\frac{l_r}{r^2|1-M_r|}\right]dS(\eta) \tag{3.3}$$

In this formulation, termed "formulation 1" by Farassat[20], $l_r = l_i\hat{r}_i$ and represents the force on the fluid per unit area in the radiation direction. "Formulation 1A" is derived by taking the time derivative into the integral. This improves accuracy of the

numerical differentiation. The result is given here from reference 19 as:

$$p'(\underline{x},t) = p_T'(\underline{x},t) + p_L'(\underline{x},t)$$

$$4\pi p_T'(\underline{x},t) = \int_{f=0} \left[\frac{\rho_0 \dot{v}_n}{r(1-M_r)^2}\right] dS(\eta) + \int_{f=0} \left[\frac{\rho_0 v_n (r\dot{M}_i \hat{r}_i + c_0 M_r - c_0 M^2)}{r^2(1-M_r)^3}\right] dS(\eta)$$

$$4\pi p_L'(\underline{x},t) = \frac{1}{c_0} \int_{f=0} \left[\frac{\dot{l}_i \hat{r}_i}{r(1-M_r)^2}\right] dS(\eta) + \int_{f=0} \left[\frac{l_r - l_i M_i}{r^2(1-M_r)^2}\right] dS(\eta) + \frac{1}{c_0} \int_{f=0} \left[\frac{l_r (r\dot{M}_i \hat{r}_i + c_0 M_r - c_0 M^2)}{r^2(1-M_r)^3}\right] dS(\eta) \quad (3.4)$$

Here p_T' and p_L' represent the thickness and loading noise (acoustic pressure) generated by the rotor. The dots over variable represent differentiation with respect to source time, not observer time.

This formulation is valid for any defined blade motion and geometry. The acoustic sources, monopoles and dipoles, are defined on the blade surface and will include any defined aerodynamic loading. This expression calculates the near-field, $1/r^2$, and far-field, $1/r$, terms explicitly, though this study is primarily interested in the tilt rotor far field acoustics. Future studies could investigate

the near field noise of a hovering tilt rotor and its affect on cabin noise using this formulation.

This formulation is coded in the WOPWOP rotor noise prediction program. The code requires the user to write three input subroutines which describe the geometry and aerodynamics of the aircraft main rotor. WOPWOP also makes use of a name list data file which defines the operating conditions and motions of the rotor. Two sets of input routines were developed for this study, one set for the metal blades used initially on the XV-15, and a set for the Advanced Technology Blade, ATB, rotors. The metal blade routines were developed for predictions based on a limited experimental data base. The ATB routines were developed as a result of a joint XV-15 aeroacoustics study by Cornell and Lockheed personnel[4].

3.2 Description of Metal Blade Input Routines

The three input subroutines define a mathematical model of the XV-15 by making use of theoretical aerodynamics, data given in the Tilt Rotor Research Aircraft Familiarization Document[21], and experimental data for two dimensional airfoils. Perhaps the most important aspect of this model is the characterization of the inflow velocity field. As was documented in chapter II, the wing below the rotor acts as a partial ground plane which causes a decrement in the inflow velocity over the wing. This change in inflow causes a change is angle of attack of the rotor blade as it passes over the wing. The net affect is a azimuthally varying loading distribution on the rotor blade. This effect is modeled in the input routines and

is seen to be the dominant discrete frequency noise mechanism in hover.

The following describes the FORTRAN subroutines used as input for WOPWOP. The organization of this description parallels the WOPWOP user's manual by defining the variables as they appear in the manual.

3.2.1 Subroutine FUNE2

This routine defines the main rotor blade geometry in the radial direction. The parameters of interest in this routine are the geometric twist of the blade, chord width, thickness and camber.

Geometric Twist:

The geometric twist of the blade is defined by two linear functions of radial position. One function covers the rotor blade from r=0 to r=1/2R and the other covers the rotor blade from r=1/2R to R. These two linear function are taken without change from data supplied by Bell, (see Appendix A). The derivative of the variation of twist with radius is defined by the slope of the linear function.

Pitch Change Axis:

Two other geometric quantities which require definition are the perpendicular distance from the chord line to the pitch change axis and the distance from the pitch change axis to the leading edge of the blade section. The pitch change axis distance was assumed to be zero over the span of the blade and the leading edge distance

was assumed to be 25% of the chord and was taken to be negative. These assumptions are made from the sample routines included in the WOPWOP manual as no data was available to accurately define these quantities.

Chord:

The chord of the blade section was defined as a function of radius and varies linearly from 18.2 inches at the theoretical root to 14 inches at 25% of the radius. From this point to the blade tip the chord was a constant 14 inches. This data was taken from 'XV-15 Blade Properties' provided by Bell.

Maximum Thickness Ratio:

The maximum thickness ratio of the blade section, thickness/chord, was defined by calculating a linear function of radius from the Bell airfoil data given for 14 radial stations in 'XV-15 Blade Properties'. The maximum thickness ratio varied from 35% at the theoretical root to 8% at the tip. This linear curve fitted the data with an r^2 of .99.

Maximum Camber Ratio:

The maximum camber ratio of the blade section, camber/chord, is defined by the airfoil section at each radial station. The airfoil section is given by Bell in 'XV-15 Blade Properties' for 14 stations. Every section is a 64 series airfoil. The data states that design coefficients, c_l, are assumed to vary linearly between stations. The maximum camber ratio is defined as the camber ratio

times the design lift coefficient divided by the ideal coefficient of lift for a 64 series airfoil, (see reference 22). The design lift coefficient was found by linear interpolation between values given at the 14 radial stations.

3.2.2 Subroutine FUNE2Q

This subroutine defines the chordwise geometry of the rotor blade in terms of radial and chordwise location.

Camber:

The camber is defined as the distance from chord line to camber line divided by the maximum camber displacement and is expressed as a fifth order polynomial fit to the data points found in reference 22, p.385. The function is multiplied by a correction factor for design lift coefficient based on the radial station location of the blade element as described above for maximum camber distance in FUNE2.

Thickness:

The thickness is defined as the distance from camber line to upper or lower surface divided by the maximum thickness. This distance is measured perpendicular to the chord line. The thickness at a given chordwise and radial location is calculated by chordwise and radial interpolation from defined data points. Data for 64 series airfoils of various thicknesses is tabulated in reference 22, pp. 347 - 353 in terms of chordwise position. These tables were used to create a two dimensional set of data points (radial and chordwise

frame of reference) from which the thickness at a given point on the blade can be extrapolated by linearly interpolating between four data points surrounding the point of interest. Five radial stations were selected to create the mesh with airfoils of 8%, 12%, 18%, 28%, and 35% thickness. The only significant approximation was that data had to be created for 28% and 35% thick airfoils. This was done by linearly scaling the thickness data of a 21% thick airfoil. This approximation is reasonable as the data given by reference 22 varies approximately linearly with thickness for 64 series airfoils. A more rigorous mathematical model of the rotor blade should include more airfoil sections and actual data for the thicker airfoils.

Chordwise Derivatives:

The derivative of the camber with respect to chord was calculated by taking the derivative of the polynomial function. The derivative of thickness with respect to chord was calculated using a finite difference method over a 1% length of chord. The derivative is calculated over a 0.5% length of chord at the leading and trailing edges.

The results of the geometry definitions are shown in figure 3.1 and 3.2 for both the metal and ATB blades.

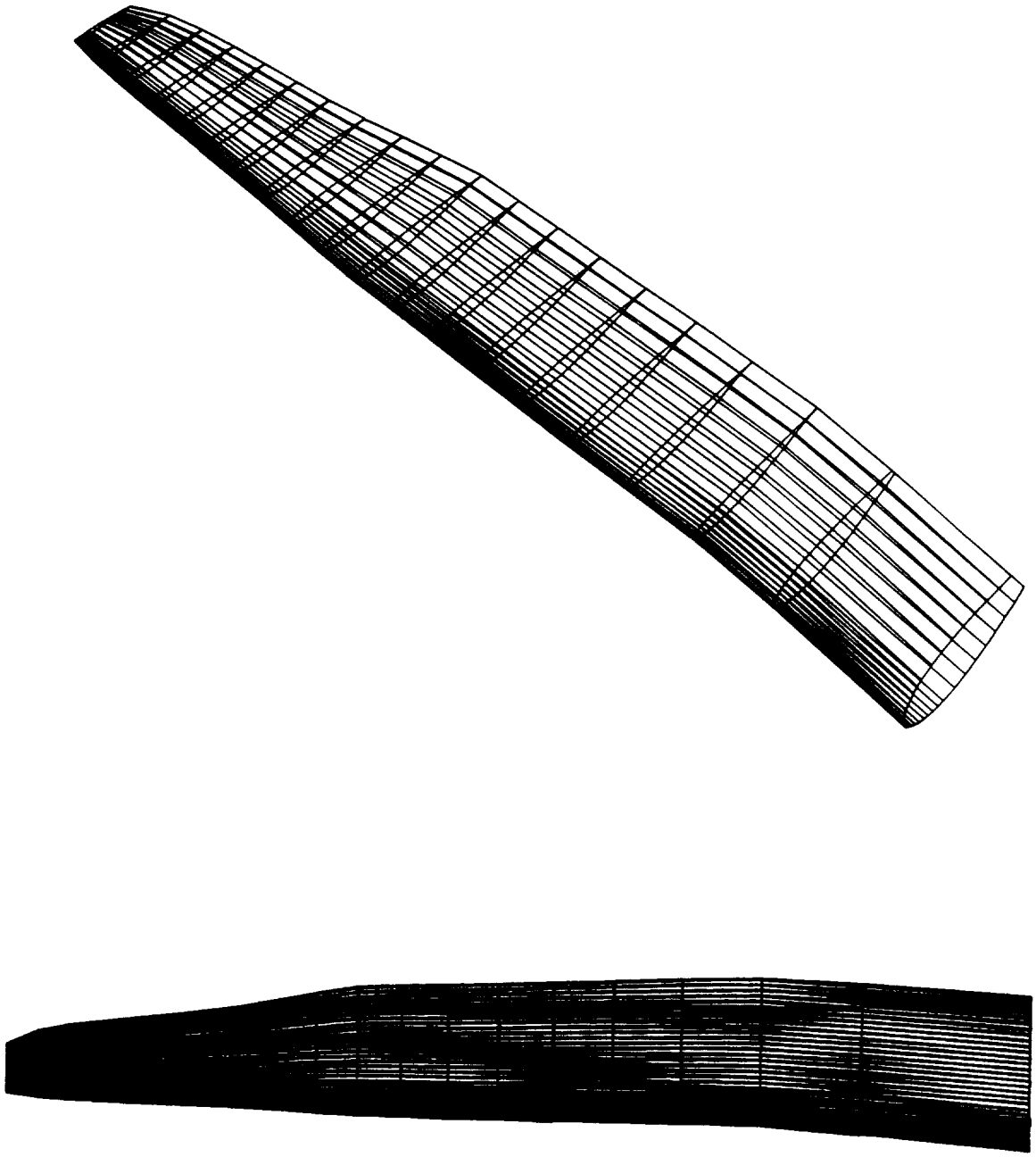

Figure 3.1 XV-15 Advanced Technology Blade geometry. Isometric, top, and planform, bottom.

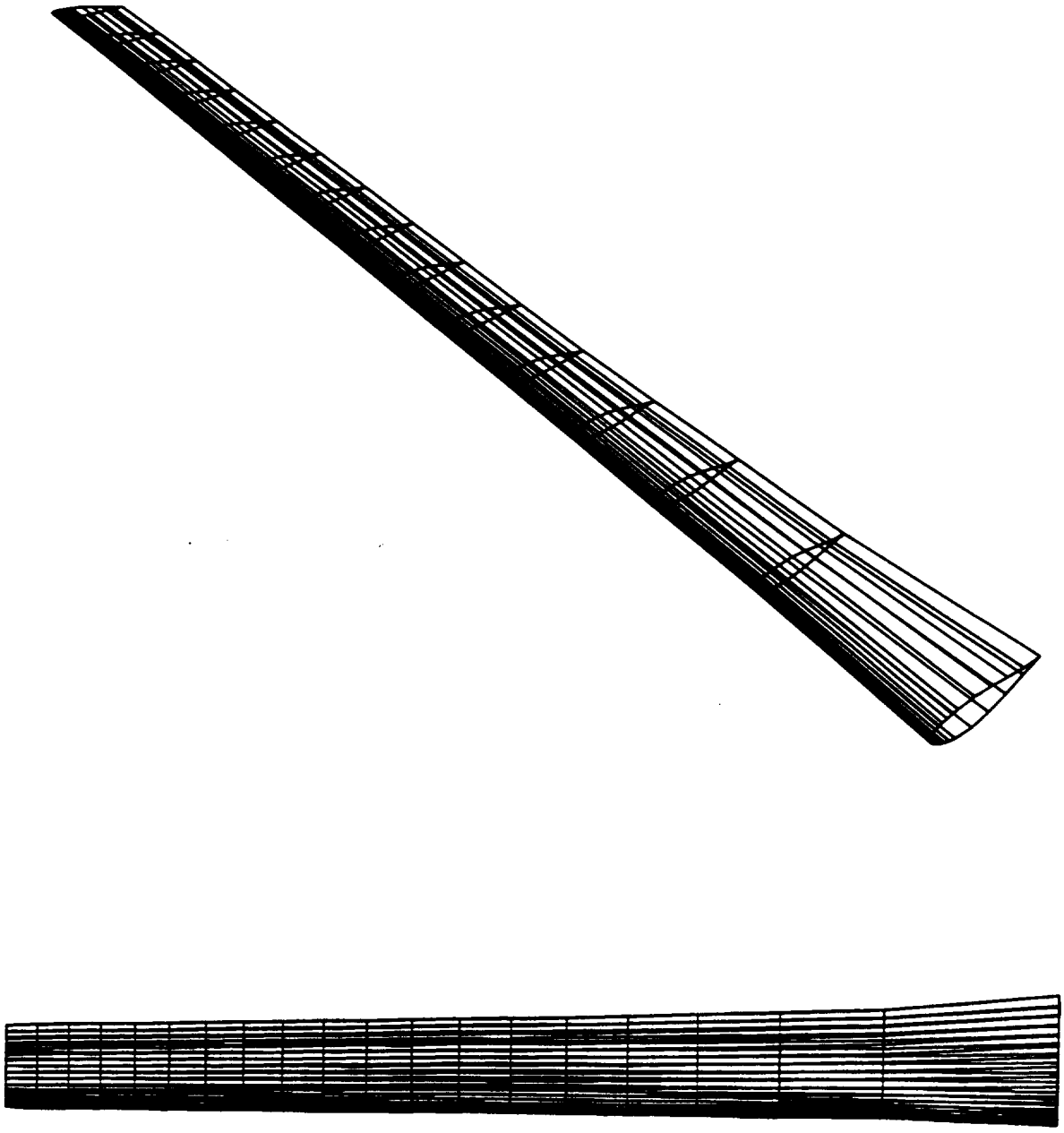

Figure 3.2 XV-15 Metal blade geometry. Isometric, top, and planform, bottom.

3.2.3 Subroutine FUNPSI

This subroutine describes the pressure distribution on the blade surface as a function of radial, chordwise and azimuthal position. This is the most complicated of the input routines and requires several assumptions and qualitative descriptions of the complicated three dimensional flow about a rotor blade in hover and forward flight. The method of computing the pressure at a point on the rotor blade was similar for hover and forward flight. The point is defined by its radial, chordwise and azimuthal positions. From these three coordinates, the angle of attack and relative velocity is calculated for the blade element containing the point. The pressure coefficient is then determined by the velocity addition method of reference 22. This method is described below and in appendix B.

Relative Velocity and Angle of Attack:

In hover, the angle of attack is equal to the sum of the collective pitch, blade twist and inflow. The twist is known from subroutine FUNE2. The inflow was assumed constant such that:

$$V_{in} = \sqrt{\frac{\text{Thrust}}{2 \cdot \text{density} \cdot \text{disk area}}} \tag{3.5}$$

The inflow angle is calculated as:

$$\tan^{-1}\left(\frac{V_{in}}{\text{radial velocity}}\right). \tag{3.6}$$

The collective was found by adjusting the collective angle until WOPWOP calculated the thrust required to match the hover value of C_T given in reference 18. This procedure provided radially varying angles of attack in agreement with hover data provided by Bell.

The relative velocity of the blade element was simply the radial distance from the hub times the rotor rate of rotation, $V = \Omega \cdot r$.

Pressure Distribution Calculation:

The pressure distribution about the airfoil was calculated using the velocity addition method of reference 22 outlined in appendix B. This method is based on adding velocity increment ratios due to camber, thickness and angle of attack in order to find the total velocity ratio at a point on an airfoil. The data for this technique was tabulated for 64 series airfoils in reference 22 pp. 346-353. As with the thickness calculations, data had to be estimated for 28% and 35% thick airfoils by scaling data from thinner airfoils. The results of this scaling are approximate as the velocity addition method may be inaccurate for thick airfoils. However, pressure distributions calculated by this method appear to be qualitatively correct and agree well with pressure distributions calculated using a panel method[23] for thin airfoils at low angles of attack.

Miscellaneous:

The above pressure distribution is corrected for compressibility by the Prandlt Glaurt compressibility correction.

The time derivative of the pressure was calculated using a finite difference method.

3.2.4 Fountain Model

Analysis of previous NASA flow visualization studies[14] and particularly the results of chapter II have shown that the presence of the wing under the hovering rotor causes profound flow phenomena referred to loosely as the fountain effect. The wing obstructs the downwash from the hovering rotor, causing the flow to turn spanwise along the wing. Also, the wing acts as a partial ground plane below the rotor which causes a decrease in the inflow velocity as the blade passes over the wing. While the change in inflow relevant to discrete noise is due to the partial ground plane, this phenomenon will be referred to as the "fountain effect" as all associated tilt rotor flow phenomena have been loosely associated with the recirculating flow.

As the exact details of the fountain flow and its effect on the rotor blade loading are not known, a mathematical model was developed to simulate a deficit in the inflow velocity over the wing. The parameters of the model are based on the chord of the wing. The main effect of the inflow velocity deficit is to increase the angle of attack of a blade element as it sweeps over the wing. This results in a time varying blade loading which produces sound. A plot of p(t) at the quarter chord point of three radial positions as a function of azimuth is shown in figure 3.3.

The mathematical model defines the width of the affected region to be 4/5 of the wing chord with an inflow velocity deficit of

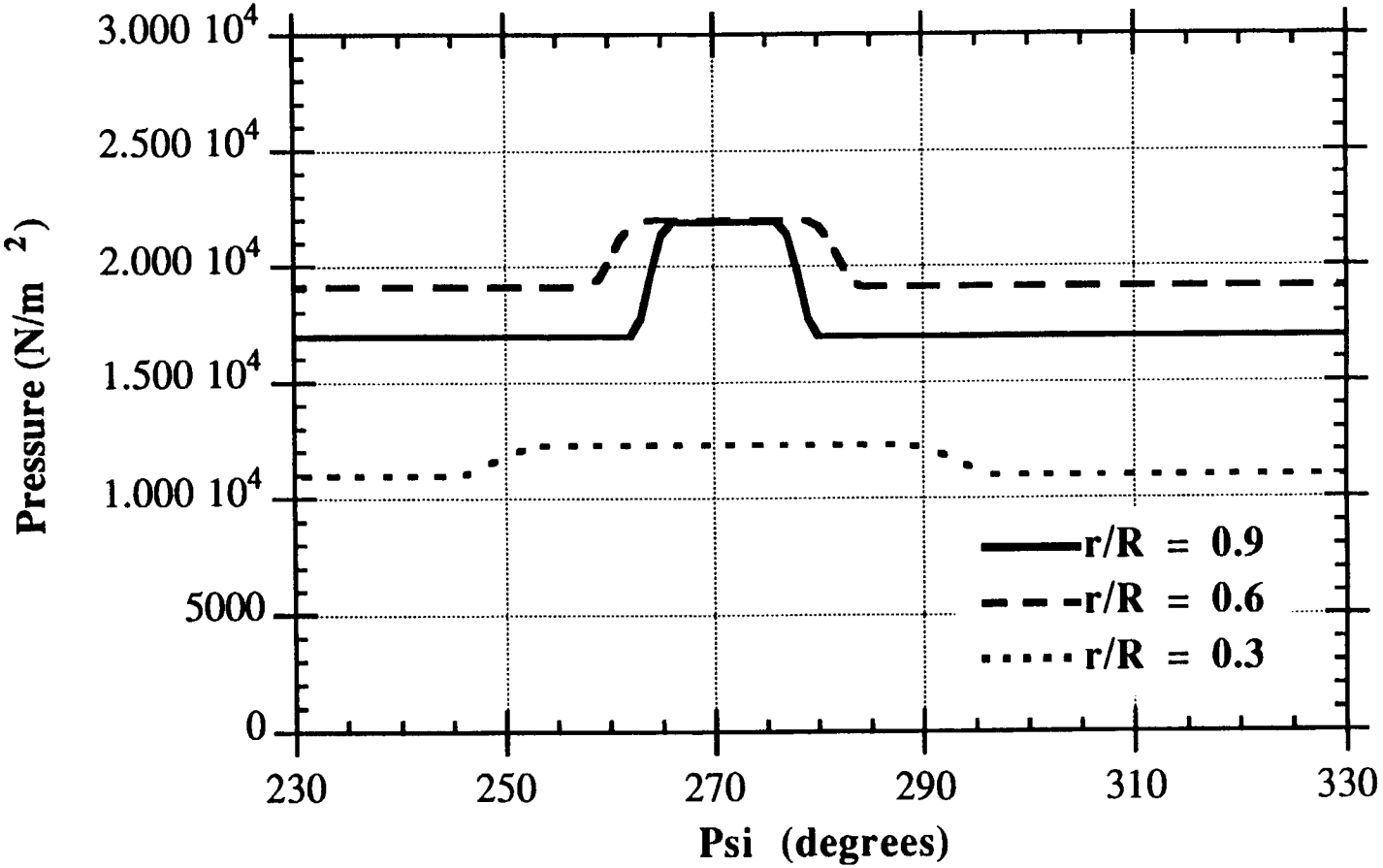

Figure 3.3 Blade element quarter chord pressure as a function of azimuth. Fountain effect centered on Psi = 270°. Quasi-steady blade response. Metal blade geometry.

20%. A sketch of the inflow velocity profile is shown in figure 3.4. As the blade approaches the region over the wing, the inflow is made to decrease as a quarter sine wave to 80% of the constant inflow velocity calculated from momentum theory. The inflow profile is made to be symmetric about the center point of the wing. The forward sweep of the wing is not accounted for. Appendix C contains the details of the mathematical model.

This model is very approximate but is currently substantiated by visual experiment and scale model results. It simulates a flow disturbance caused by the wing obstructing the downwash. Further investigation into the recirculating fountain effect will provide more accurate models in the future.

3.2.5 Namelist

The name list specifies the operating conditions of the main rotor including the location of the microphone, forward speed, rotor speed and blade motion coefficients. The inputs for the operating conditions were obtained from the experimental cases of hover and forward flight. The blade motion coefficients are defined by the Fourier coefficients in the Namelist. In hover, a constant coning angle of 2° was used. The blade lagging and feathering coefficients were set to zero as aeroelastic effects were neglected.

The above three subroutines and name list represent a mathematical model of the geometry and aerodynamics of the XV-15 metal blade rotor. A similar set of routines was developed to model the different geometry and loadings of the ATB blades. The loading definitions differed in that no chordwise accurate loading

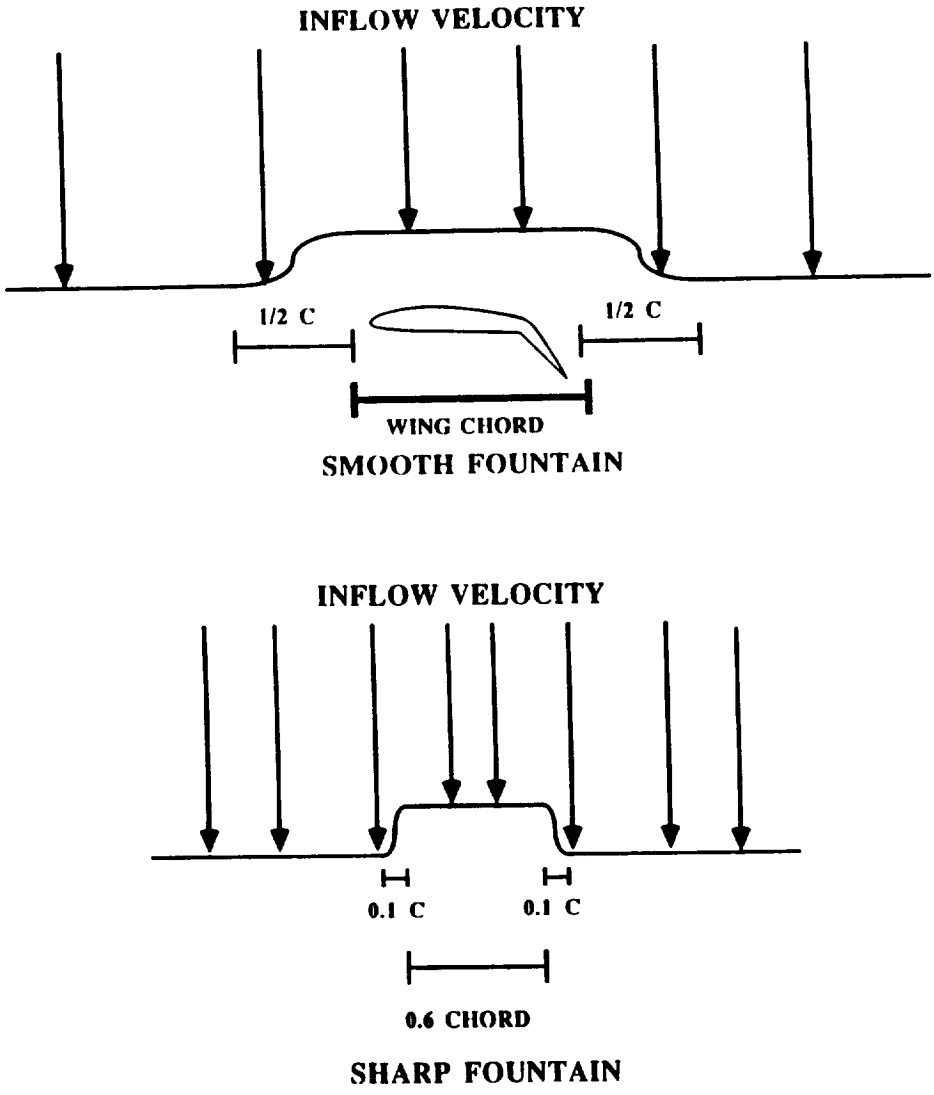

Figure 3.4 Schematic of rotor inflow velocity profile showing 'sharp' and 'smooth' fountain models.

data was available for the advanced airfoil section A triangular loading distribution was implemented. CAMRAD data for the VR7, VR8, and VR43030 blade element coefficients of lift and drag were used to determine the blade element loading. (This data and all related ATB data was obtained from Ken Rutledge at Lockheed Engineering and Sciences Company, Hampton, Virginia.) The chordwise compact (triangular loading) assumption will be shown to be a good assumption. The availability of more accurate CAMRAD lift and drag data, tabulated as a function of angle of attack and Mach number, allows for a more accurate spanwise loading distribution.

3.3 Comparison of Metal Blade Calculations With Experiment

The model used here to compare to the XV-15 test include chordwise accurate loading distributions based on the method of Abbot and Von Doenhoff as described above. The sharp fountain model was used as described in appendix C. The observer geometry is shown in figure 3.5 for the following predictions. Operational and rotor characteristics are given in appendix A. Figures 3.6 and 3.7 show comparisons for near in-plane observer locations in front and behind the aircraft. The predicted spectra are corrected to account for the experimental conditions which included two rotors and ground plane microphones. The ground plane microphones effectively double the acoustic pressure and the two rotors are considered here to be uncorrelated sources which double the acoustic energy. Thus the single rotor free field predictions are increased by 9 dB for comparison.

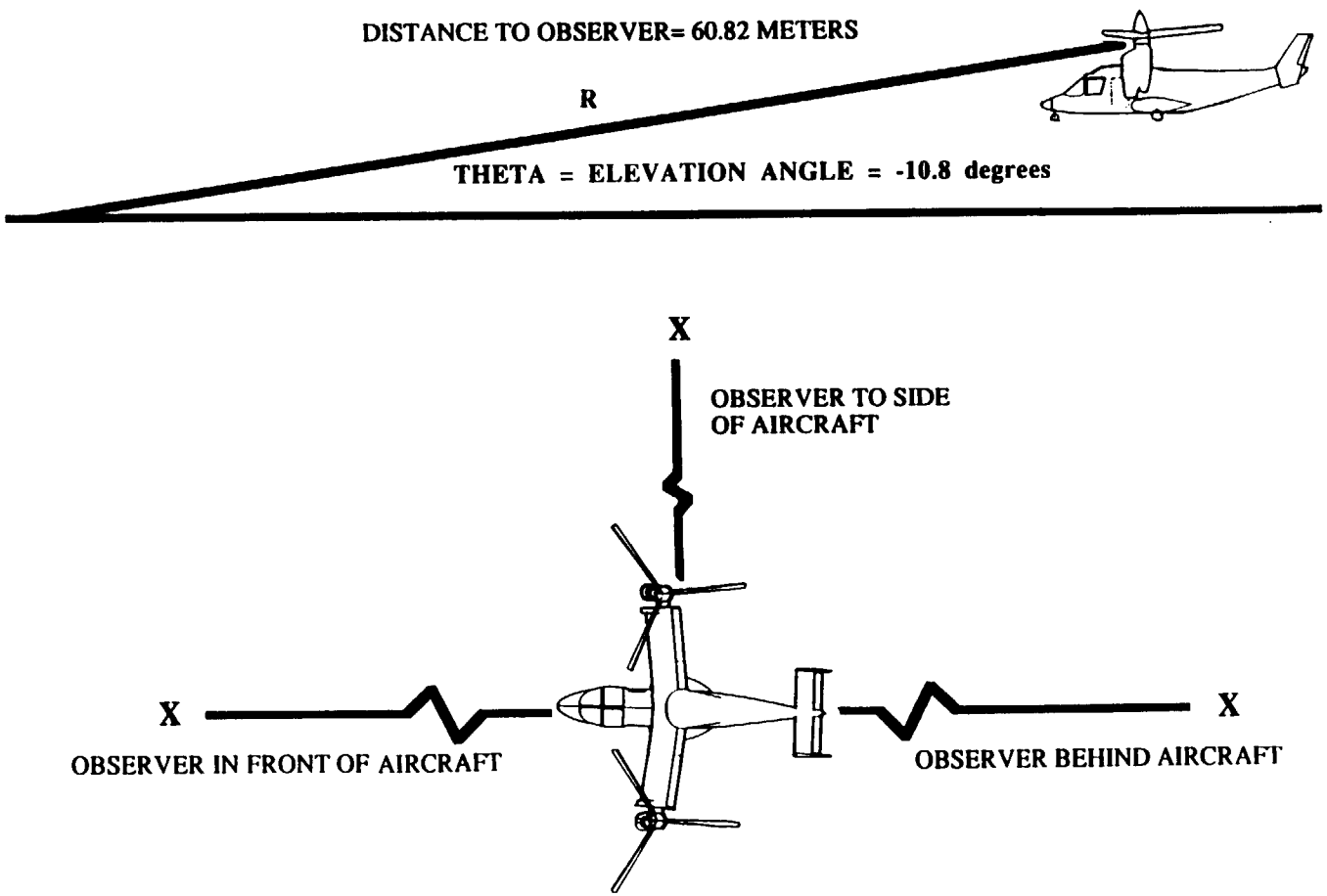

Figure 3.5 Observer geometry for near in-plane acoustic predictions.

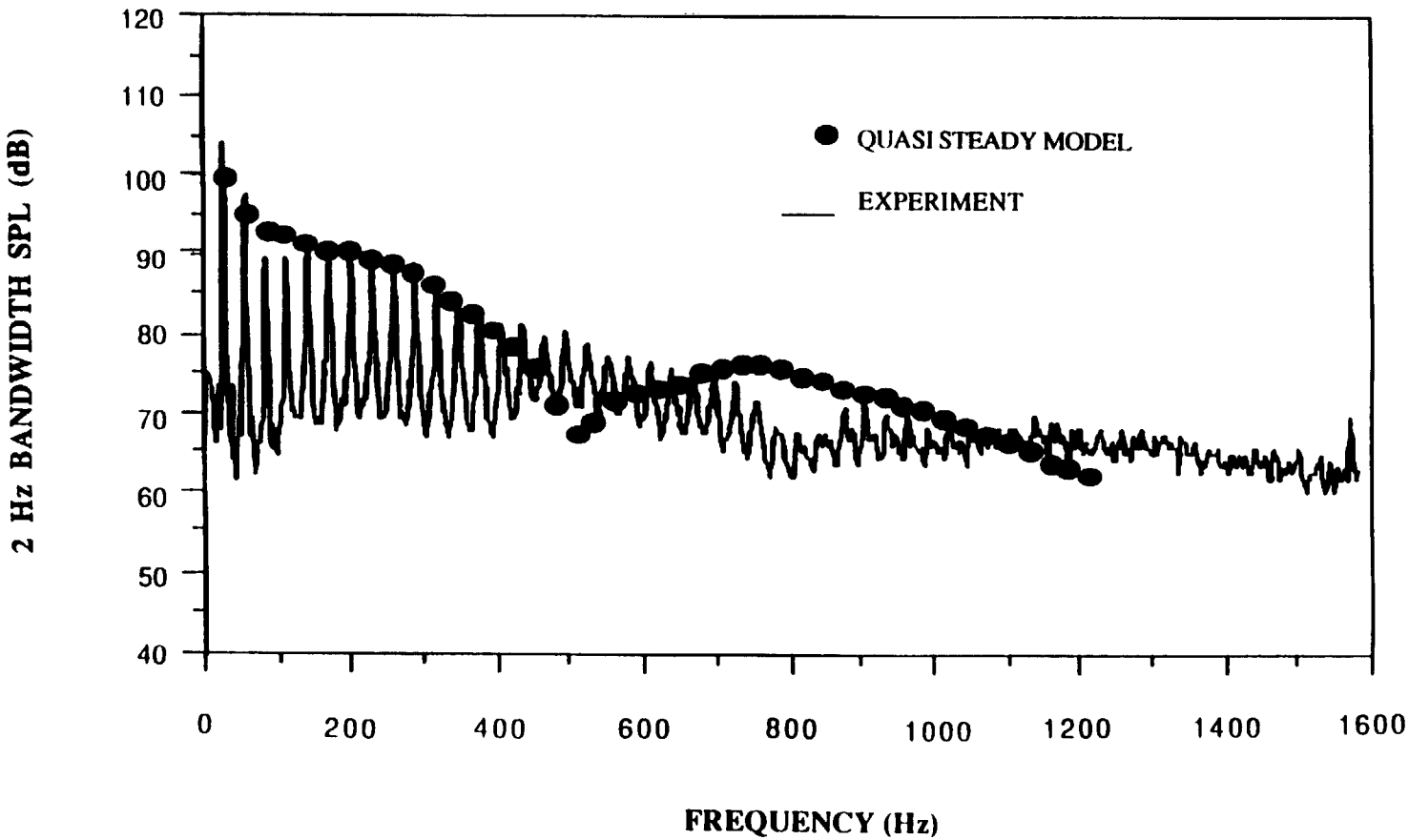

Figure 3.6 Comparison of discrete sound spectrum with experiment. Sharp fountain model. Near in-plane rear aircraft acoustics. Metal blade geometry. Quasi-steady and chordwise accurate blade loading.

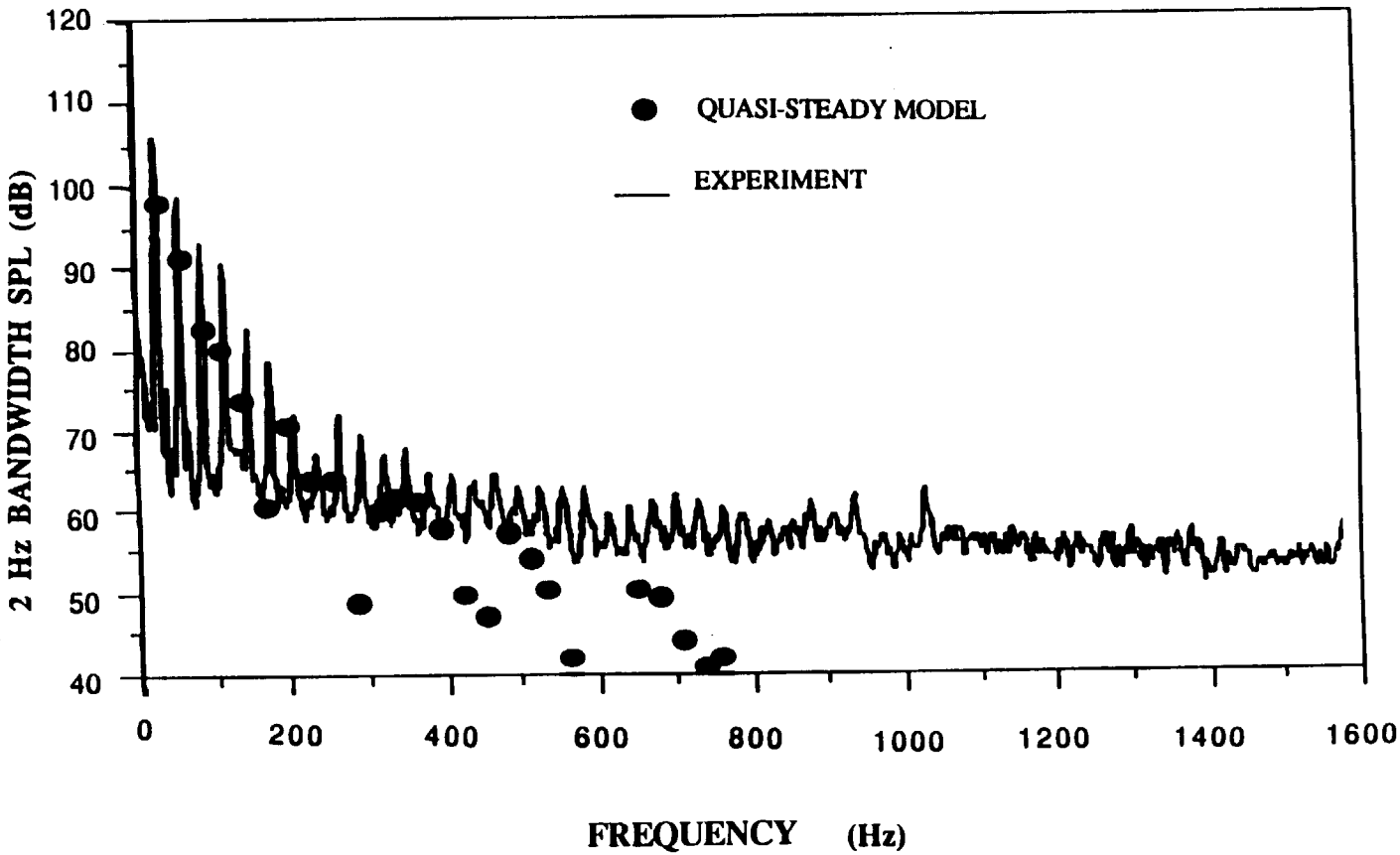

Figure 3.7 Comparison of discrete sound spectrum with experiment. Sharp fountain model. Near in-plane front aircraft acoustics. Metal blade geometry. Quasi-steady and chordwise accurate blade loading.

As seen in figures 3.6 and 3.7, the predictions are in good agreement with with the experimental spectra. Considering the rear acoustics shows that the fundamental harmonic of the prediction is ~5 dB low, but harmonics 2-15 are well predicted. The front acoustics are not as well predicted in level, but the trends are captured which indicates that the predictions capture the directionality of tilt rotor hover noise. Overall, these predictions indicate that tilt rotor hover discrete noise can be predicted using the fountain model with acceptable accuracy. A more extensive set of comparisons is presented in section 3.6.2 based on more recent XV-15 acoustic tests which use the ATB blades.

3.4 Scalloping Effects in Noise Predictions

The scalloping in the prediction, (see also figure 3.34), which is not apparent in the experiment can be explained. The scalloping in the prediction is due to the periodic nature of the blade/fountain interaction and the mathematical definition of the fountain model. This functional definition causes a pattern of increasing and decreasing amplitudes of the Fourier components of the predicted acoustic signal. Figure 3.12 demonstrates how different functional definitions of the fountain cause different scalloping patterns. The scalloping pattern is essentially related to the time and length scales of the functional definition of the fountain model. These time and length scales reflect a Doppler shifted composite time, the time it takes for the blade elements to pass through the fountain, and some characteristic width associated with the fountain. The time and

length scales then determine a fountain "frequency" and harmonics which results in frequency modulation or scalloping.

As seen in chapter II, the fountain flow is a time varying phenomenon and is changing positionally and in shape and magnitude. For the experimental spectra, many time traces are considered, and their spectra are averaged. The scalloping is obliterated due to averaging the spectra of time signals which vary significantly depending on the fountain flow variations. This variability is shown if figures 3.8a and 3.8b which show two instantaneous spectra for the ATB blades taken over approximately 4 blade passages. One can see variations in the discrete noise of up to 20 dB. Barely noticeable scalloping appears in these figures as these spectra contain more than one blade passage which averages out the effect. The over and under prediction of the higher harmonics can be attributed to the scalloping in the predictions which are averaged out of the experiment.

3.5 Aeroacoustic Experiments Using WOPWOP

Many modifications and refinements were made during the development of the current model. This process of refinement provided several insights into the effects of aerodynamic and blade loading parameters on the noise spectrum of the XV-15 rotor. Different parameters studied include the aeroacoustic effect of the presence of the fountain, a study of the effects of the fountain geometry on the acoustic signal, the effects of chordwise loading distributions, and the effect of dynamic blade loadings due to the impulsive loading changes

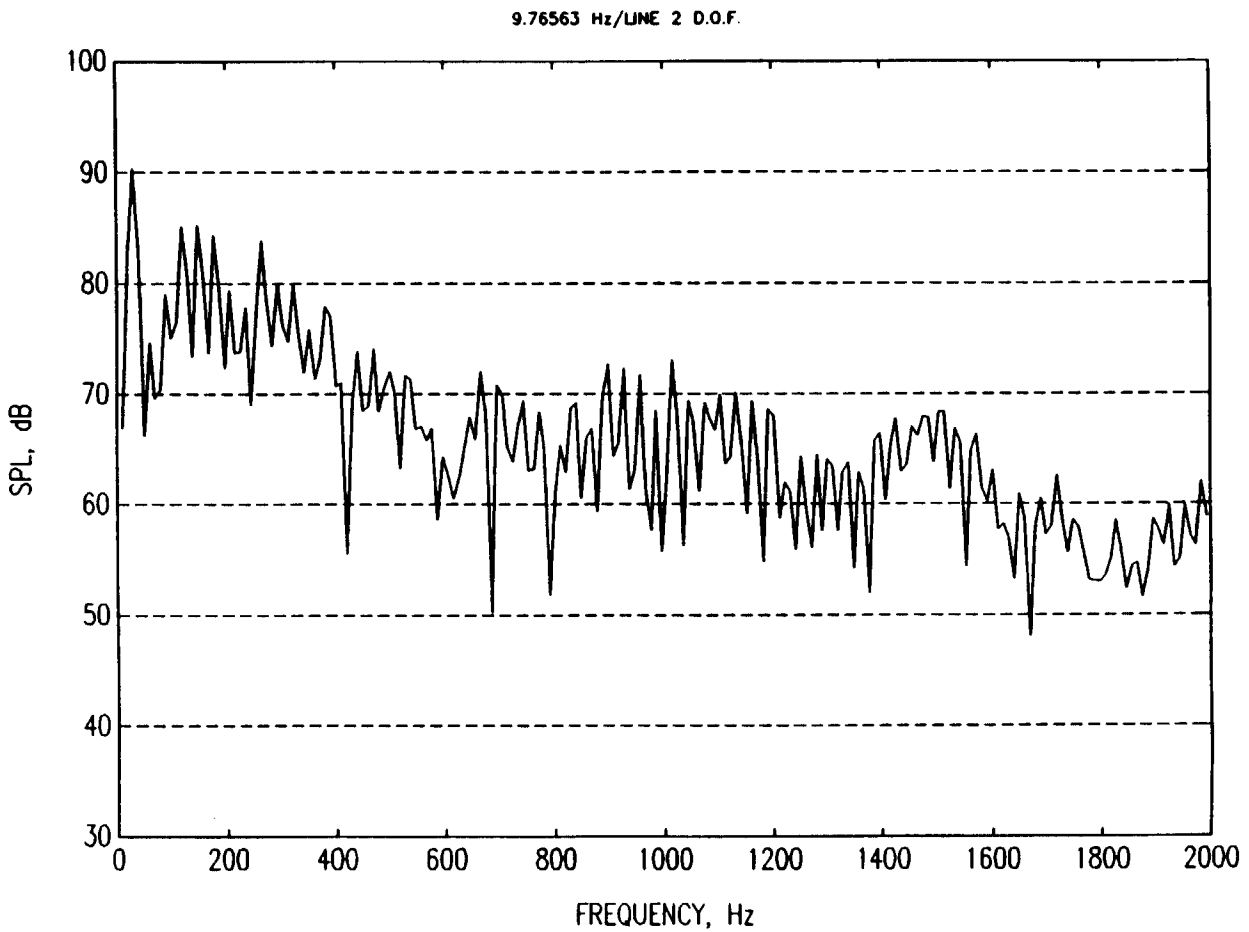

Figure 3.8a Sound spectrum based on four blade passages (signal periods). ATB geometry. Observer distance = 218 m. Polar angle = 45.7°. Rear Acoustics. RPM = 589.

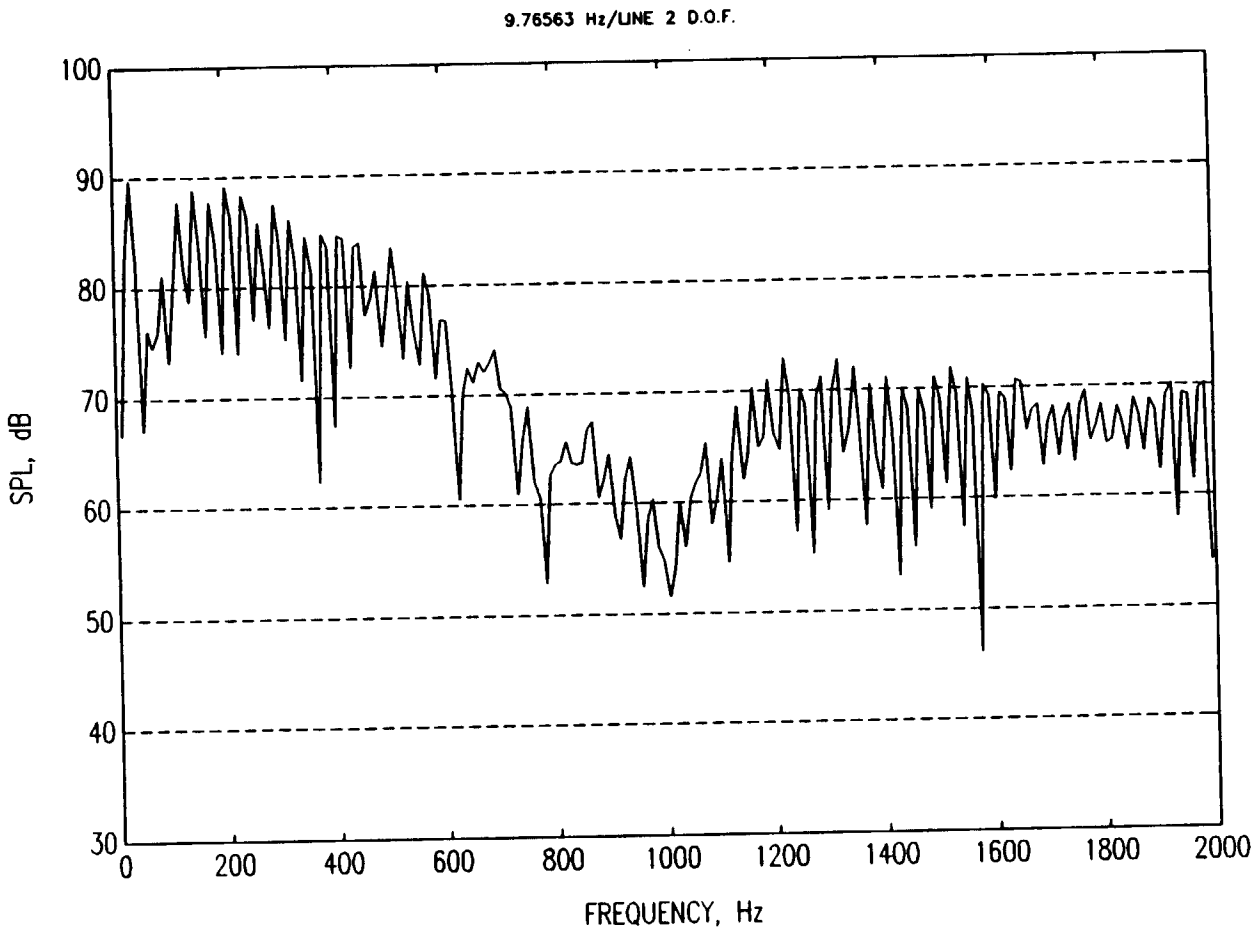

Figure 3.8b Sound spectrum based on four blade passages (signal periods). ATB geometry. Observer distance = 218 m. Polar angle = 45.7°. Rear Acoustics. RPM = 589.

3.5.1 Fountain Effect on Loading Noise

Figure 3.9 shows a prediction, (waveform and spectrum), without the fountain effect, ie. azimuthally constant loading. In this figure, and wherever indicated, "Levels not corrected for experiment" means that the figure shows a single rotor, free field microphone calculation, and the results of the calculation cannot be directly compared to experimentally obtained results. This prediction demonstrates the relative importance of thickness and loading noise for this near in-plane case behind the aircraft. With the exception of the first harmonic, the monopole or thickness source is the dominant source of sound radiation in-plane. The lift dipole is perpendicular to the blade chord. The highly twisted blades of the XV-15 tend to cause both mechanisms to radiate sound outside of the simple radiation patterns usually associated with a rotating acoustic dipole and monopole. The blade twist provides a spanwise variation in orientation of the sources. Thus the loading noise is only a few dB less than the thickness noise for this near in-plane case, whereas one might expect the thickness noise to be of much greater magnitude.

The inclusion of the fountain effect in the WOPWOP calculations caused a significant increase in the predicted sound levels. Figure 3.10 compares the acoustic wave form and spectra for predictions made with and without the fountain effect. This figure shows how the high noise levels associated with the fountain flow noise mechanism make it the dominant sound source. Because of the highly twisted blades, the fountain sound mechanism

C-2

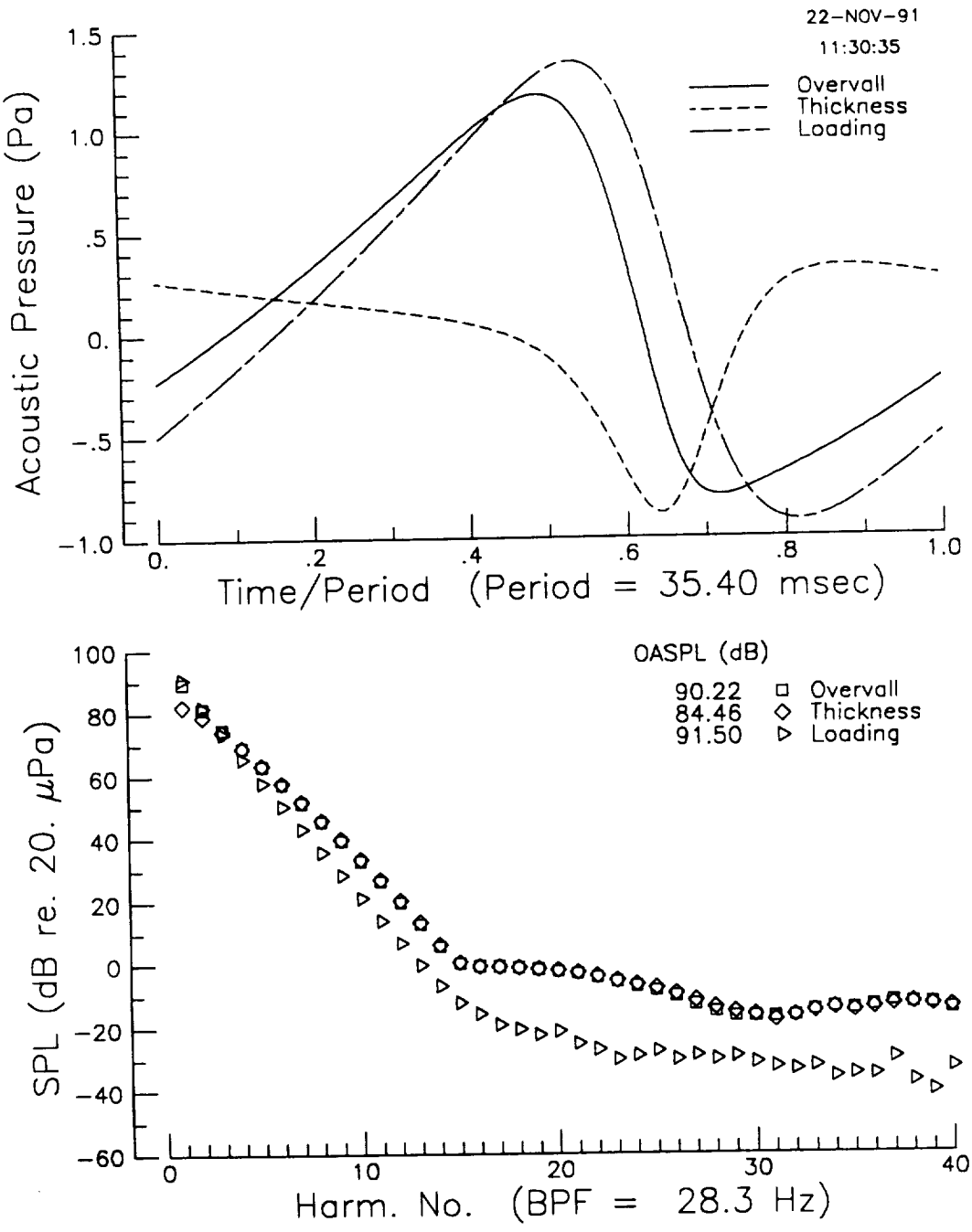

Figure 3.9 **Prediction without the fountain model showing thickness, loading and overall sound levels. Acoustic pressure time history and sound spectrum. Levels not corrected for comparison to experiment.**

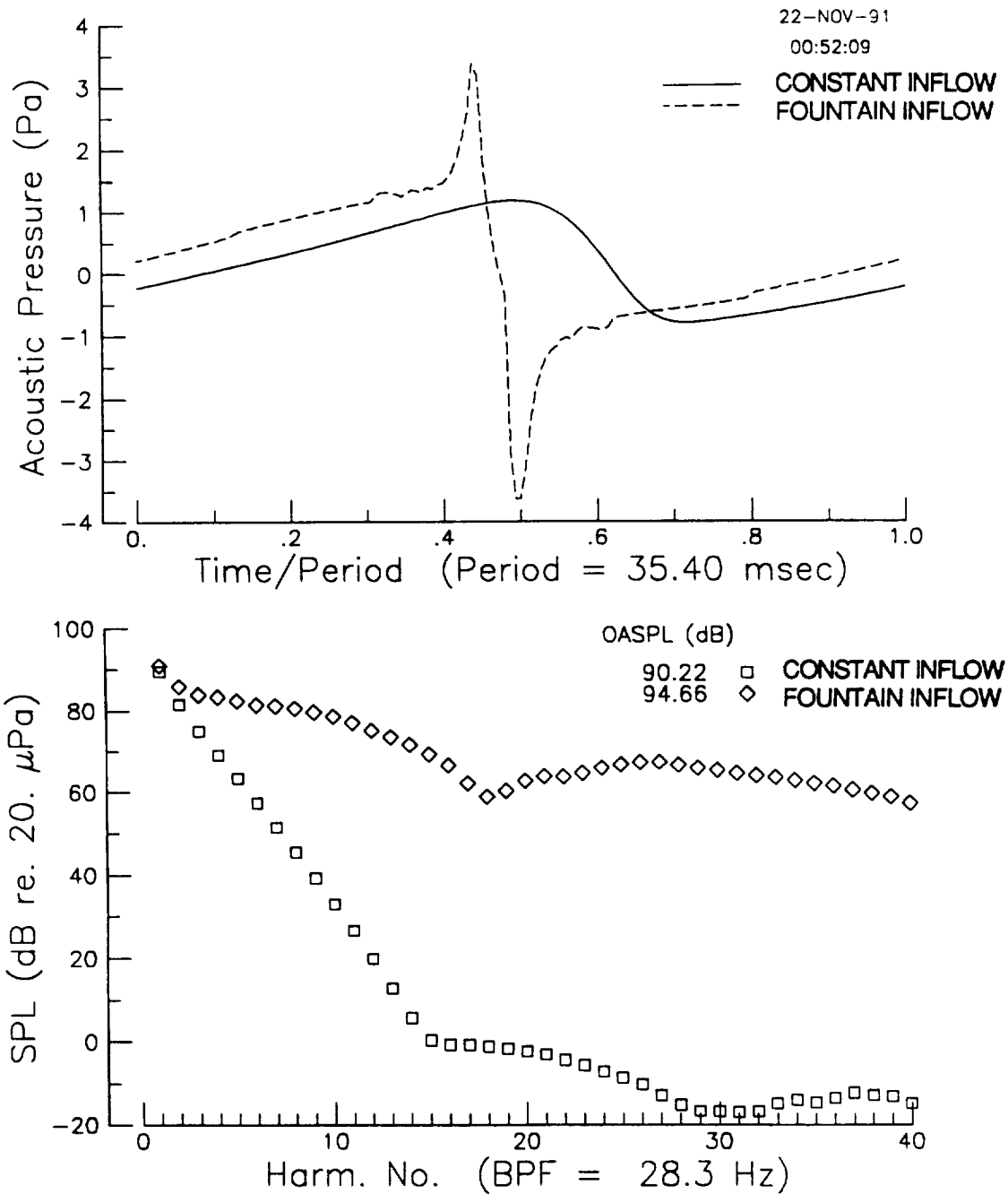

Figure 3.10 Comparison of 'sharp' fountain model calculation to no fountain model calculation. Overall noise. Acoustic pressure time history and sound spectrum. Near in-plane rear aircraft acoustics. Levels not corrected for comparison to experiment.

radiates sound in all observer directions including this near in-plane case. The fountain mechanism stems from the azimuthally varying inflow conditions. The changing inflow causes a change in blade element angle of attack. This makes the blade loading become a function of time in a blade fixed coordinate system. Figure 3.11 shows a plot of the time derivative of blade surface pressure for three spanwise stations. The acoustic pressure is proportional to $\frac{dF}{dt}$ where F is the force on the fluid. Thus one can write for a blade fixed coordinate system:

$$p' \propto \frac{dP}{dt} \tag{3.7}$$

where p' is the acoustic pressure and $\frac{dP}{dt}$ is the time derivative of the blade surface pressure. Figure 3.11 shows that $\frac{dP}{dt}$ is zero over the rotor disk except in the fountain region. This physically explains the fountain noise mechanism. $\frac{dP}{dt}$ also approximates the acoustic waveform of the fountain mechanism at each radial station. The acoustic signal in the observer fixed coordinate system will be a time shifted sum of the acoustic signal generated by each radial station. Comparing figure 3.11 with figure 3.10 which shows the acoustic signal calculated by WOPWOP illustrates this point. One should also note that fountain mechanism does not affect the thickness noise for obvious reasons.

Two fountain models were developed: the 'sharp' inflow variation was characterized by a sharp decrease in inflow velocity

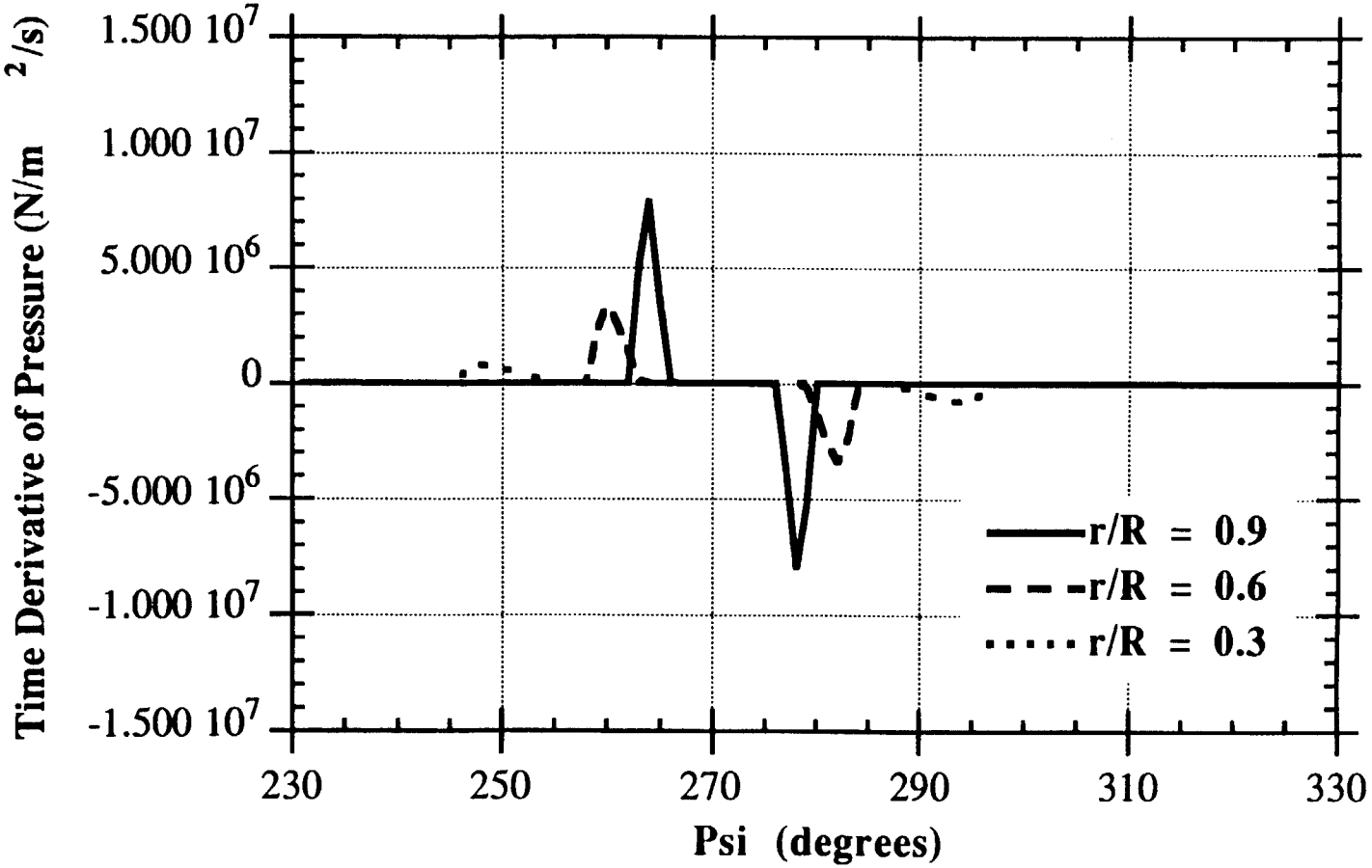

Figure 3.11 Time derivative of blade element quarter chord pressure as a function of azimuth. Quasi-steady blade response. Fountain effect centered on Psi = 270°. Metal blade geometry.

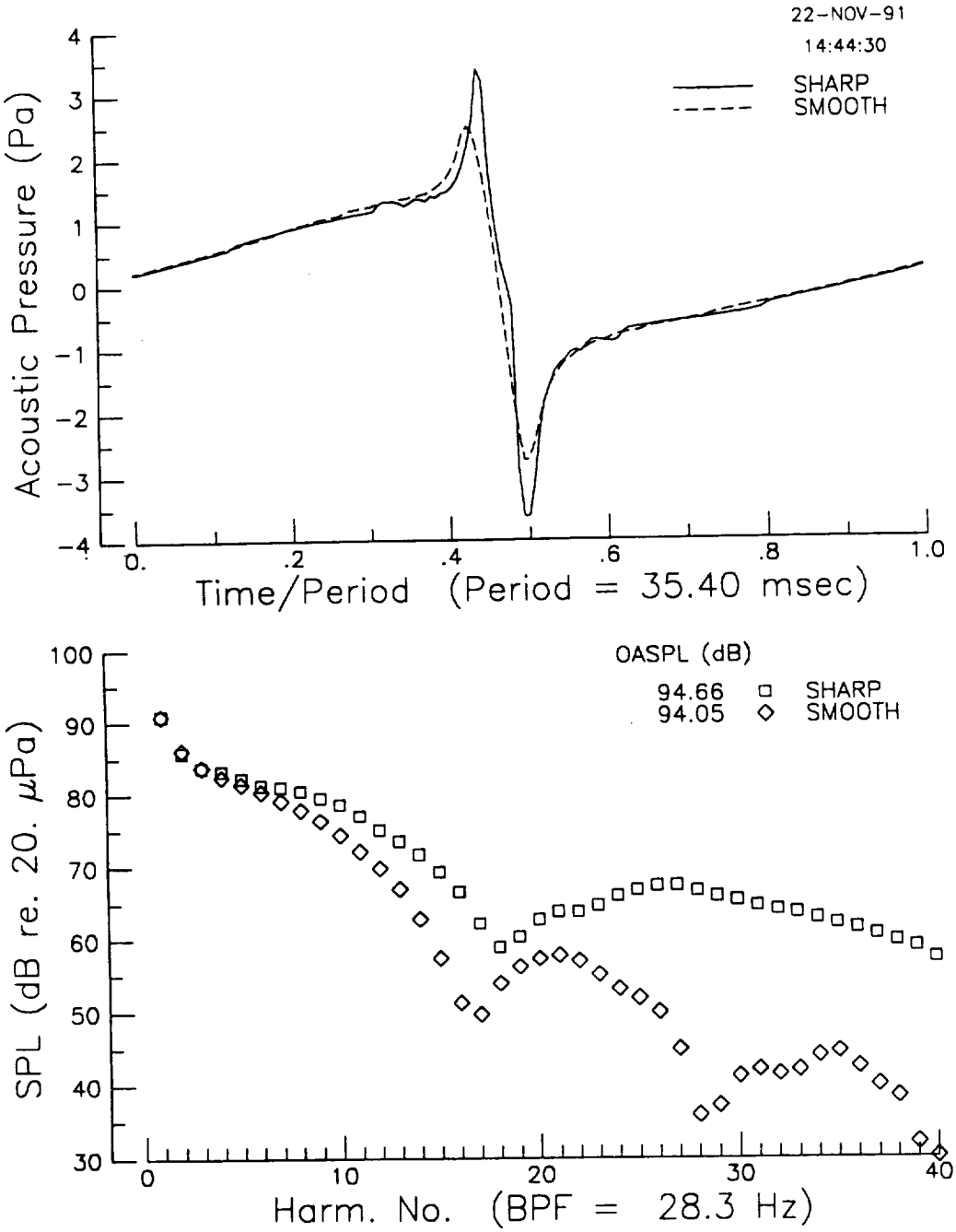

Figure 3.12 **Comparison of predictions with 'sharp' and 'smooth' fountain models. Overall noise. Acoustic pressure time history and sound spectrum. Near in-plane rear aircraft acoustics. Levels not corrected for comparison to experiment.**

over the wing and the 'smooth' inflow variation was characterized by a gradual decrease in inflow velocity (see appendix C for details). Predictions for a rearward observer location are compared in figure 3.12 for the two fountain models. The sharp fountain model has a spikier acoustic wave form of slightly greater amplitude. As would be expected, this results in higher spectral amplitudes for the higher discrete harmonics. The overall sound pressure levels are approximately equal for the two fountain models.

3.5.2 The Effects of Chordwise Loading Distributions

As user input, WOPWOP requires the pressure on the blade surface as a function of azimuth, radial station and chordwise position. The problem lends itself to a 2-D blade element simplification The loading characteristics of each radial station are calculated as if for a 2-D airfoil in a steady flow.

Modelling a chordwise accurate pressure distribution on the rotor is complicated by the need for the loading distribution to be a function of angle of attack, Mach number and the flow conditions (attached or separated flow for example). For standard NACA airfoils, the chordwise pressure distribution can be approximated using the velocity addition method of Abbott and Von Doenhoff[22]. This method is accurate for slender airfoils at small angles of attack (fully attached flow) and low Mach numbers.

However, this method was not applicable to the ATB blades as they are not standard NACA airfoils. The development of the dynamic lift model for the metal blades also precluded the use of the velocity addition method. A simplifying assumption was to

model the chordwise loading with a triangular loading distribution. This simplification was based on the premise that the loading distributions are approximately acoustically compact; the chordwise loading distribution is unimportant for computing the noise signal for the discrete frequencies of interest.

The conditions for compactness given by Farassat[20] are that the distance from the source to observer should be much greater than the length scale of the source. Also, the time taken for the collapsing sphere to cross the body should be much less than the period of the sound fluctuation. This implies the following compact limits:

$$r_{obs} >> \text{chord} \tag{3.8}$$

$$\frac{\text{chord} \cdot c_0}{(1.- M_{tip})} << \frac{1}{\text{frequency}} \tag{3.9}$$

For the case of the XV-15 in hover, M_{tip} = 0.65, the chord @ 90% radius = 0.34 meters, and assume a speed of sound of 340 m/s. This implies that the accuracy of the chordwise pressure distribution is unimportant for frequencies less than 350 Hz.

The compactness assumption was tested by comparing the WOPWOP calculations of three different chordwise distributions for the XV-15 using the standard metal blades which employ NACA 64 series airfoils. The three distributions were constant chordwise loading, a triangular loading distribution where the maximum pressure occurred at the 1% chord point, and a chordwise accurate

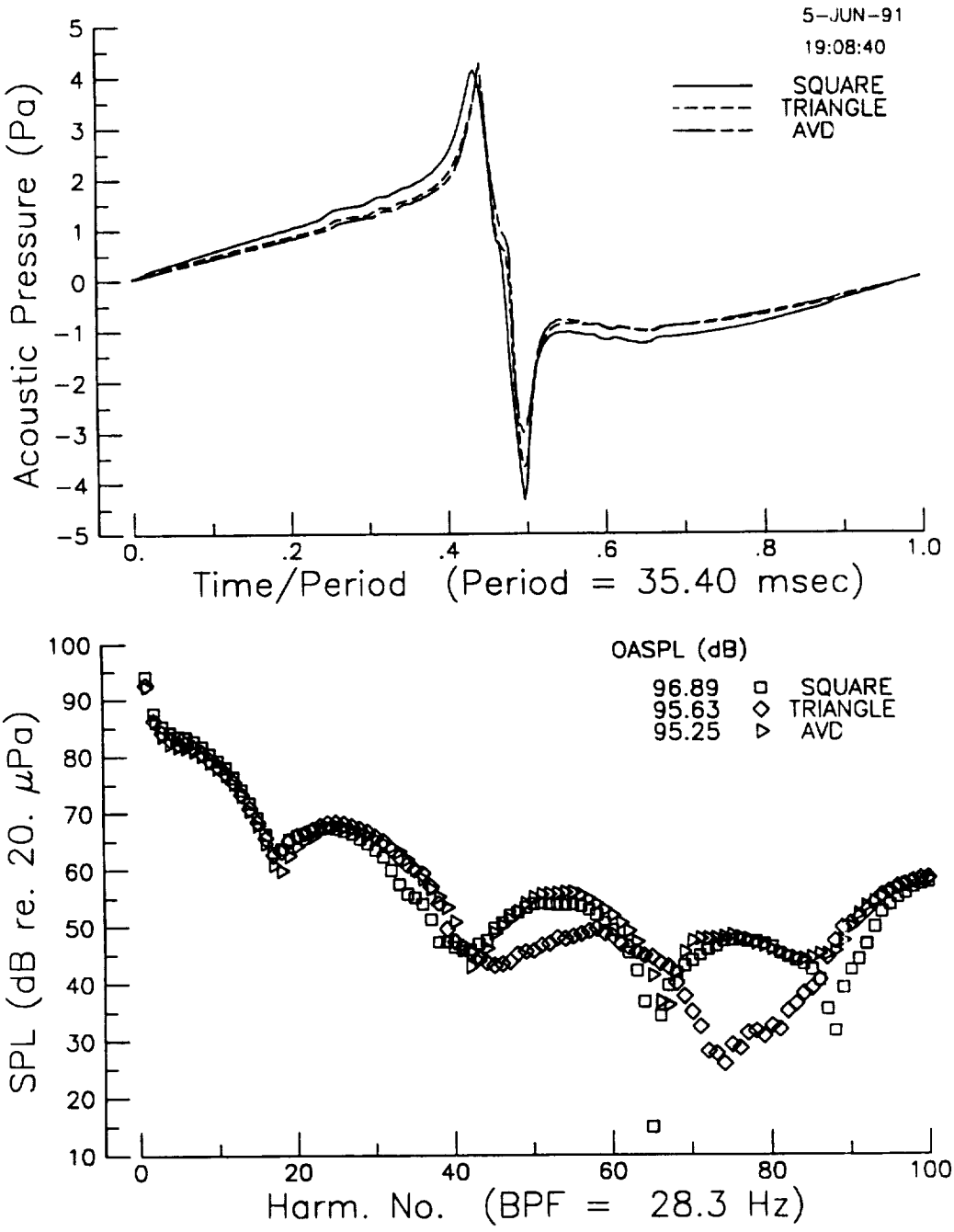

Figure 3.13 Comparison of predictions with different chordwise loading distributions. Loading noise. Square: constant chordwise loading. Triangle: triangular loading distribution. AVD: chordwise accurate loading distribution. Levels not corrected for comparison to experiment.

pressure distribution calculated using the velocity addition method of Abbott and Von Doenhoff. The total lift on each blade element was the same for the three loading distributions. A near in-plane observer location to the rear of the aircraft (the same conditions as the previous predictions) was chosen so as to maximize the Mach number of the blade as it passed through the fountain moving towards the observer. This maximizes the Doppler shift and amplification. The results of these calculations are shown in figure 3.13. The spectra are very close out to about 800 Hz. The triangular loading distribution is shown to be a valid and accurate simplification. Also note that the OASPL differs by less than half a dB for the triangular loading and chordwise accurate loading cases.

3.5.3 The Effects of Dynamic Airfoil Response

Dynamic lift effects on the rotor blade were modeled using Leishman and Beddoes' semi-empirical dynamic stall model.[24,25] This model is presented in a form which is consistent with an indicial formulation. It accounts for the unsteady growth and decay of lift in response to angle of attack changes. The onset of vortex shedding is represented by a criterion for leading edge or shock induced separation based on a critical leading edge pressure. Induced vortex lift and its convection and decay are represented empirically. Nonlinearities associated with trailing edge separation are represented using a Kirchhoff flow model in which the separation point is related to airfoil behavior.

This model is formulated in terms of a superposition of two indicial aerodynamic responses to forcing. An indicial function

defines the response to a disturbance which is applied instantaneously at time zero and held constant thereafter, ie a step function change in angle of attack. These responses consist of an initial noncirculatory or impulsive loading, based on piston theory which decays rapidly with time, and a circulatory loading which builds with time to the steady state value. These response functions are shown in figure 3.14 for a NACA 0012 airfoil subjected to a 2° step change in angle of attack. C_N is the normal force coefficient of the airfoil

Duhamel's principle[26] is used to derive the net response based on these two indicial response components to step functions for any arbitrary forcing function. In this case, the forcing function is the time history of the blade element angle of attack. The response of a linear system, (indicial response functions may then be summed), to an arbitrary forcing function can be regarded mathematically as a summation of successive step functions. The response of an airfoil is then a summation of the airfoil responses to the individual step changes in angle of attack. Let $\Delta\alpha(\tau)$ be the magnitude of each step change in angle of attack over a time interval $\Delta\tau$. Let $A(t-\tau)$ be the indicial response at time t resulting from the unit step change in angle of attack initiated at time τ. Thus $A(t-\tau)$ corresponds to the sum of the impulsive and circulatory indicial response functions described above. The airfoil response to a single step change in angle of attack can be expressed as:

$$\frac{\Delta\alpha(\tau)}{\Delta\tau}\,\Delta\tau\; A(t-\tau). \qquad (3.10)$$

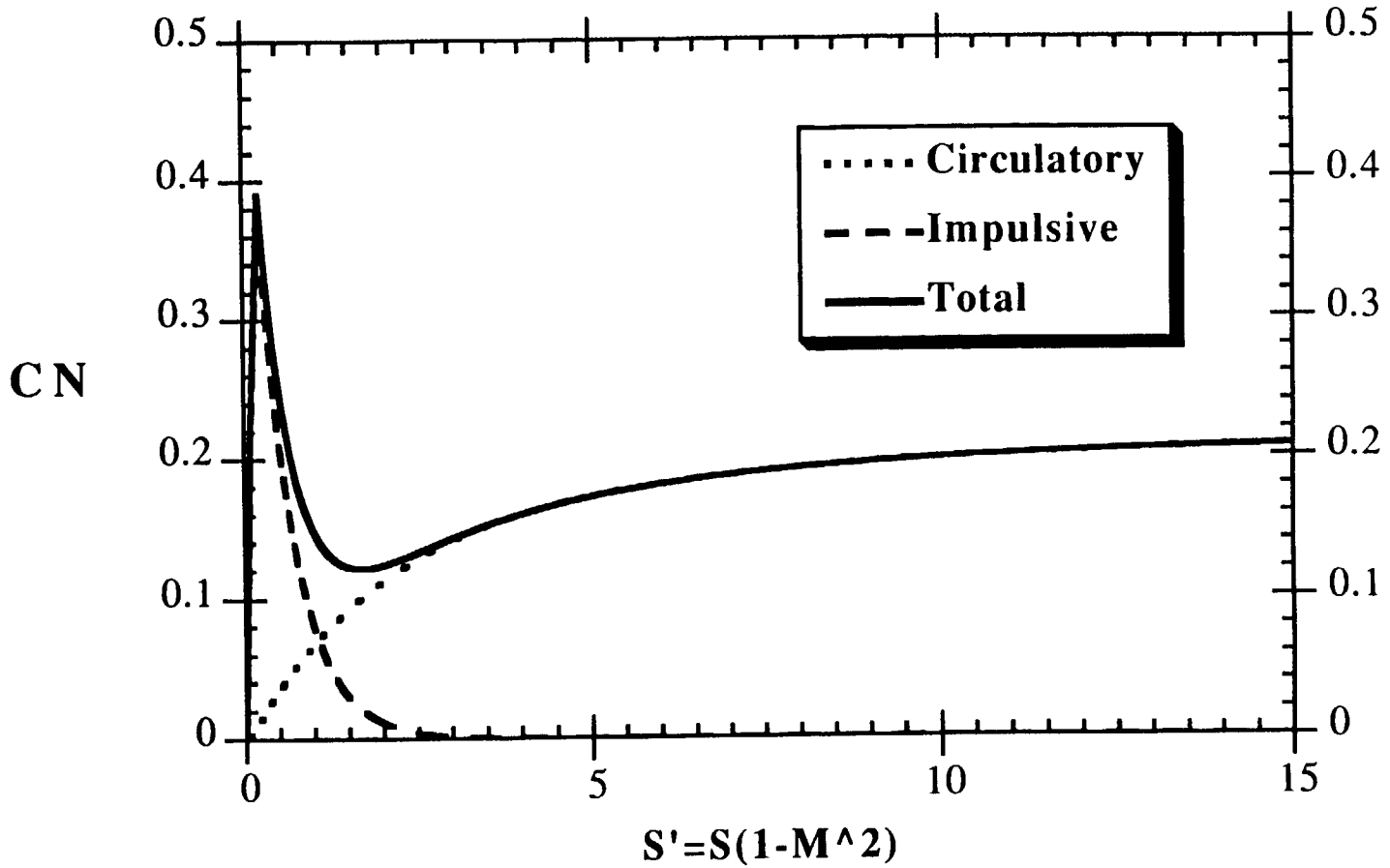

Figure 3.14 Blade element indicial response functions. M = 0.3. Step change in angle of attack, $\Delta\alpha$ = 2°. NACA 0012 airfoil. CN = normal force coefficient.

The response of a linear system to all the step functions initiated from $\tau = 0$ to $\tau = t$ is:

$$C_N(t) = \alpha(0)A(t) + \sum_{\tau=\Delta\tau}^{\tau=t} \frac{\Delta\alpha(\tau)}{\Delta\tau} A(t-\tau)\,\Delta\tau. \qquad (3.11)$$

Taking the limit as $\Delta\tau$ goes to zero gives the superposition integral or Duhamel's integral:

$$C_N(t) = \alpha(0)A(t) + \int_0^t \alpha'(\tau)\, A(t-\tau)\, d\tau. \qquad (3.12)$$

The attached flow airfoil response can then be found by numerically solving equation 3.12 with the given indicial response functions. The algorithm for doing this is given in references 24 and 25 and is used here. One should note that these indicial response functions are semi-empirical.

The superposition integral is only valid for attached flow. The dynamic stall model of Leishman and Beddoes incorporates semi-empirical schemes for correcting the airfoil response due to trailing edge separation, stall, and reattachment. Two important dimensionless parameters are S, the dimensionless distance travelled by the airfoil, and k, the reduced frequency of the airfoil. They are defined as follows:

$$S = 2\frac{Vt}{c} \tag{3.13}$$

$$k = \frac{\omega c}{2V} \tag{3.14}$$

where c is the blade chord, V is the airfoil velocity and ω is the frequency of the forcing function.

To demonstrate the importance of dynamic stall as a sound mechanism, a stationary airfoil with a time varying loading was studied using the dynamic stall model of Leishman and Beddoes'. Figure 3.15 shows the dynamic lift and stall hysteresis for a NACA 0012 airfoil subjected to a sinusoidal change in angle of attack. This figure shows the dynamic lift, delayed separation and stall, and the reattachment process. Figure 3.16 shows this cyclic process as a function of time. The acoustic waveform can be found from the loading time history using the relation, $p'(t) = \frac{dF(t)}{dt}$. C_N is the normal force coefficient, so the acoustic waveform will look similar to $\frac{dC_N(t)}{dt}$. This derivative is calculated numerically and plotted in figure 3.17. This waveform clearly shows that the acoustic signal generated by a blade undergoing dynamic stall will radiate sound over a significant part of the frequency spectrum. Figure 3.18 shows a comparison between the dynamic stall loading and the steady response loading. The steady response signal is generated by assuming a linear response to changes of angle of attack, ie $C_N \propto \alpha$. Figure 3.19 shows a comparison between the waveform generated by an airfoil using dynamic response and steady

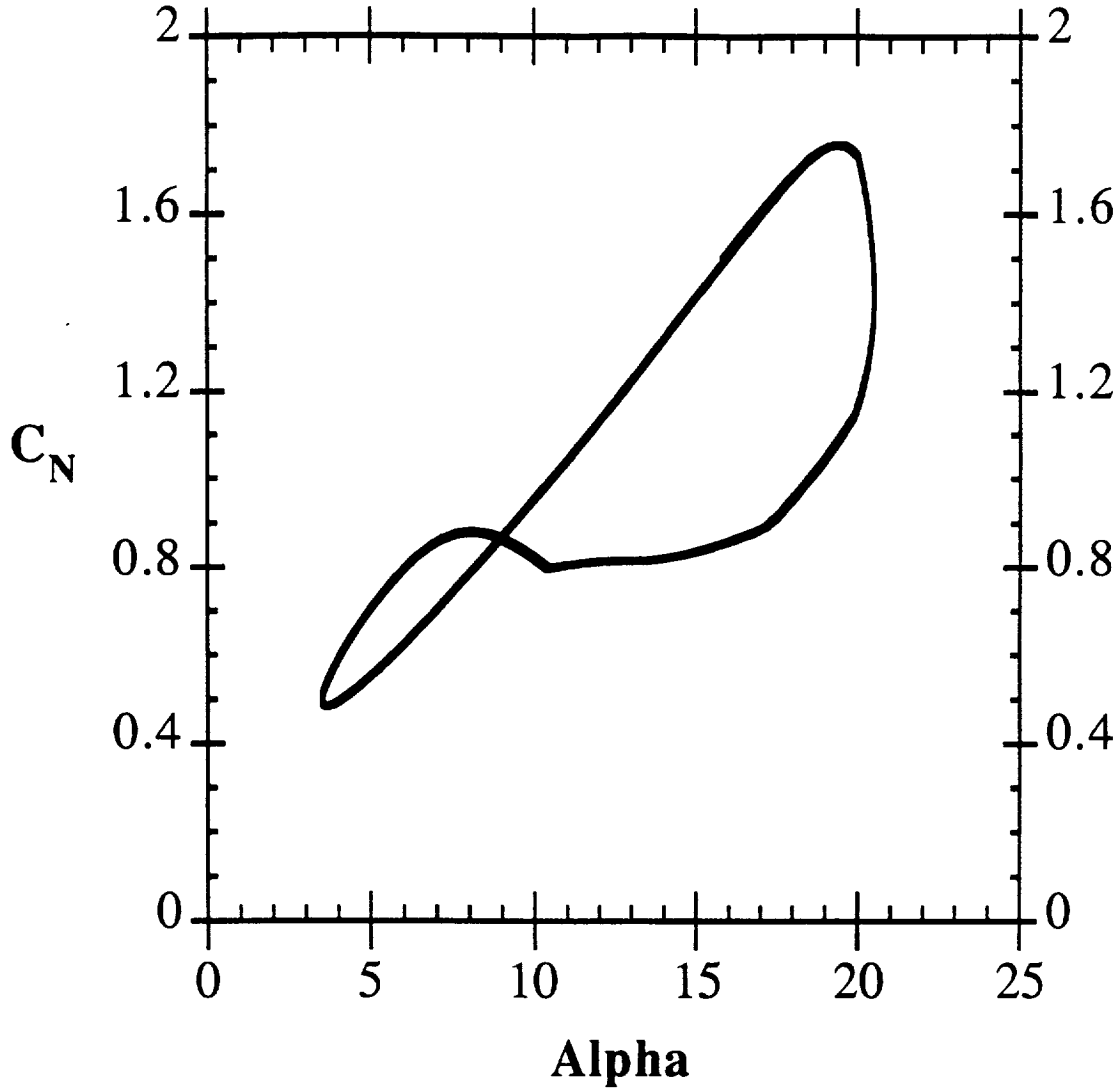

Figure 3.15 Dynamic stall hysteresis. $\alpha = 12 + 8.5 \sin(\omega t)$. $k = 0.1$. $M = 0.3$. chord = 0.34. NACA 0012 airfoil.

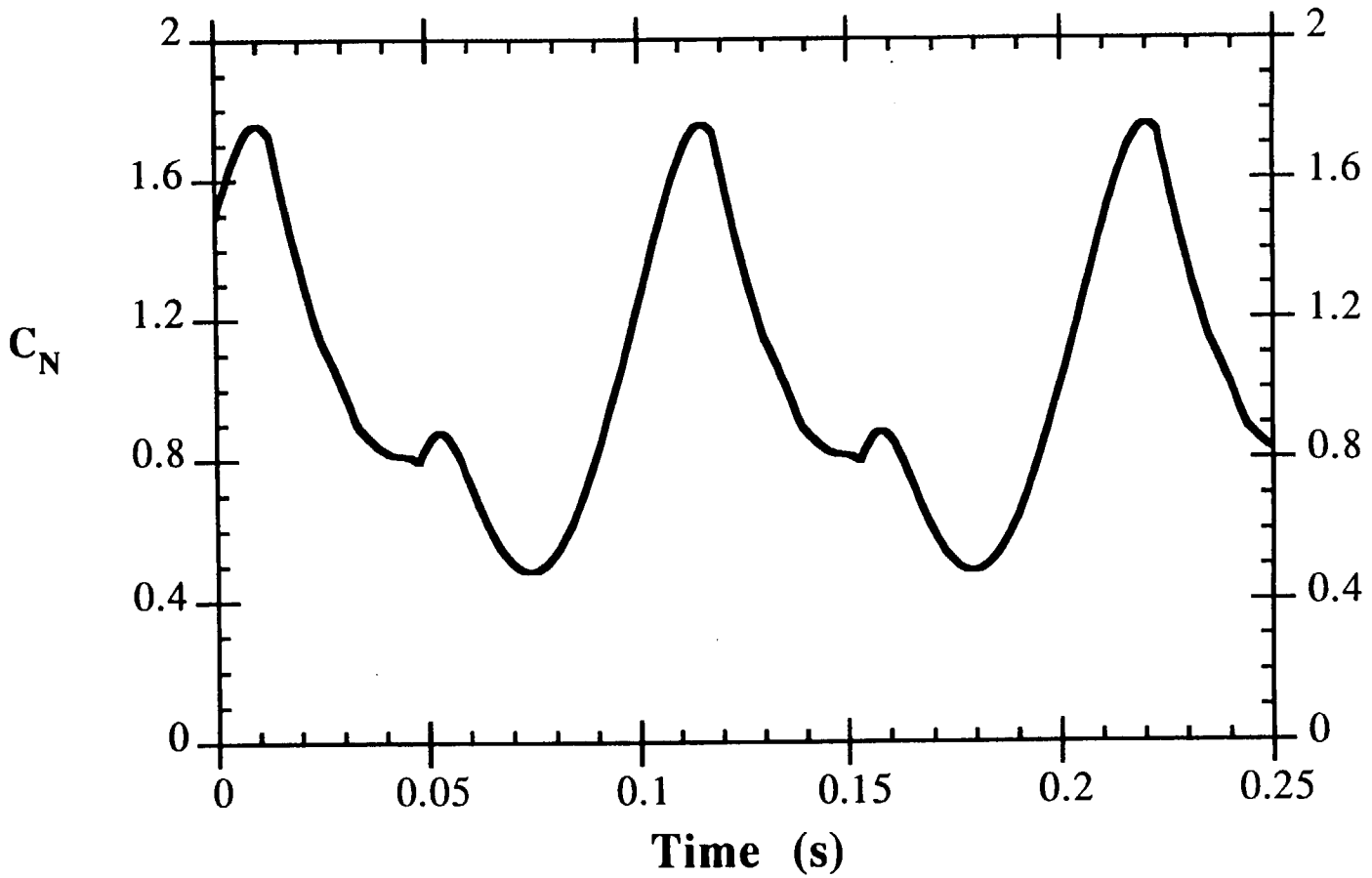

Figure 3.16 Dynamic stall hysteresis as a function of time. $\alpha = 12 + 8.5 \sin(\omega t)$. $k = 0.1$. $M = 0.3$. chord = 0.34. NACA 0012 airfoil.

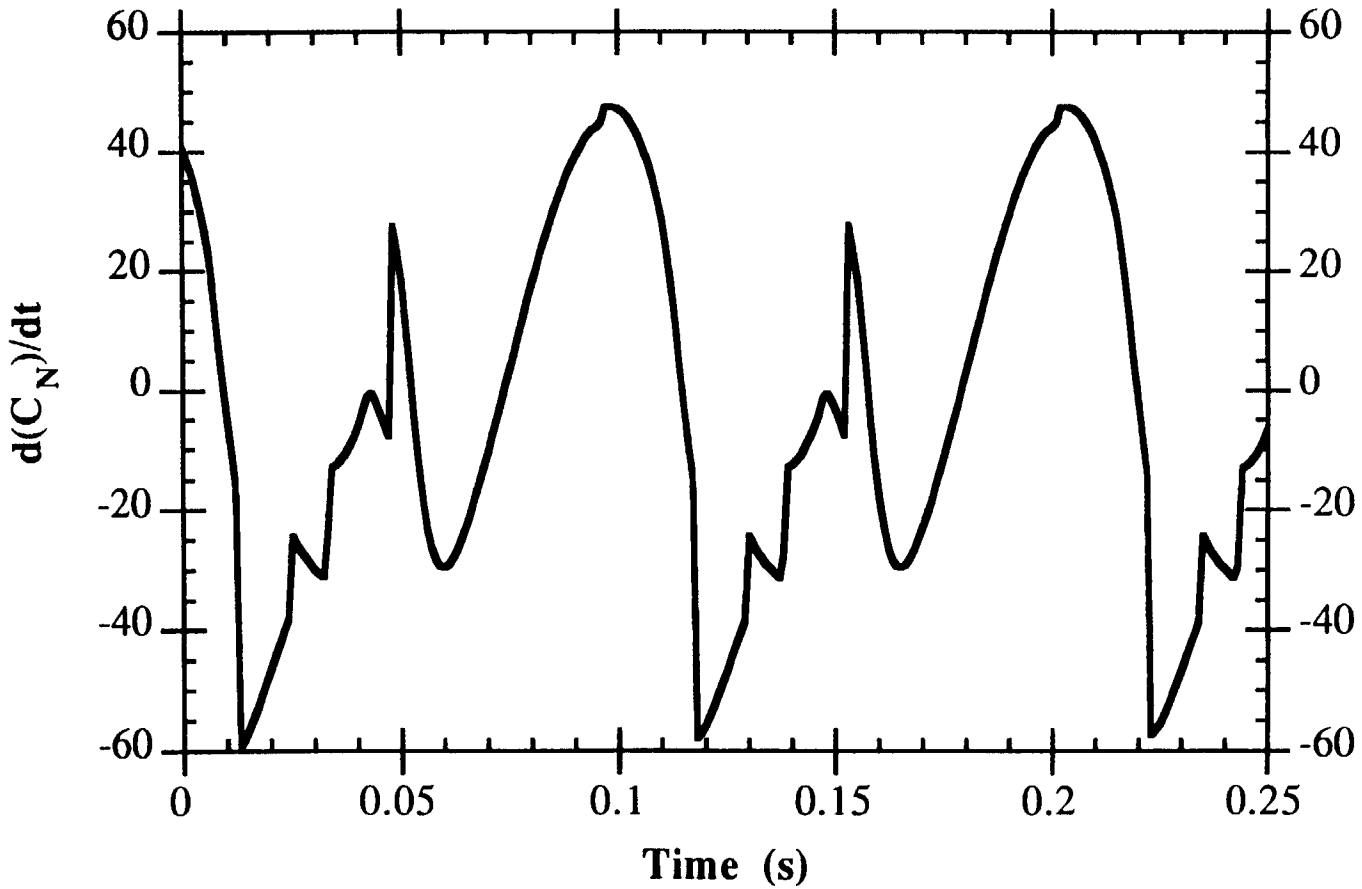

Figure 3.17 Acoustic waveform, $\frac{dC_N}{dt}$. $\alpha = 12 + 8.5 \sin(\omega t)$. $k = 0.1$. $M = 0.3$. chord = 0.34. NACA 0012 airfoil.

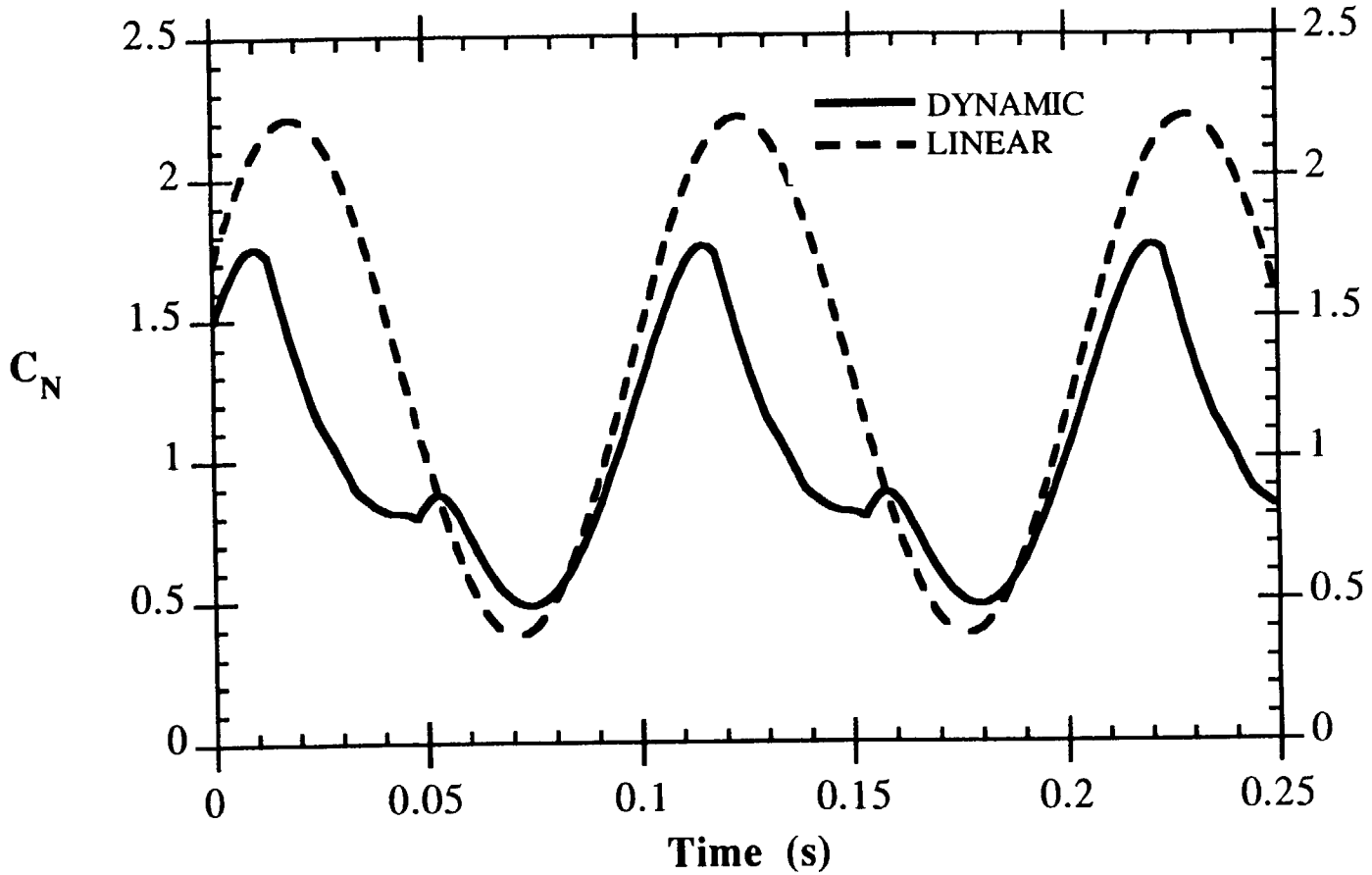

Figure 3.18 Comparison of $C_N(t)$ for dynamic and linear steady blade response. $\alpha = 12 + 8.5 \sin(\omega t)$. k = 0.1. M = 0.3. chord = 0.34. NACA 0012 airfoil.

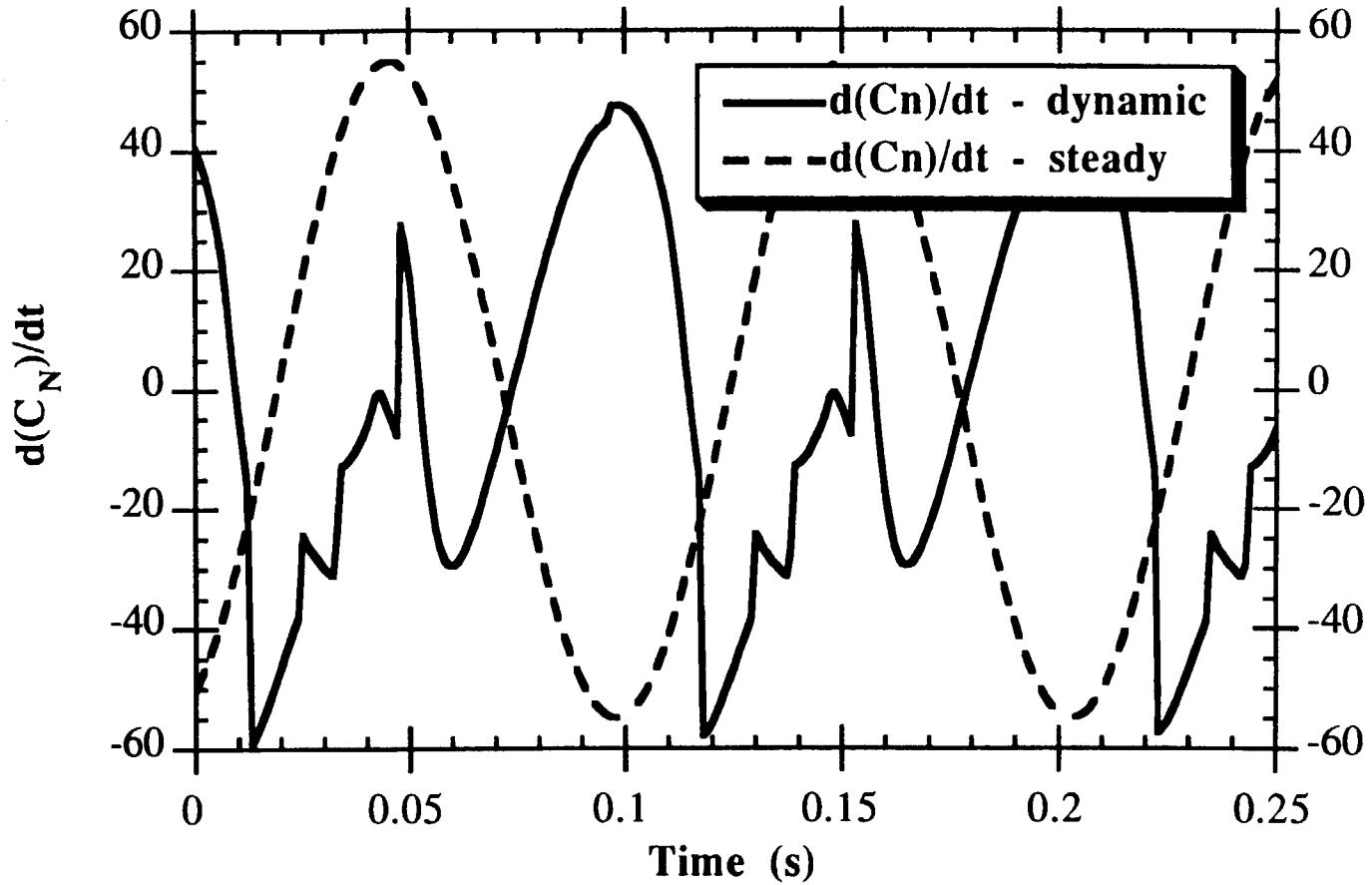

Figure 3.19 Comparison of acoustic waveform, $\frac{dC_N}{dt}$, for dynamic and linear steady blade response. $\alpha = 12 + 8.5 \sin(\omega t)$. $k = 0.1$. $M = 0.3$. chord = 0.34. NACA 0012 airfoil.

response to a sinusoidal varying angle of attack. The steady response will radiate sound only at the frequency of the forcing. This analysis indicates that the dynamic stall of an airfoil would be an important source of noise radiation across the frequency spectrum.

The above analysis is for a non-moving airfoil, (stationary source), with a sinusoidally varying angle of attack. An investigation of possible interest would be to study the effect of dynamic stall on a rotating rotor blade, (moving source). This could be accomplished by using this dynamic stall model with a rotor blade defined by constant spanwise properties and using WOPWOP to calculate the acoustic signature as the rotating blade undergoes stall and reattachment. Dynamic stall effects would be an important sound producing mechanism as the stall/reattachment hysteresis may result in significant time varying blade loadings. This mechanism would be an important source of sound for a rotor in forward flight as the retreating blade operates at high angles of attack.

The tilt rotor blades were carefully designed for hover and only inboard spanwise sections operate at high angles of attack. The change in angle of attack due to the fountain is not enough to cause stall over any section of the blade. However, the fountain flow causes an impulsive type loading which has dynamic characteristics. These include blade element over and undershoot responses to changes in angle of attack as well as a definite hysteresis as the blade makes a complete revolution. These effects

were modeled using the dynamic stall model of Leishman and Beddoes discussed above.

This method was developed and tuned primarily for the NACA 0012 airfoil. In order to apply this method to the NACA 64-series airfoil on the tilt rotor blades, we used the compressibility corrections for C_{Lmax} and $C_{L\alpha}$ and the time constants from the available NACA 0012 information[24]. Also, chordwise accurate loading distributions were not used. As seen in section 3.5.2, the triangular loading distribution simplification should not significantly affect the calculations. Thus the absolute accuracy of the lift predictions will not be expected to be high but they should be sufficient for these initial acoustic predictions.

The result of this indicial formulation is that the airfoil tends to overshoot the steady state lift value due to a change in angle of attack. This is caused by the impulsive indicial response function. Acoustically, the impulsive indicial response is more significant than the circulatory indicial response as it leads to more rapid changes in blade loadings. This effect can be seen in figure 3.20 which shows the lift response of an airfoil passing through a sharp fountain inflow velocity variation. Note the overshoots and decays due to the indicial response of the airfoil. The dimensionless distance, S, through the constant inflow part of the fountain zone is not long enough to build a significant circulatory response.

The physical mechanism by which the dynamic loading response generates sound is illustrated in figure 3.21 and figure 3.22. Figure 3.21 shows quarter chord pressure as a function of azimuth. The indicial response over and under-shoots are apparent

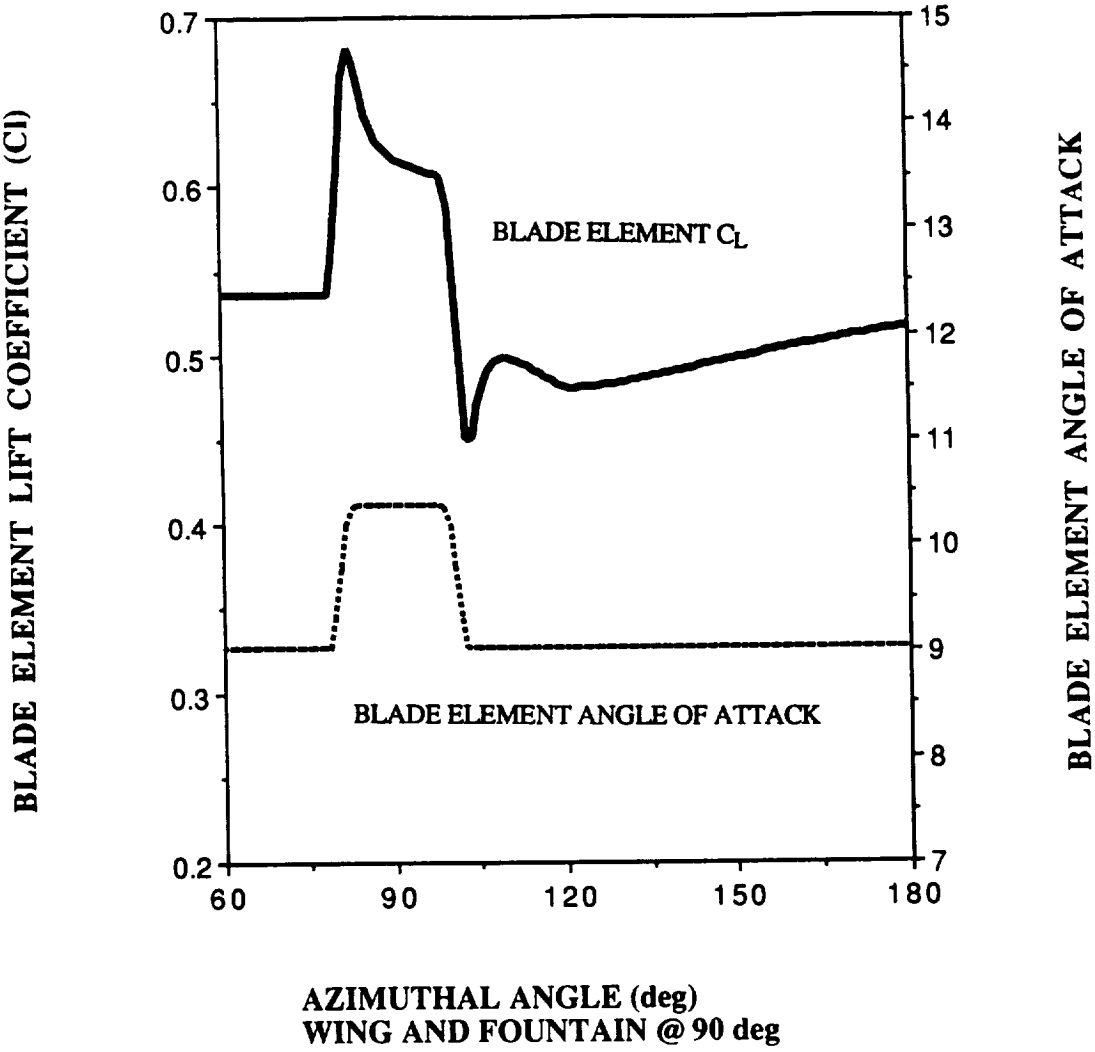

Figure 3.20 Dynamic lift response of a blade element to azimuthally varying angle of attack. 'Sharp' fountain model. M= 0.42. Fountain centered on 90 degrees.

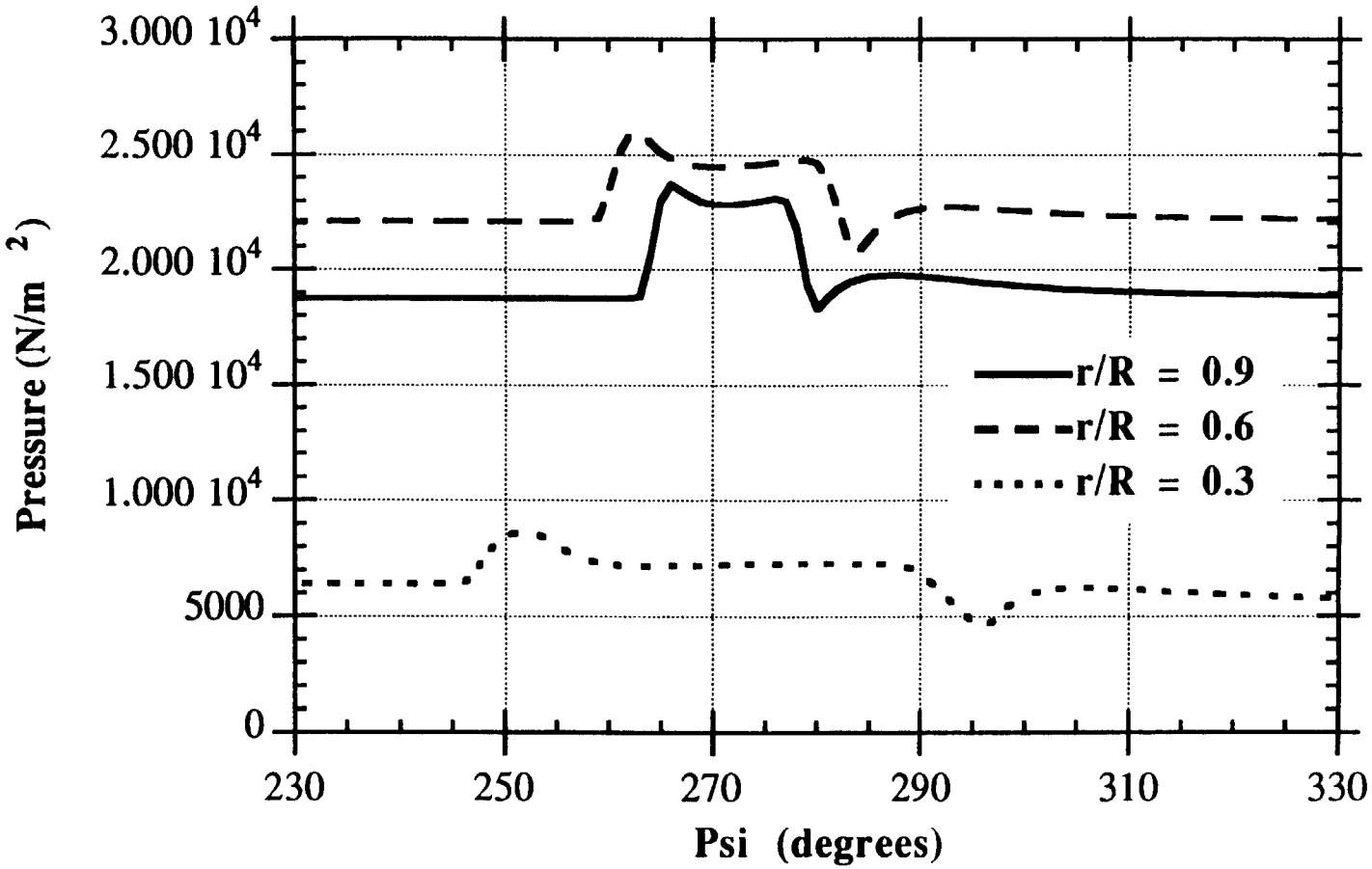

Figure 3.21 Blade element quarter chord pressure as a function of azimuth. Dynamic blade response. Fountain effect centered on Psi = 270°. Metal blade geometry.

at the entrance and exit of the fountain region. Within the fountain, the lift never assumes the steady state value, showing the dominance of the indicial response. The circulatory response is observed to accumulate after the blade section exits the fountain and the blade approaches the steady state lift. The acoustic waveform can be generated by examining $\frac{dP}{dt}$, shown in figure 3.22. Figure 3.23 shows a comparison to the $\frac{dP}{dt}$ for the steady response for a blade element at 90% chord. Clearly the over and undershoots result in an acoustic waveform of higher amplitude and slightly different shape.

Figure 3.24 shows WOPWOP noise predictions using the dynamic and quasi-steady lift responses for the rearward, near in-plane acoustics of the XV-15. The velocity addition model is termed quasi-steady as it assumes a steady state lift value for a given angle of attack and the angle of attack time history has no affect on the lift. As expected, the WOPWOP calculations show that the acoustic signal generated by the dynamic response model has a higher amplitude due to the indicial over and undershoots. The lack of smoothness in the acoustic signal is due to the coarse spanwise discretization, 25 spanwise segments, which is used to minimize CPU time. Figure 3.25 illustrates the effect of using 10 and 40 spanwise discretizations on the WOPWOP calculations.

Figure 3.26 shows a comparison between the dynamic lift and quasi-steady models using the smooth fountain model of appendix C. Again, the indicial response causes lift overshoots which result in acoustic waveforms of higher amplitude and similar shape. In the

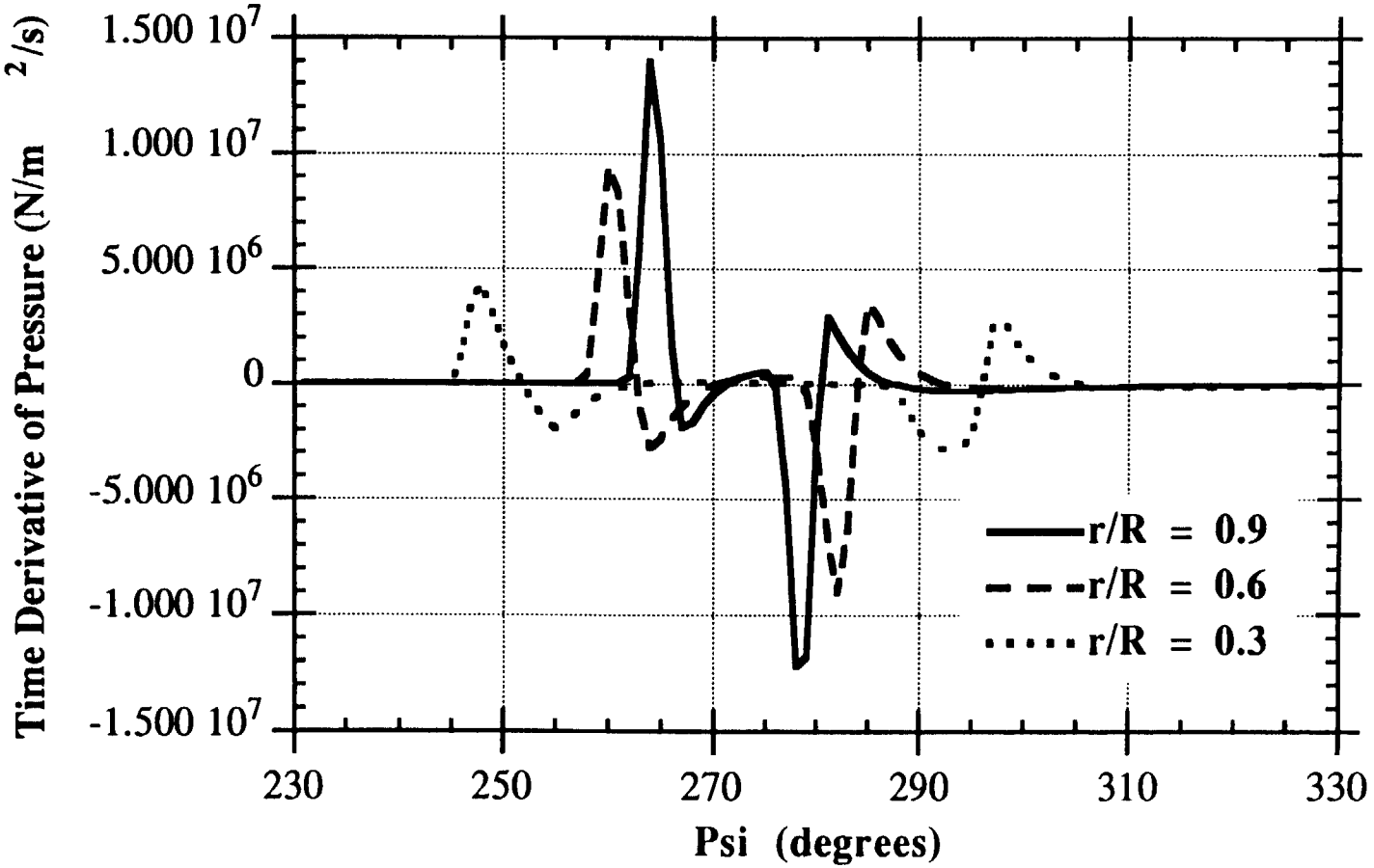

Figure 3.22 Time derivative of blade element quarter chord pressure as a function of azimuth. Dynamic blade response. Fountain effect centered on Psi = 270°. Metal blade geometry.

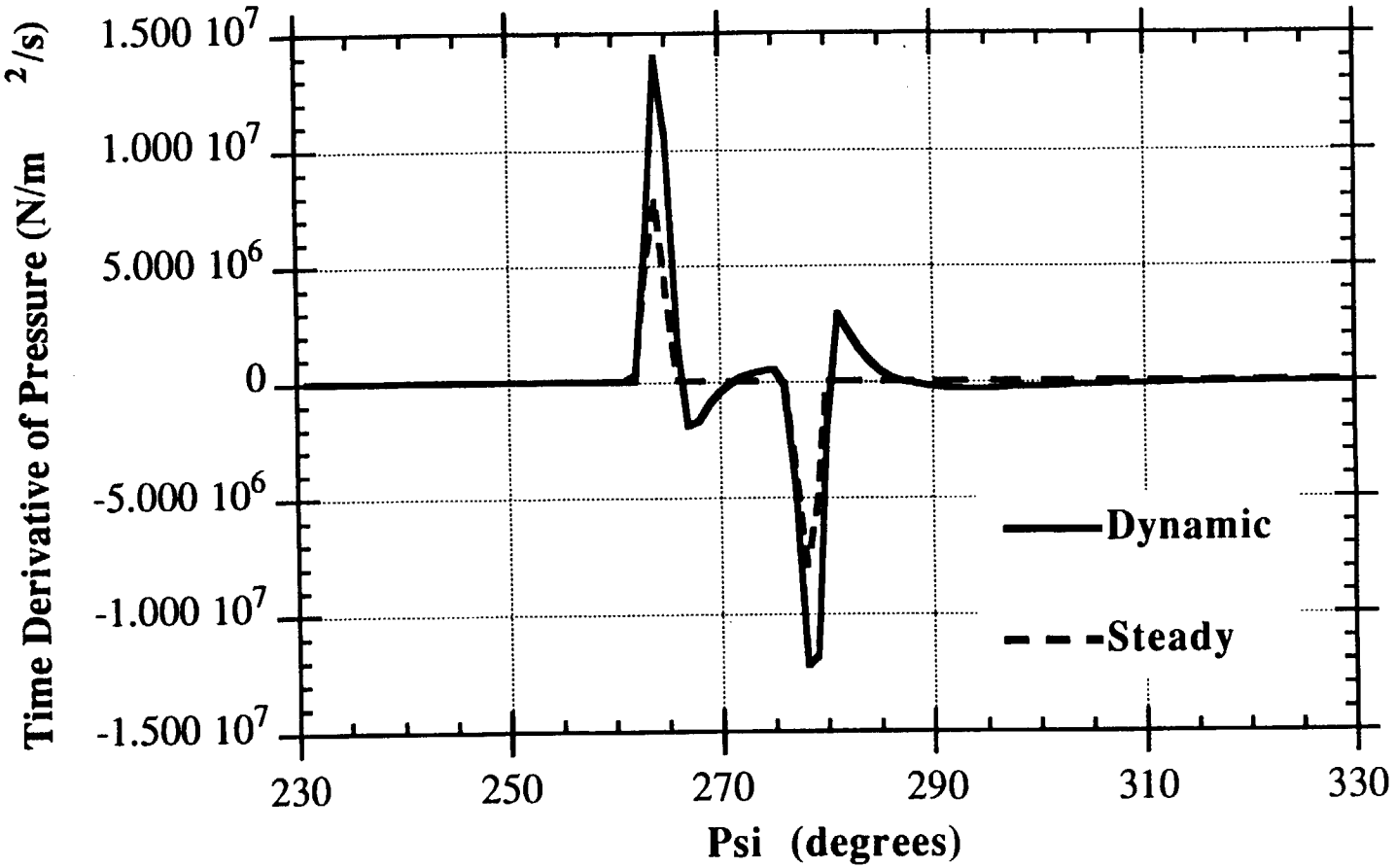

Figure 3.23 Comparison of dynamic and quasi-steady blade response. Time derivative of blade element quarter chord pressure as a function of azimuth. Fountain effect centered on Psi = 270°. r/R = 0.9. Metal blade geometry.

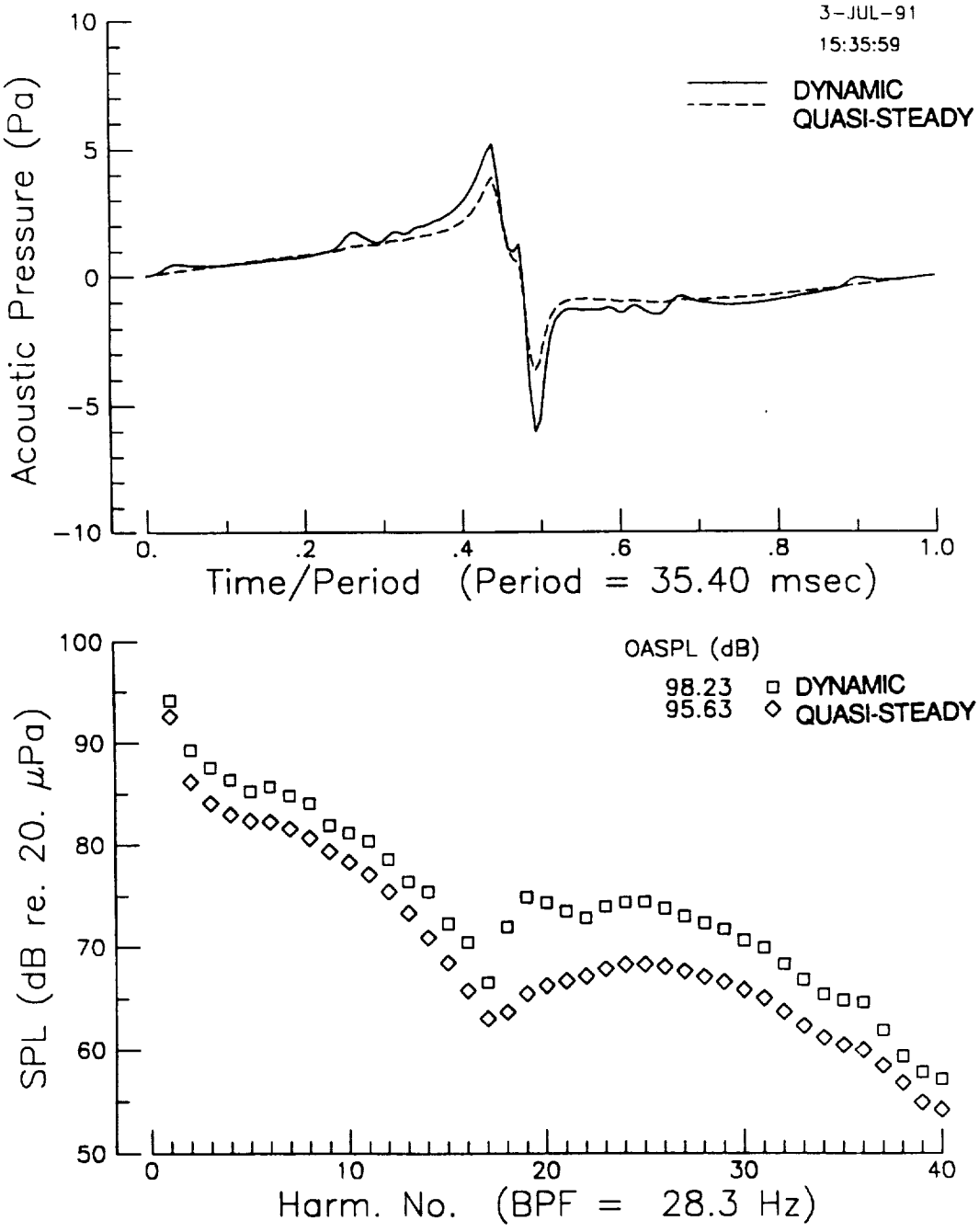

Figure 3.24 Comparison of predictions with different blade response; dynamic and quasi-steady. Loading noise. 'Sharp' fountain model. Acoustic pressure time history and sound spectrum. Near in-plane rear aircraft acoustics. Levels not corrected for comparison to experiment.

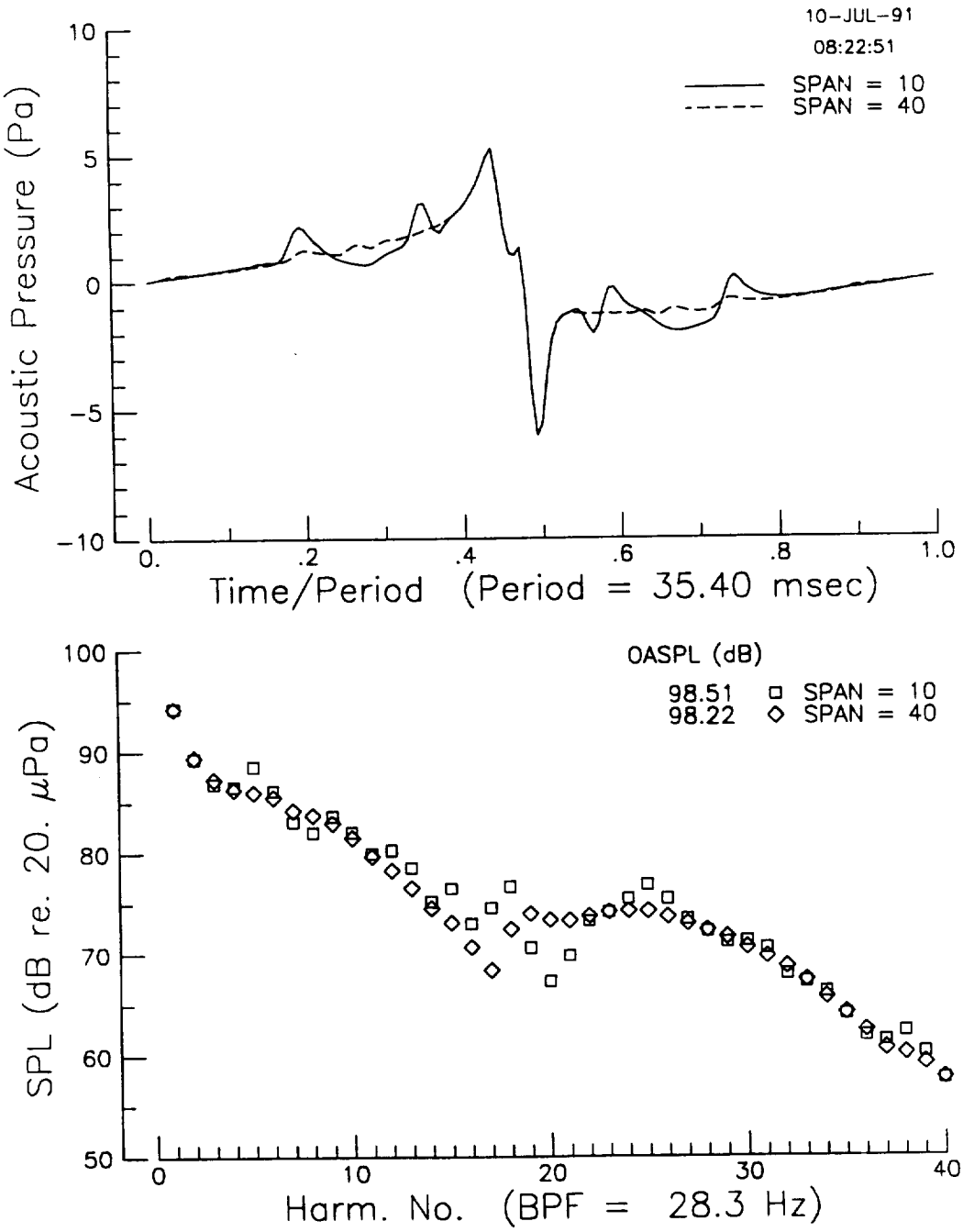

Figure 3.25 Comparison of predictions with different spanwise discretizations. Dynamic blade response. Loading noise. Acoustic pressure time history and sound spectrum. Near in-plane rear aircraft acoustics. Levels not corrected for comparison to experiment.

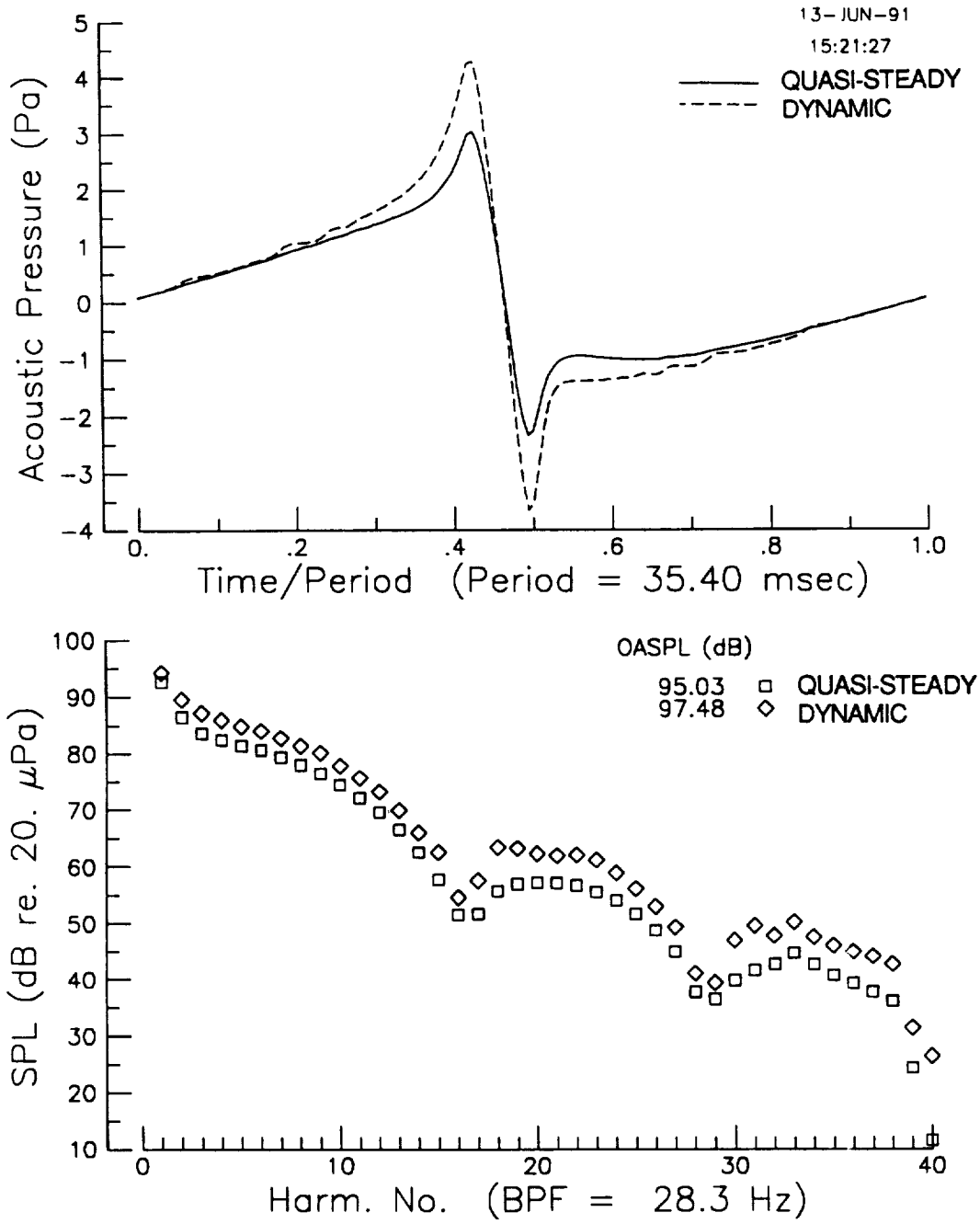

Figure 3.26 Comparison of predictions with different blade response; dynamic and quasi-steady. Loading noise. 'Smooth' fountain model. Acoustic pressure time history and sound spectrum. Near in-plane rear aircraft acoustics. Levels not corrected for comparison to experiment.

frequency domain, the dynamic lift model results in OASPL levels approximately 3 dB higher and with higher levels of high frequency content.

The implications of this study are that rotor noise predictions based on azimuthally varying rotor loads should include dynamic lift effects. Neglecting dynamic lift effects may result in under predicting the amplitude of the acoustic signal, and the higher harmonic amplitudes. This result may explain the under prediction of the fundamental harmonic in the comparisons to experiment shown in figures 3.6 and 3.7. The amplitude of the fundamental frequency is generally determined by the amplitude of the acoustic signal.

3.6 WOPWOP Noise Predictions for the XV-15 ATB Blades

WOPWOP input code was also developed to model the geometry and loading on the ATB blades described previously. These blades made use of composite materials and had different geometries and airfoil sections than the metal blades. Geometrically, the ATB blades are characterized mainly by a tapering of the chord towards the tip. A quasi-steady loading model was used with a triangular loading distribution. The sharp fountain model was used to describe the spatially varying inflow velocity.

3.6.1 Comparison of ATB and Metal Blade Acoustics

Figures 3.1 and 3.2 illustrate the geometries for the two blades. The different geometry and different loading characteristics

due to the advanced airfoil sections result in noticeably different acoustics than the metal blades. Figure 3.27 compares the thickness noise for the rearward, near in-plane acoustics for the two blades. The operational parameters are the same here as for the predictions presented in section 3.3. Figure 3.28 compares the loading noise for the two blades and figure 3.29 shows the overall noise at this observer location. These calculations are based on a single rotor calculation. The differences in acoustic signal are noticeable but not extreme. The ATB blades exhibit a 2 dB decrease in OASPL. This may be due in part to the 5% less thrust generated by the ATB blade as calculated by WOPWOP. However, this comparison does show the feasibility of modifying a rotors acoustics through selective changes in geometry and airfoil section.

3.6.2 Comparison of ATB Predictions to Experiment

The main purpose of generating input code for the ATB blades was to see if the fountain model previously defined could be used to predict both polar and azimuthal directionality and amplitude for the far field acoustics of a hovering tilt rotor. This was accomplished by comparing WOPWOP noise predictions based on the fountain model to an extensive set of aeroacoustic tests[4]. The WOPWOP comparisons made here differed from previous calculations in that the acoustic signals from the two rotors were coupled. This was done by implementing a scheme in which two WOPWOP runs were performed for each observer location. The two runs represented mirror images of observer locations about the longitudinal plane of symmetry. The pressure signals of each run

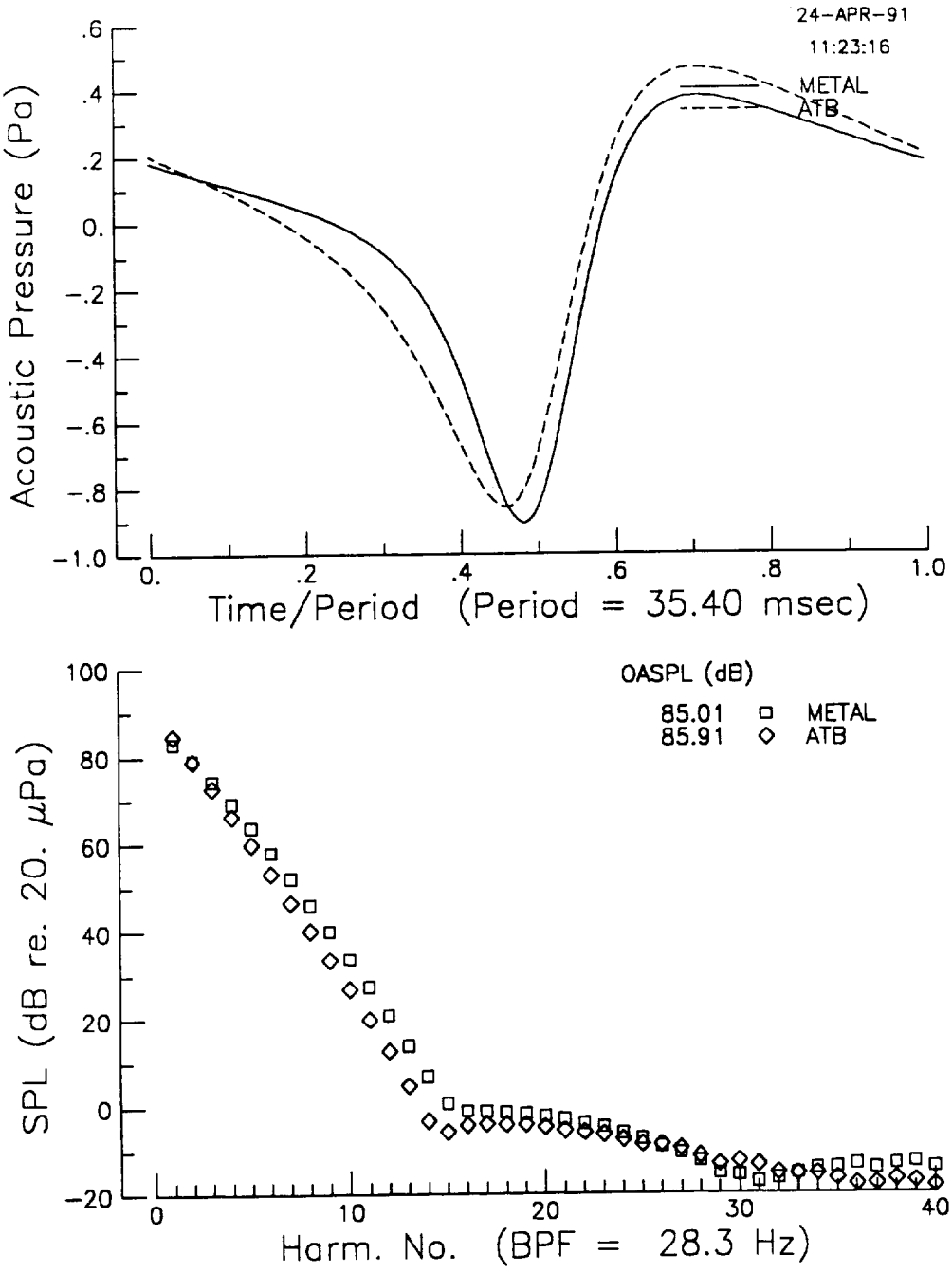

Figure 3.27 Comparison of predictions with different blade geometries; ATB and metal blades. Thickness noise. 'Sharp' fountain model. Acoustic pressure time history and sound spectrum. Near in-plane rear aircraft acoustics. Levels not corrected for comparison to experiment.

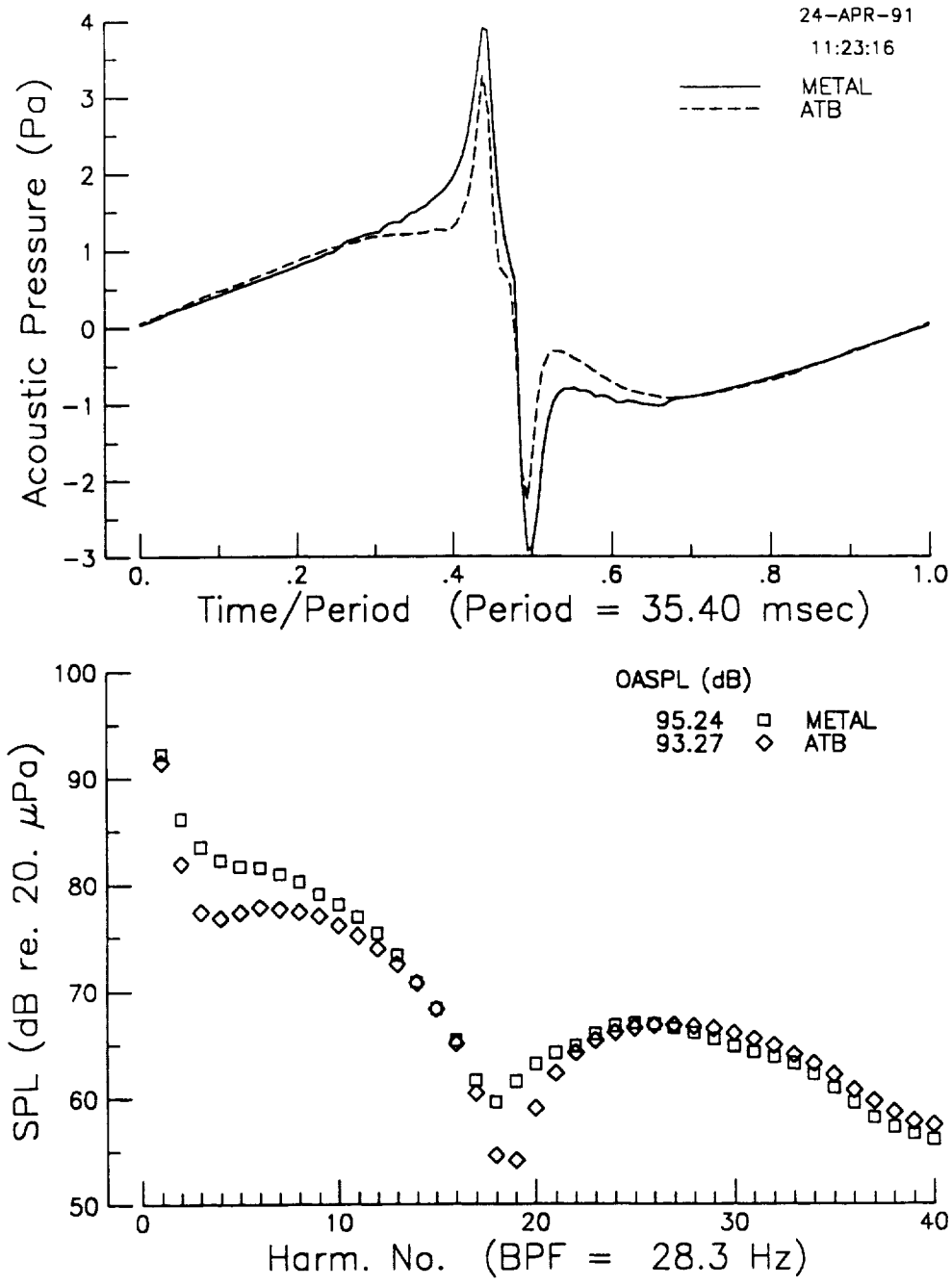

Figure 3.28 Comparison of predictions with different blade geometries; ATB and metal blades. Loading noise. 'Sharp' fountain model. Acoustic pressure time history and sound spectrum. Near in-plane rear aircraft acoustics. Levels not corrected for comparison to experiment.

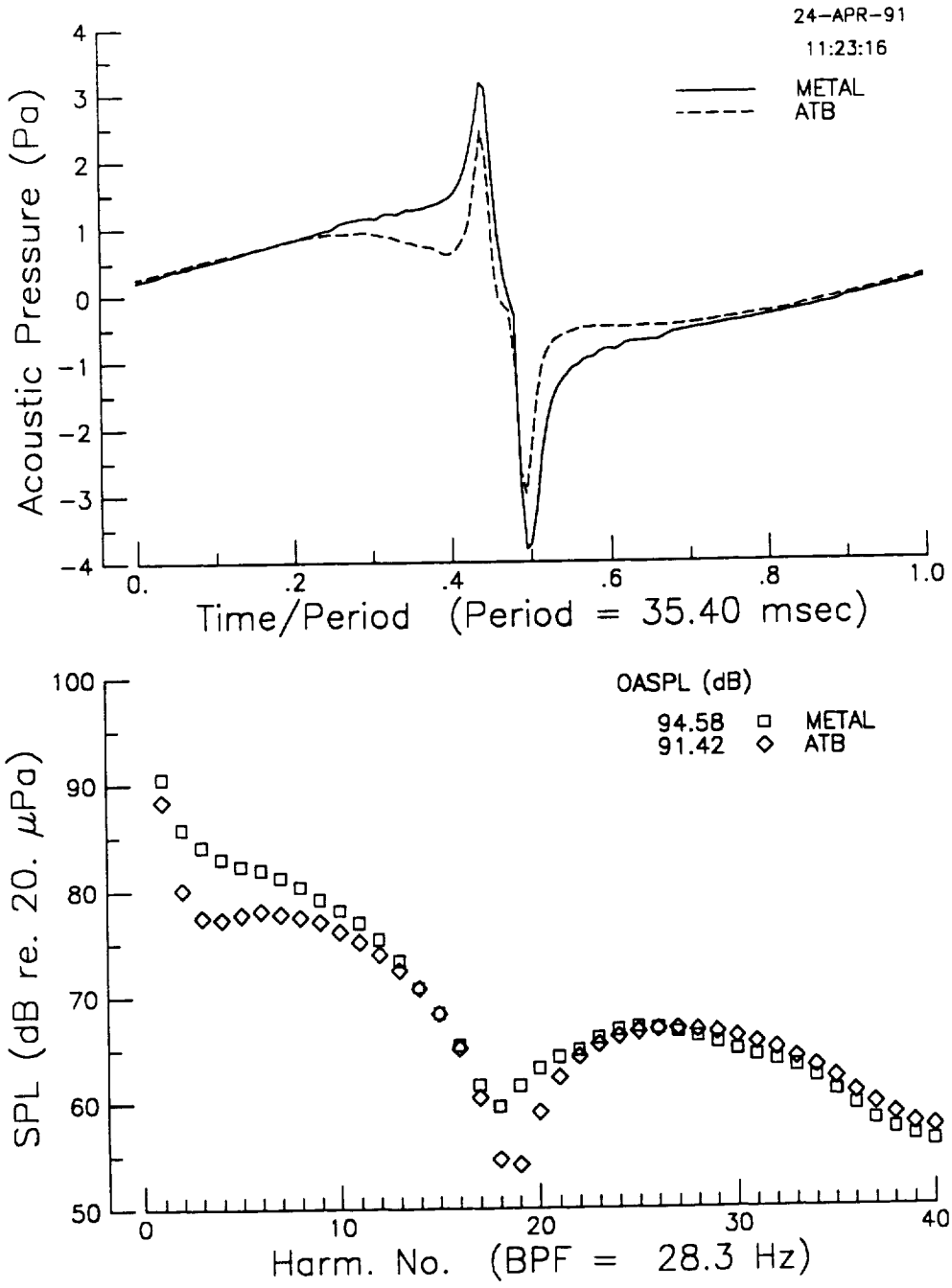

Figure 3.29 Comparison of predictions with different blade geometries; ATB and metal blades. Overall noise. 'Sharp' fountain model. Acoustic pressure time history and sound spectrum. Near in-plane rear aircraft acoustics. Levels not corrected for comparison to experiment.

were then summed to give the far field prediction. This method accounts for the interference pattern generated by two correlated acoustic sources. The summed pressures were then doubled to account for the ground plane microphones used in the experiment.

Some of the results of these predictions are shown in figures 3.30-3.33. Figure 3.30 compares the polar directivity for the forward acoustics and figure 3.31 compares the polar directivity for the rearward acoustics. Figure 3.32 compares the azimuthal directivity for an observer 45.7 degrees below the rotor plane. Figure 3.33 shows a comparison of the acoustic signal for the rear acoustics 45 degrees below the rotor plane.

An in-depth analysis of these hover acoustic tests and WOPWOP noise predictions is presented in reference 4. The conclusions of these comparisons are summarized here for completeness.

The noise mechanisms and associated directivity patterns illustrated in figures 3.30-3.33 indicate that the acoustic spikes apparent in both experimental and predicted time domain results are generated by the fountain effect. Doppler amplification, the $\frac{1}{|1-M_r|^2}$ in the far field terms of equation 3.4, causes the noise to be radiated preferentially to the rear of the aircraft. This is because the blades are moving towards the rear of the aircraft as they pass through the fountain region and are subjected to unsteady loadings. The amplitude of the acoustic signal is also greater for radiation directions out of the rotor plane as the lift dipoles radiate preferentially perpendicular to the airfoil surface which is

approximately parallel to the rotor plane. The general agreement in directivity variations and signal amplitudes support the conclusion that the fountain effect is the dominant noise mechanism for tilt rotor hover acoustics.

Differences between the predictions and experiment can also be explained. In the predictions, the positive pressure peak corresponds to a blade entering the fountain region and the negative pressure peak corresponds to the blade exiting the fountain region. In general, the predictions capture the character of the positive pressure peak as illustrated in fig 3.33. However, the negative pressure peak is generally over predicted. This implies that the physical fountain region on the XV-15 has a strongly defined entrance region which is predicted well by the fountain model. However, the irregularity of the negative pressure peak indicates that the exit region is not physically well defined and varies with time. Another consideration is that the randomly time varying exit region causes the two rotors to behave as uncorrelated acoustic sources which results in a smearing of the negative pressure peak. This random phenomenon was expected. In fact the time variations in the acoustic signal correlate qualitatively well with the time variations measured in the inflow field for the 1/12 scale model tilt rotor. Thus an important aspect of tilt rotor hover acoustics, the randomly time varying character of the acoustic signal, cannot be predicted with a deterministic mathematical model like the fountain model. One possible approach to solving this problem is to correlate acoustic and hotwire measurements over both rotors on a model tilt rotor. This would enable the

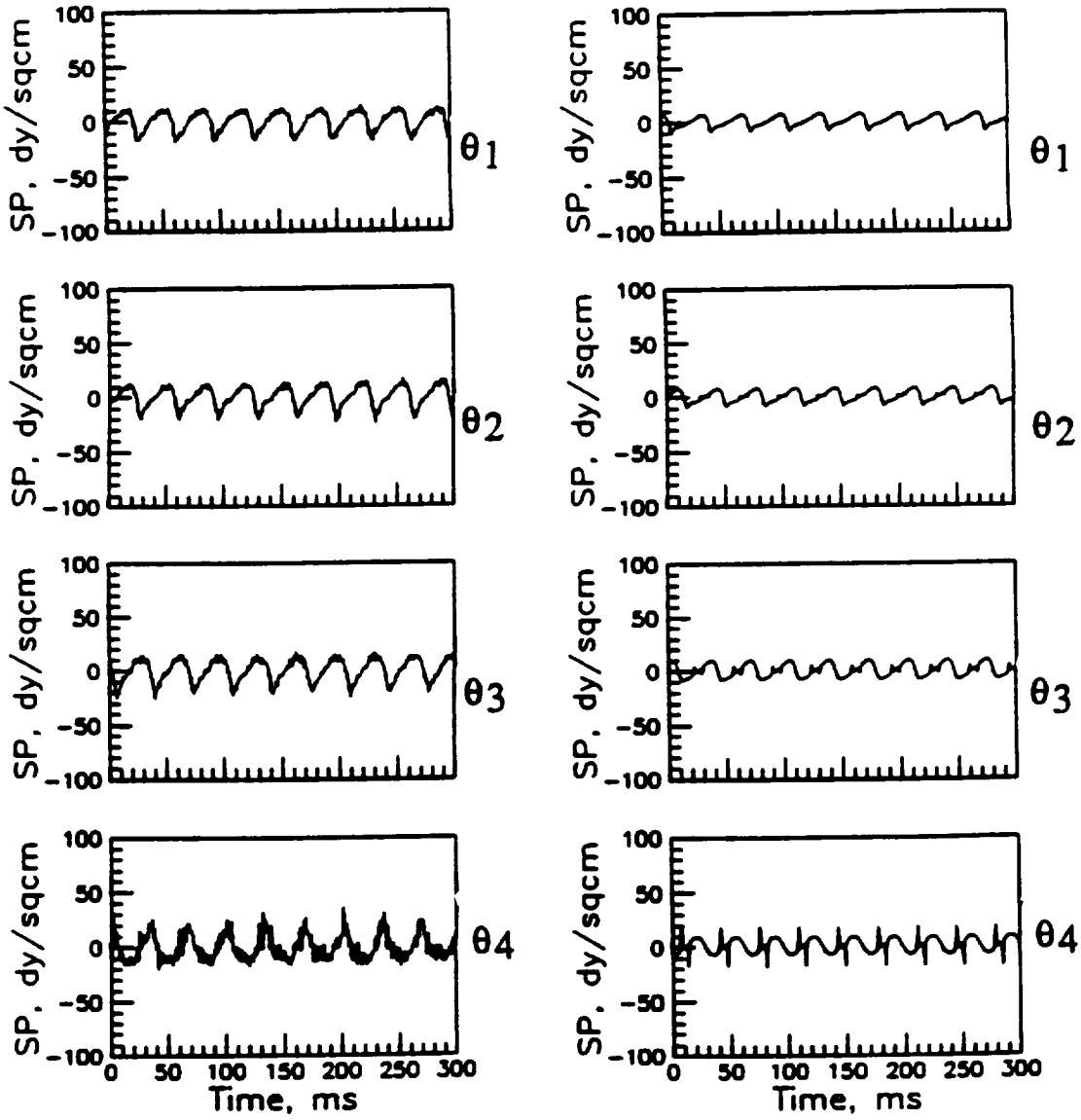

Figure 3.30 Comparison of predictions to experiment. Front aircraft acoustics for four polar angles. θ_1 = 7.2°, θ_2 = 12.7°, θ_3 = 23°, θ_4 = 45.7°. ATB geometry. Two rotor calculation, corrected for comparison to experiment. Acoustic pressure time history.

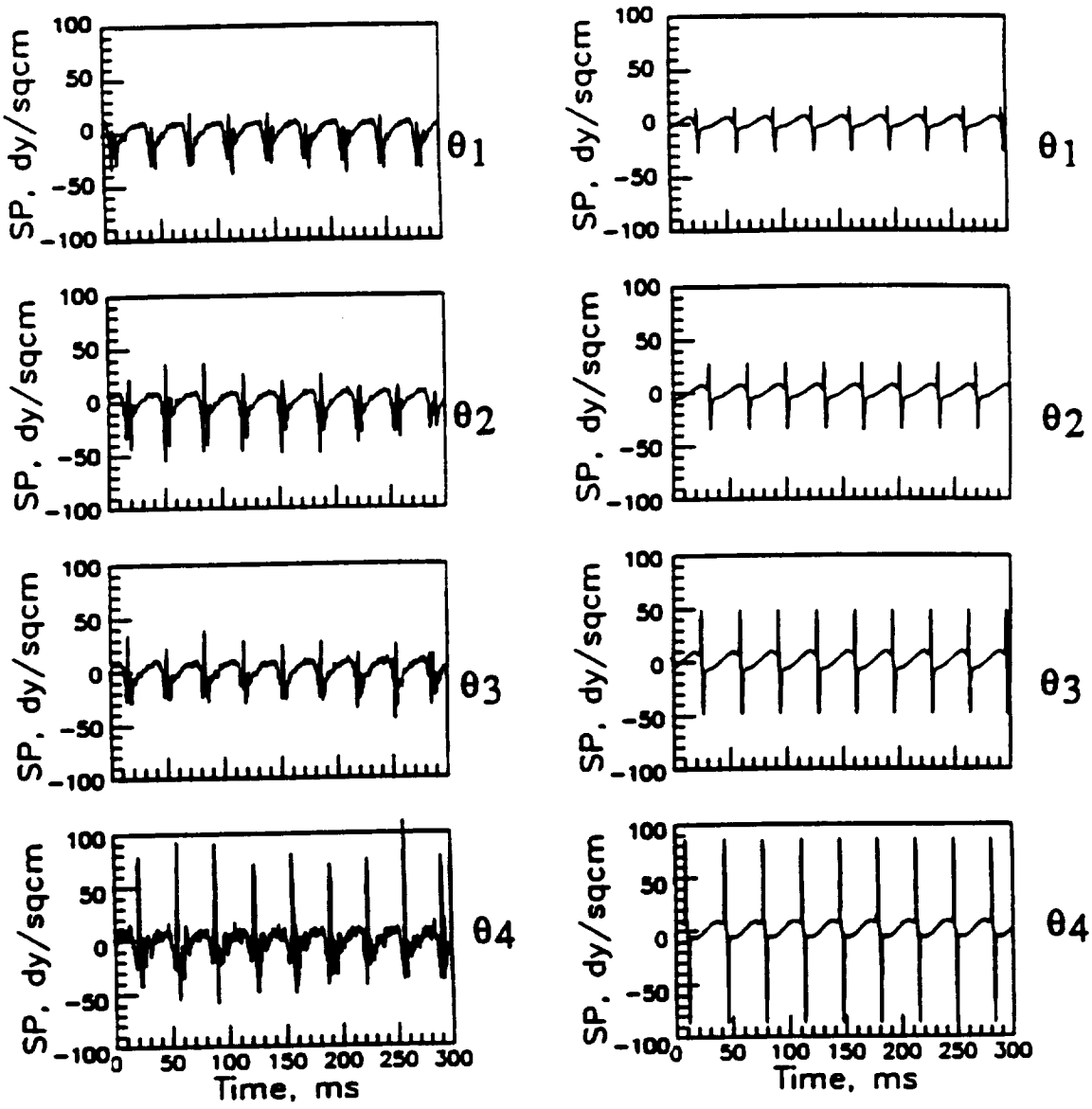

Figure 3.31 Comparison of predictions to experiment. Rear aircraft acoustics for four polar angles. $\theta_1 = 7.2°$, $\theta_2 = 12.7°$, $\theta_3 = 23°$, $\theta_4 = 45.7°$. ATB geometry. Two rotor calculation, corrected for comparison to experiment. Acoustic pressure time history.

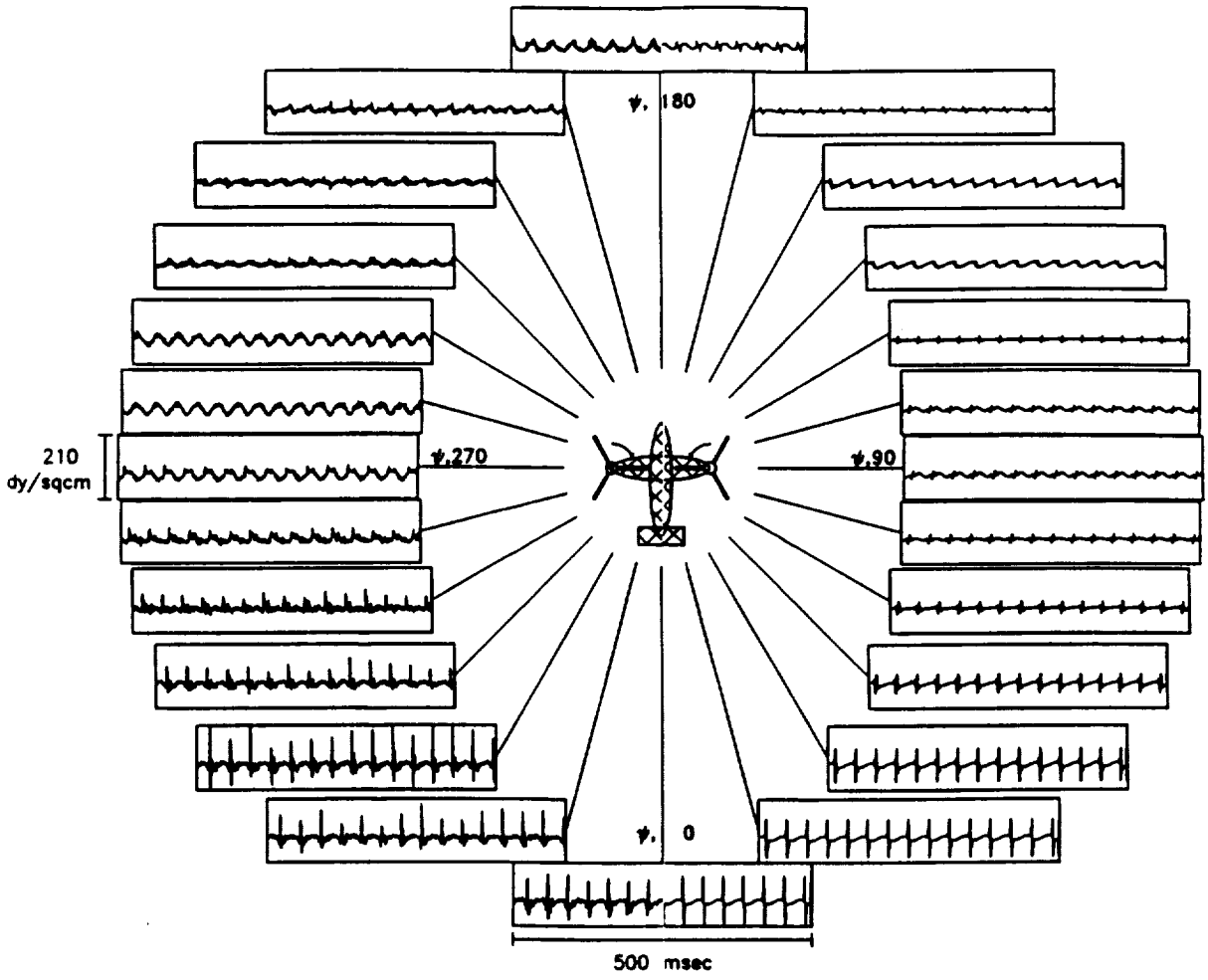

Experiment Predicted

Figure 3.32 Comparison of predictions to experiment. $\theta = 45.7°$. Thirteen front to rear azimuthal angles. ATB geometry. Two rotor calculation, corrected for comparison to experiment. Acoustic pressure time history.

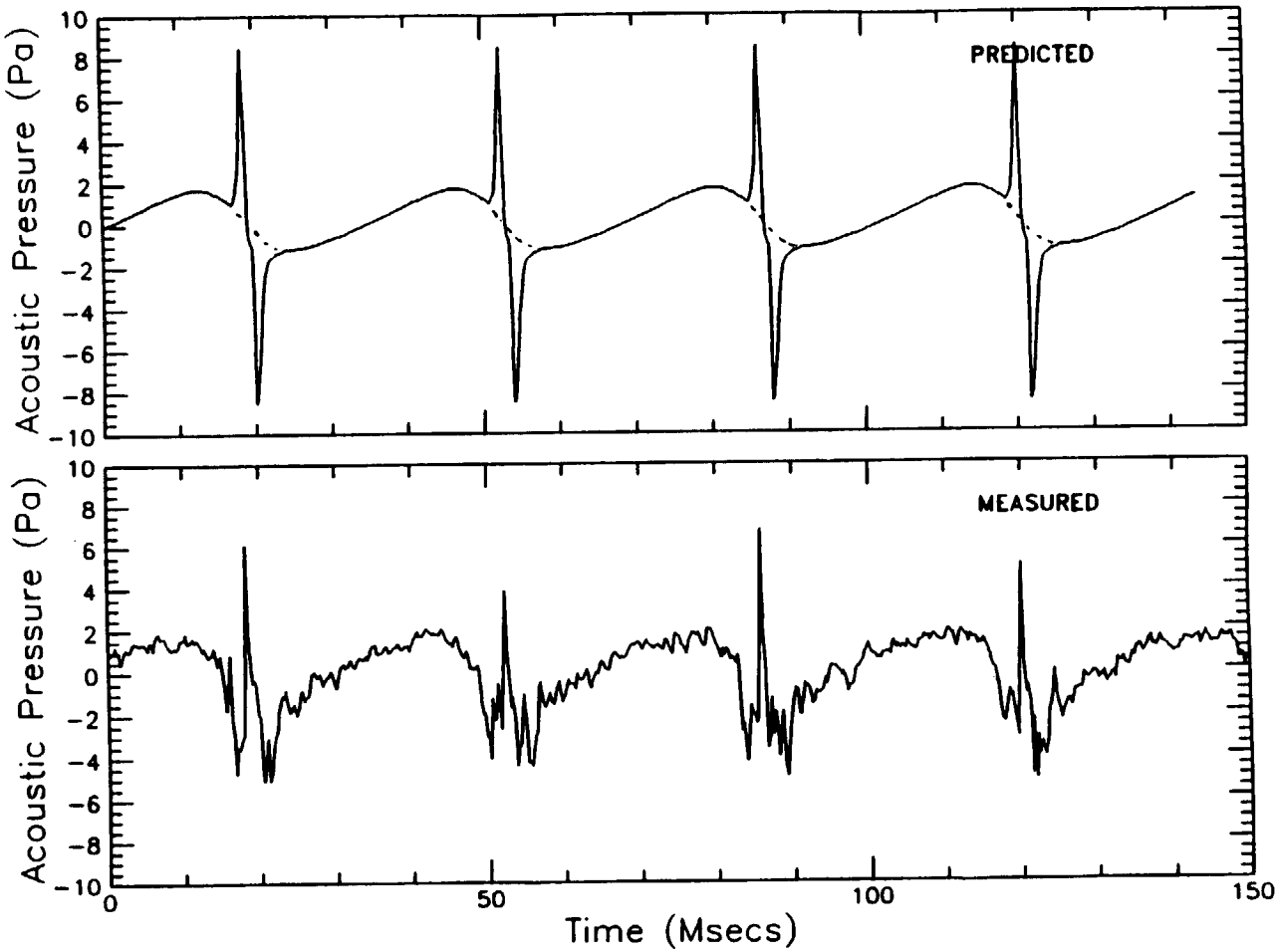

Figure 3.33 Comparison of prediction to experiment. $\theta = 45.7°$. $\psi = 0°$. ATB geometry. Two rotor calculation, corrected for comparison to experiment. Acoustic pressure time history. Dashed lines indicate prediction without fountain effect.

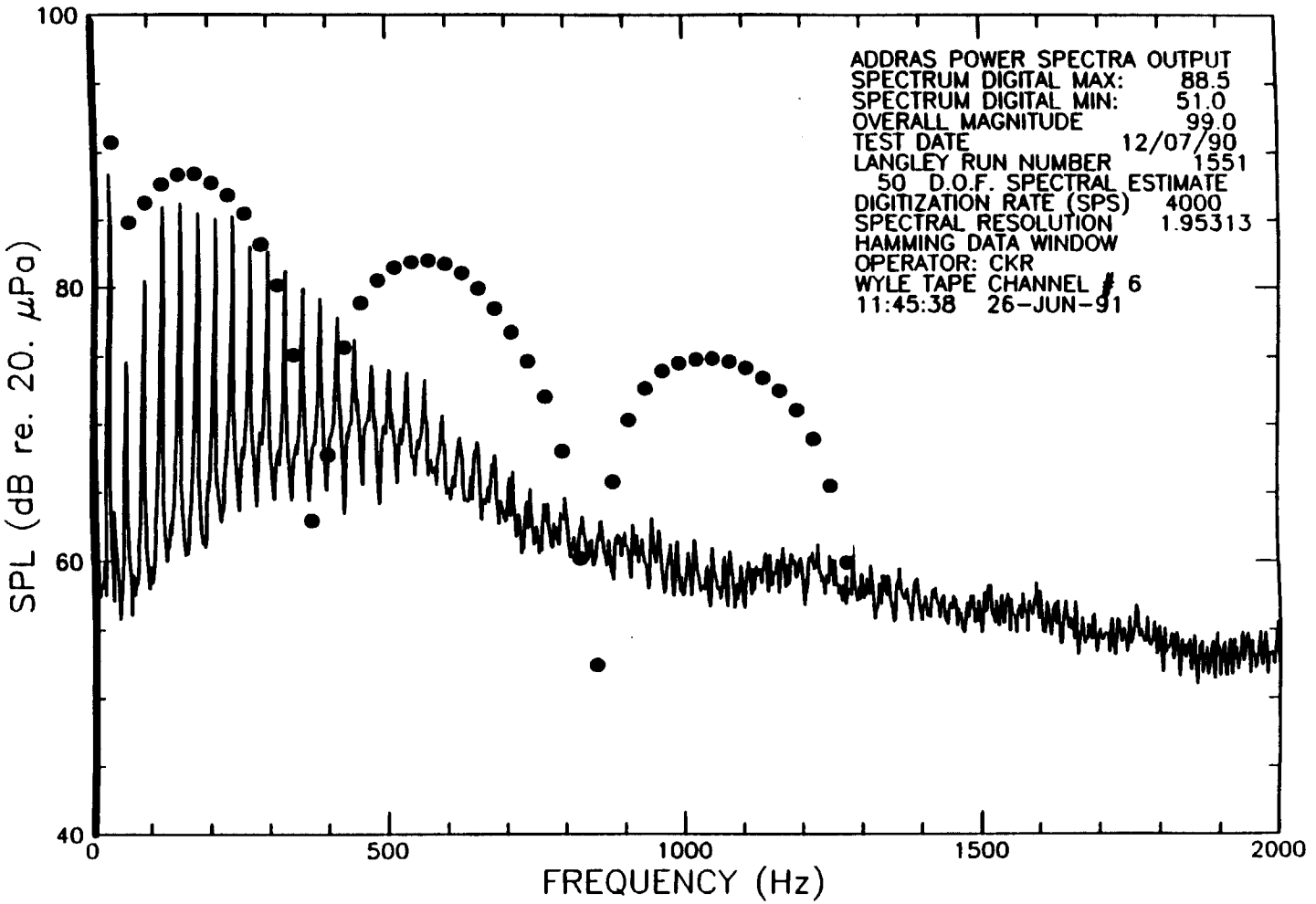

Figure 3.34 Comparison of prediction to experiment. $\theta = 45.7°$. $\psi = 0°$. ATB geometry. Two rotor calculation, corrected for comparison to experiment. Sound spectrum.

development of a fountain model based on correlation results instead of assuming a correlation of 1 or 0 between the acoustic sources.

This effect shows up more clearly in a comparison of measured and predicted spectra. Figure 3.34 shows a comparison of spectra for an observer location behind the aircraft and 45.7 degrees below the rotor plane. The predicted spectra are based on a non-variable single blade passage calculation and show the harmonic scalloping discussed in section 3.4. The experiment does not exhibit this characteristic as the experimental spectrum contains 50 averages of spectra calculated from 1 second time intervals each of which contains approximately 30 blade passages.

Chapter IV

Broadband Noise Predictions Using Modified Amiet Method

Previously, no methods were available for predicting rotor broadband noise with azimuthally varying inflow turbulence. This chapter describes a method for adapting the method of Amiet[27,28,29] to account for azimuthally and radially varying turbulence and presents broadband noise predictions for a hovering tilt rotor based on this scheme.

4.1 Broadband Acoustic Formulation

As was alluded to in Chapter II, broadband noise cannot be calculated explicitly from the Ffowcs Williams Hawkings Equation. This is because the loading fluctuations are due to turbulent fluctuations in the inflow field and are therefore non-deterministic. The most widely used approach is to solve for the acoustic far field noise spectrum. This can be done by solving in the frequency domain rather than the time domain. Reference 30 contains a more extensive treatment of general broadband rotor noise concepts.

The radiative terms of loading noise can be extracted from equation 3.4:

$$4\pi p_L'(\underline{x},t) = \frac{1}{c_0}\int_{f=0}\left[\frac{\dot{l}_i\hat{r}_i}{r(1-M_r)^2}\right]dS(\eta) + \frac{1}{c_0}\int_{f=0}\left[\frac{l_r(\dot{M}_i\hat{r}_i)}{r(1-M_r)^3}\right]dS(\eta) \tag{4.1}$$

If one assumes that the surface force distribution can be replaced by a point source, then in an analogous way to equation 4.1 the far field sound due to a moving point force can be written as[31]:

$$4\pi p_L'(\underline{x},t) = \left[\frac{\hat{r}_i}{c_0 \, r^2 (1-M_r)^2} \left(\frac{\partial F_i}{\partial t} + \frac{F_i}{1-M_r} \frac{\partial M_r}{\partial t} \right) \right] \qquad (4.2)$$

The acoustic pressure can be written in spectral form as the generalized Fourier transform of the time domain solution:

$$p_L'(\underline{x},f) = \int_{-\infty}^{\infty} p_L'(\underline{x},t) \, e^{-2\pi i f t} \, dt \qquad (4.3)$$

How this integral is to be evaluated for a rotor whose fluctuating loads are caused by inflow turbulence has been the subject of several previous studies.[27,28,29,30,32,33]

4.2 Comparison of 3 Broadband Rotor Noise Prediction Schemes

Amiet's method is of primary relevance here as his algorithm can be easily modified to account for azimuthally varying inflow properties. A brief description and comparison of other existing methods is provided for historical context and completeness.

4.2.1 Method of Homicz and George[32]

This method treats the general case of unsteady forces distributed in space following the Lighthill Equation[34]. Each blade is

represented by a point acoustic dipole at some radius, R_0. The analysis is carried out in observer fixed coordinates which rigorously accounts for blade to blade correlations. This approach can be viewed as calculating the sound field generated by unsteady forces distributed in space. The acoustic dipoles related to these unsteady force switch on and off as the blade rotates over the dipole location in space.

4.2.2 Method of George and Kim[33]

This method approximates the distributed unsteady blade forces as moving point forces. The calculation method takes advantage of the high frequency characteristics of the load fluctuations to reduce computational complexity. The smooth high frequency part of the spectrum is primarily generated by uncorrelated blade loadings which allows direct summation of the acoustic intensities of each blade. This method also accounts for Doppler shifts in the radiation frequency due to the moving point force.

4.2.3 Method of Amiet[27,28,29]

This method takes a different approach by approximating the circular motion of the rotor blade as a series of rectilinear motions. The noise spectrum can be obtained by summing and averaging the noise spectrum of a number of individual linear blade motions over one revolution. This method has the advantages of accounting for a full range of wavelength-to-chord ratios and has accurate directivity predictions. This method can also be applied to noise

calculations for a rotor in forward flight and can account for turbulence contraction effects. Most importantly in the present study, this method is easily adapted to account for azimuthally varying inflow turbulence.

4.2.4 Comparison of Broadband Noise Prediction Schemes

As the above three broadband noise prediction schemes use different assumptions and computational schemes, a set of operating conditions was selected to compare the results of the three methods. The operational parameters of the Johnson and Katz experiment[35] was used as predictions for this case have previously been published for the three methods. Previously, Amiet compared the results of his method to the method of Homicz and George. This comparison showed good agreement. However, the method of Amiet assumed a Von Karman spectrum of turbulence while the method of Homicz and George assumed a Dryden spectrum of turbulence. Figure 4.1 shows calculations for the three methods all of which use the Von Karman turbulence spectrum in the calculation. The methods of George and Kim and Amiet, both of which use 20 spanwise segments, show good agreement, especially at high frequencies. where the assumptions made in both of these schemes are valid. The predictions based on the method of Homicz and George, which approximates the blade as a single element at 80% radius, are consistently higher than the other two methods by approximately 15 dB.

Figure 4.2 shows a similar calculation using the Dryden turbulence spectrum. In this figure, the method of Kim and George

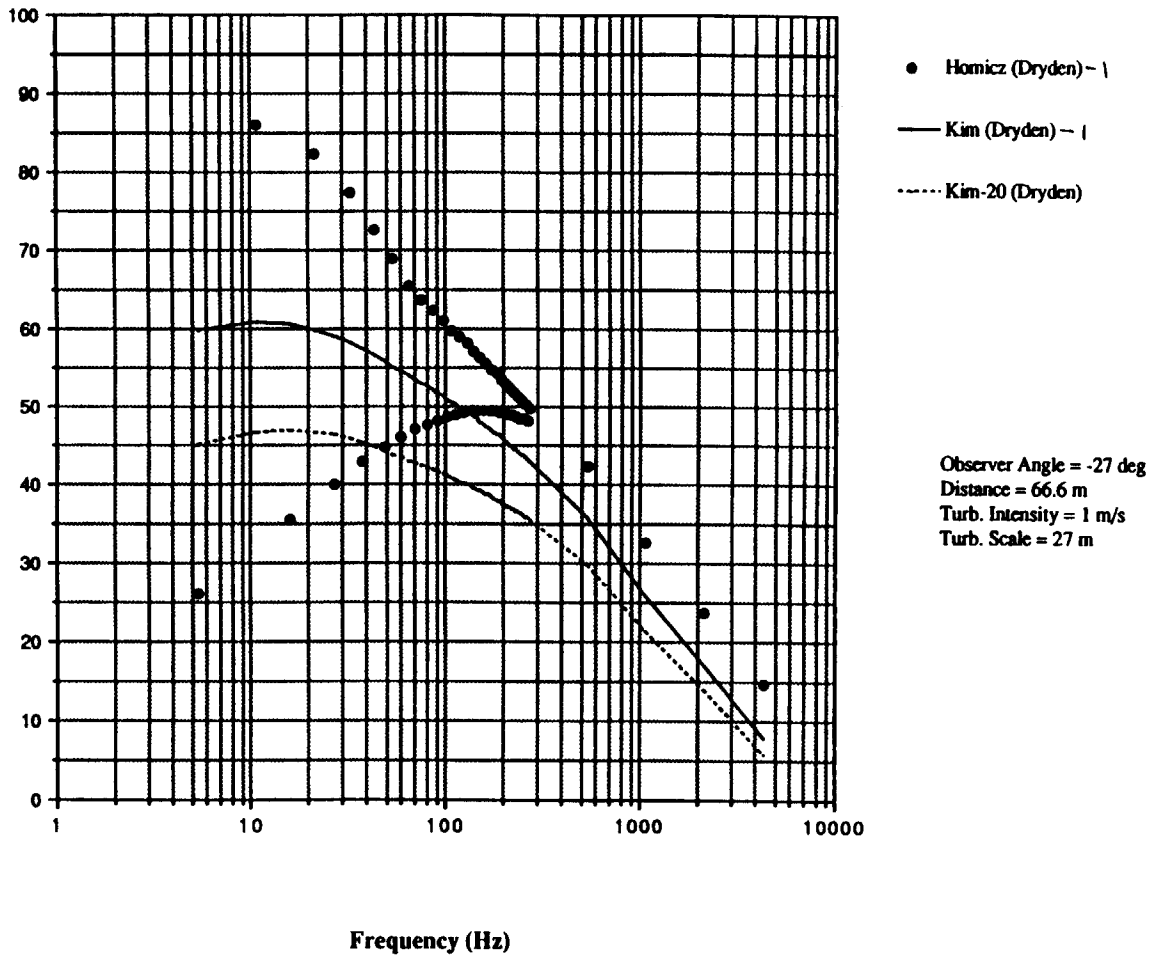

Figure 4.1 Comparison of broadband noise prediction methods. Von Karman turbulence spectrum. Amiet (20 spanwise segments), Kim and George (20 spanwise segments), and Homicz and George (1 spanwise segment).

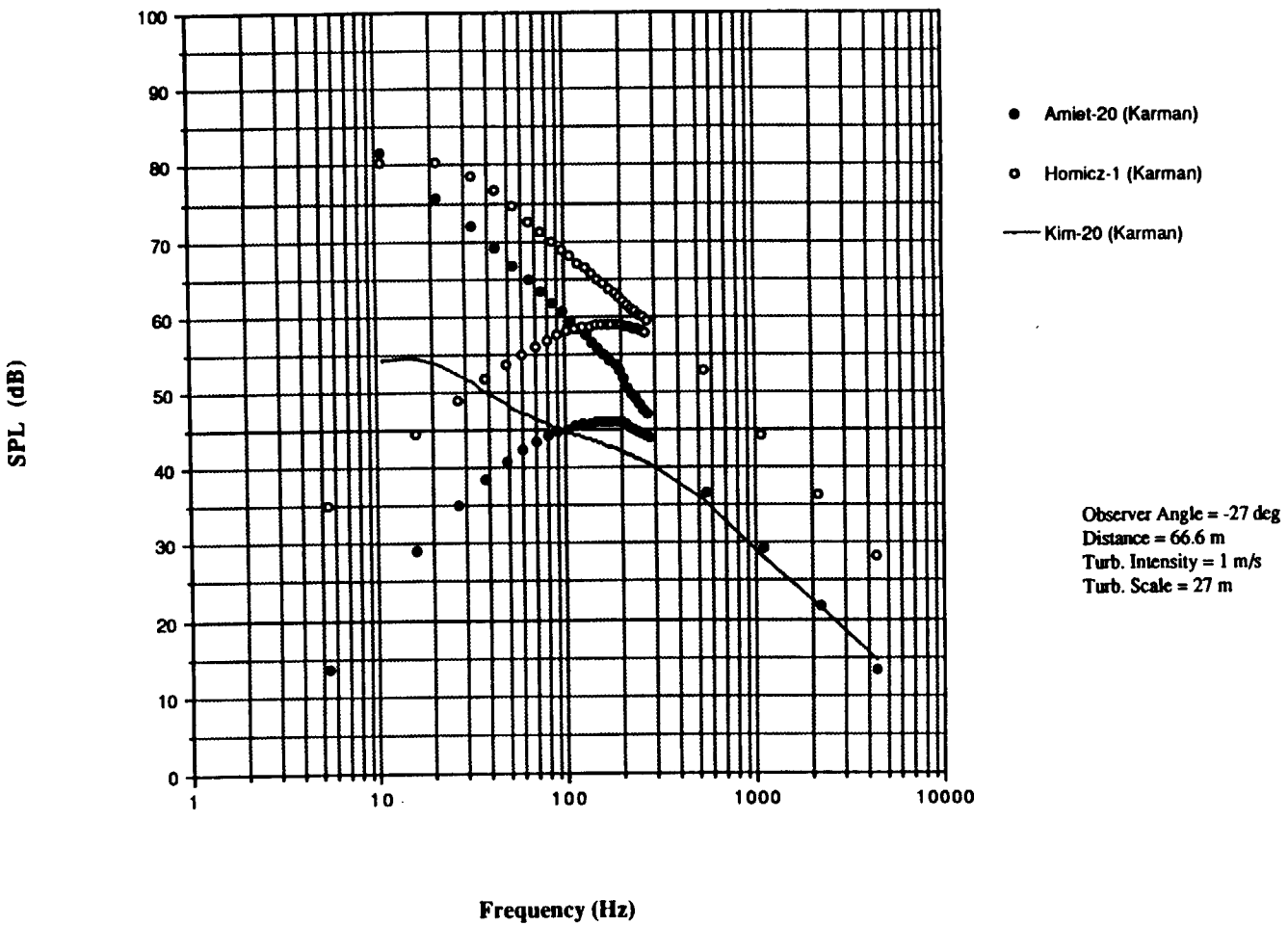

Figure 4.2 Comparison of broadband noise prediction methods. Dryden turbulence spectrum. Kim and George (20 spanwise segments), Kim and George (1 spanwise segments), and Homicz and George (1 spanwise segment).

is compared to the method of Homicz and George. Amiet's method is not compared as the code could not be easily modified to use the Dryden spectrum. Two predictions are shown for the method of George and Kim; the solid line curve approximates the rotor blade as a single element at 80% radius and the hashed line approximates the rotor blade using 20 radial segments. As noted previously, the method of Homicz and George approximates the rotor blades as a single element at 80% radius. Figures 4.1 and 4.2 indicate that approximating the rotor blade as a single element at 80% radius leads to overpredictions of the sound pressure levels. Figure 4.2 also indicates that the method of Homicz and George does not agree well with the method of George and Kim. The two single element calculations disagree by ~7 dB at all frequencies. Comparisons of this nature have not been made previously as the method of Homicz and George had been previously computationally impractical for high frequencies and the method of George and Kim is not accurate at low frequencies. The method of Homicz and George should be reformulated in terms of multiple spanwise segments in order to be compared further with the other two formulations. The good agreement between the method of George and Kim and the method Amiet indicates that both are accurate formulations and are coded correctly.

4.3 Modified Method of Amiet

The basic method of Amiet calculates the noise produced by an airfoil as it moves rectilinearly through turbulence. The actual circular blade motion of a rotor blade is then approximated by a

series of straight line segments. The analysis can also include rapid distortion theory (the effect of distortion on turbulence as it moves onto the rotor), and some blade-to-blade correlation due to multiple eddy chopping. In this study, the method of Amiet was modified to account for azimuthal variations of the turbulence characteristics as the blade rotates through the fountain reingestion zone. These modifications are described in Appendix D. The azimuthally varying turbulence was defined in such a way as to approximate the measured spatial variations in rms inflow velocity shown in figure 2.22.

The calculations require the blade planform geometry and motion, mean inflow velocity, and local values of the inflow rms turbulent velocity and integral scale. The turbulence properties were scaled from the 1/12 scale model experiments. The principles behind the scaling method are described in Appendix E. For the calculations, the reingestion zone rms velocity is 4.71 m/s, the convection velocity is 22.36 m/s, and the integral scale is 0.356 m. Over the rest of the disk, the rms velocity is 1 m/s, the convection velocity is 22.36 m/s and the integral scale is 90% of the hover altitude.

The method of Amiet is set up for calculations using the Von Karman turbulence spectrum. This assumption was evaluated by comparing the Von Karman longitudinal spectrum with the measured longitudinal spectrum for the 1/12 scale model tilt rotor. The comparison is shown in figure 4.3 and the principles behind reducing the experimental data and generating the longitudinal spectrum from the energy spectrum are given in Appendix F.

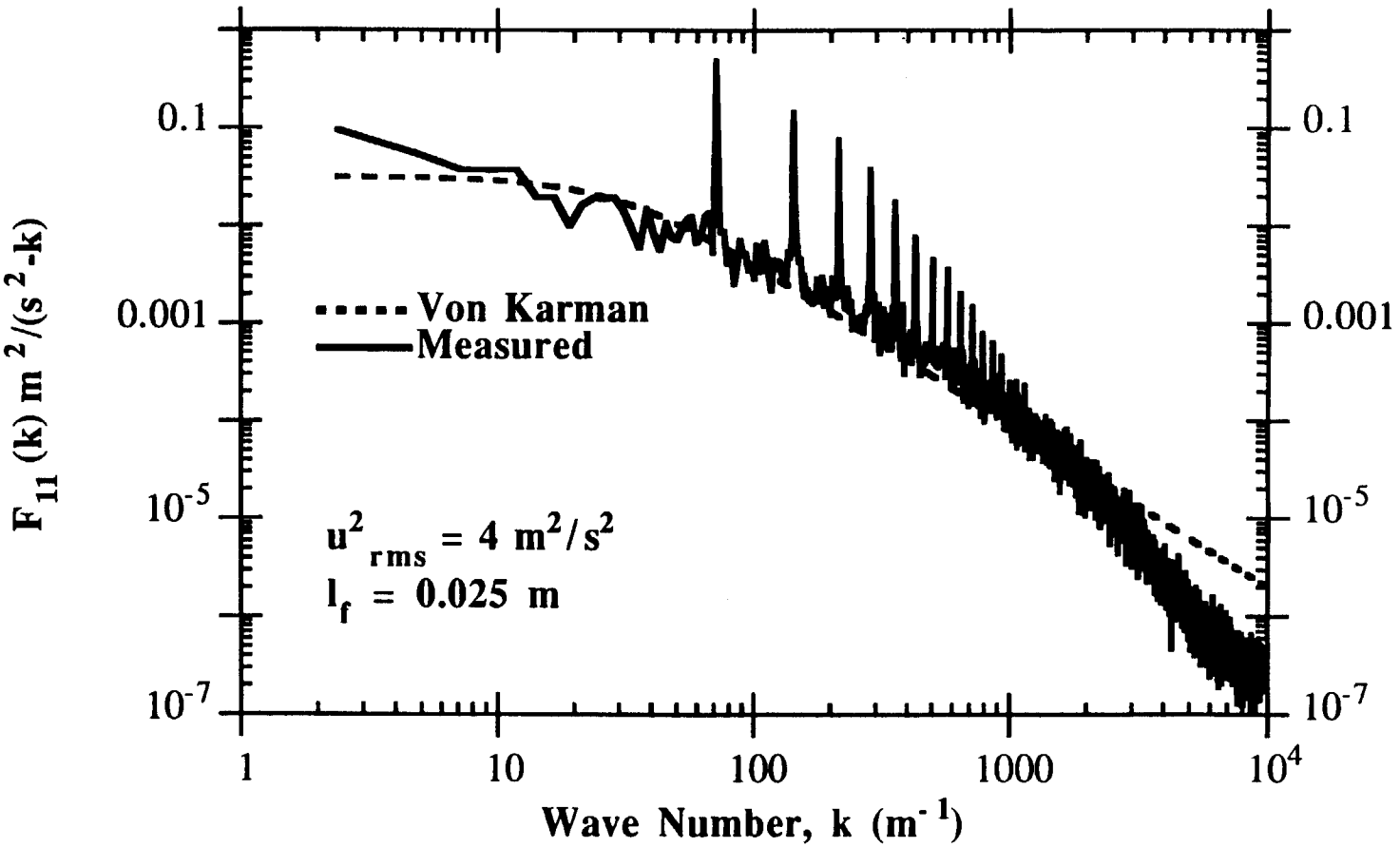

Figure 4.3 Comparison of Longitudinal Spectra, $F_{11}(k)$. Von Karman vs. Measured.

Figure 4.3 shows reasonable agreement for wave numbers less than 3000 m^{-1}. At higher wave numbers the experimental data shows significantly less energy than the Von Karman spectrum used in the predictions. This should result in overpredictions of the sound pressure levels at higher frequencies. The apparent inconsistency between the Von Karman spectra and the experimental longitudinal spectrum is that while the Von Karman spectrum falls off as $k^{-5/3}$, the experimental longitudinal spectrum falls off much more rapidly at high wave numbers. This is probably due to the viscous effects at the smaller scales of the model test.

4.4 Comparison of Modified Method of Amiet to Experiment

The modified method of Amiet was used to predict the sound pressure levels for three azimuthal observer locations at each of four polar observer angles. For the polar angles of 7.2°, 12.7°, 23.1°, and 45.7° the front, rear, and side acoustics were calculated. The rear acoustic predictions are compared to the NASA full scale, tilt rotor hover experiments in figures 4.4a-d. Figures 4.5-4.8 show the predictions and experimental results for the front, rear, and side acoustics at each of the four hover heights. The .p designation indicates the plot shows the predicted sound spectrum and the .e indicates that the plot shows the experimental sound spectrum.

The predictions are quite promising as they indicate that the sound polar and azimuthal directionality trends are captured. The predicted sound levels are reasonable and are generally within a few dB of the experiment with the exception of the high frequency range of the 23.1° polar angle. With one exception, the predictions

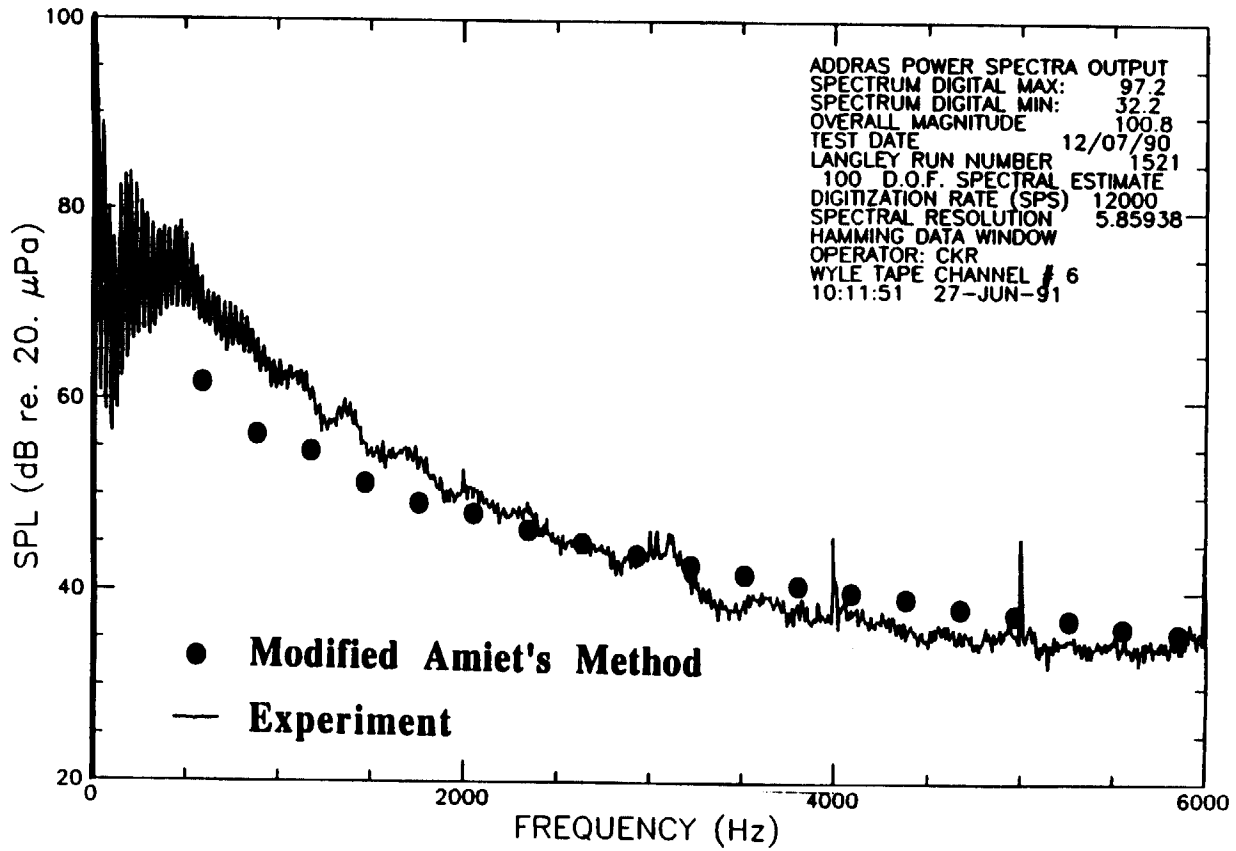

Figure 4.4a Comparison of experimental and predicted broadband noise spectra. Rear aircraft acoustics, θ = 7.2°. Langley/Ames XV-15 ATB hover test.

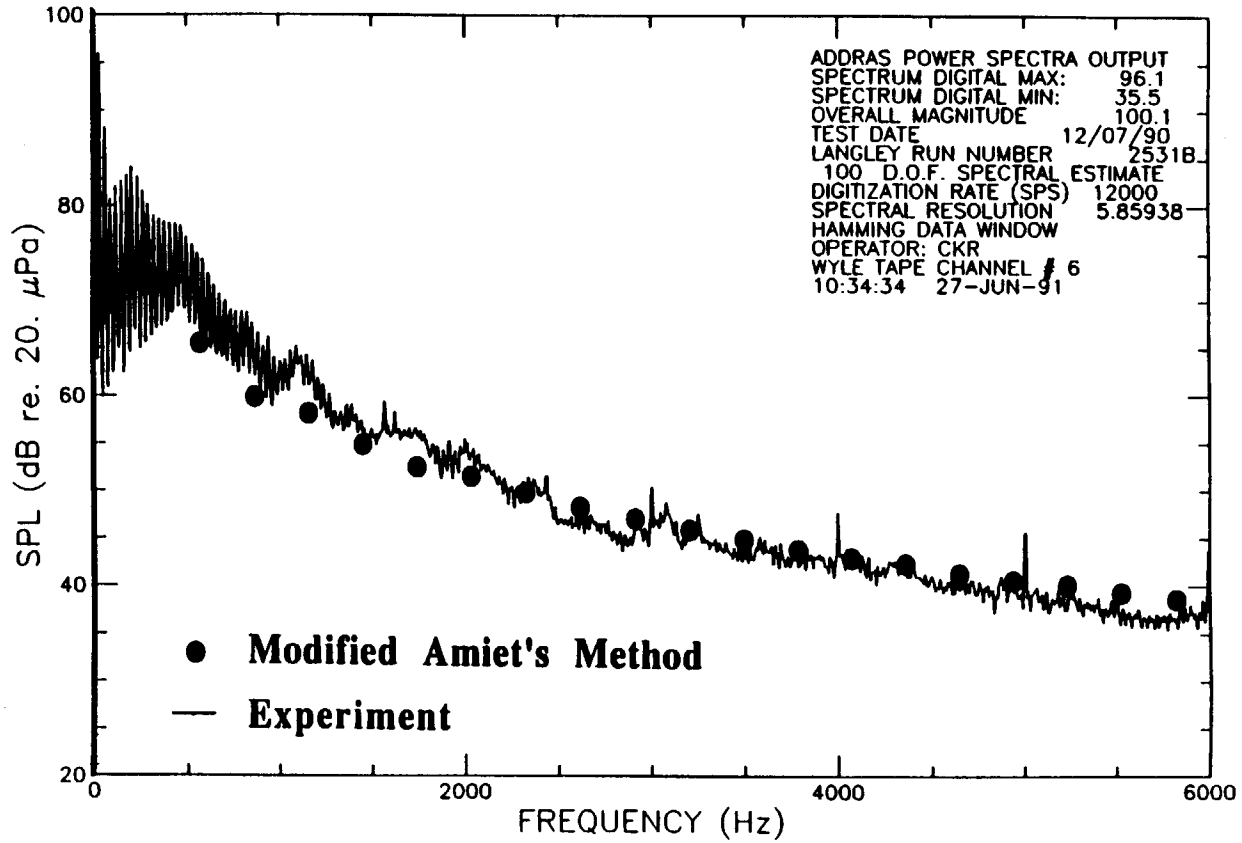

Figure 4.4b Comparison of experimental and predicted broadband noise spectra. Rear aircraft acoustics, θ = 12.7°. Langley/Ames XV-15 ATB hover test.

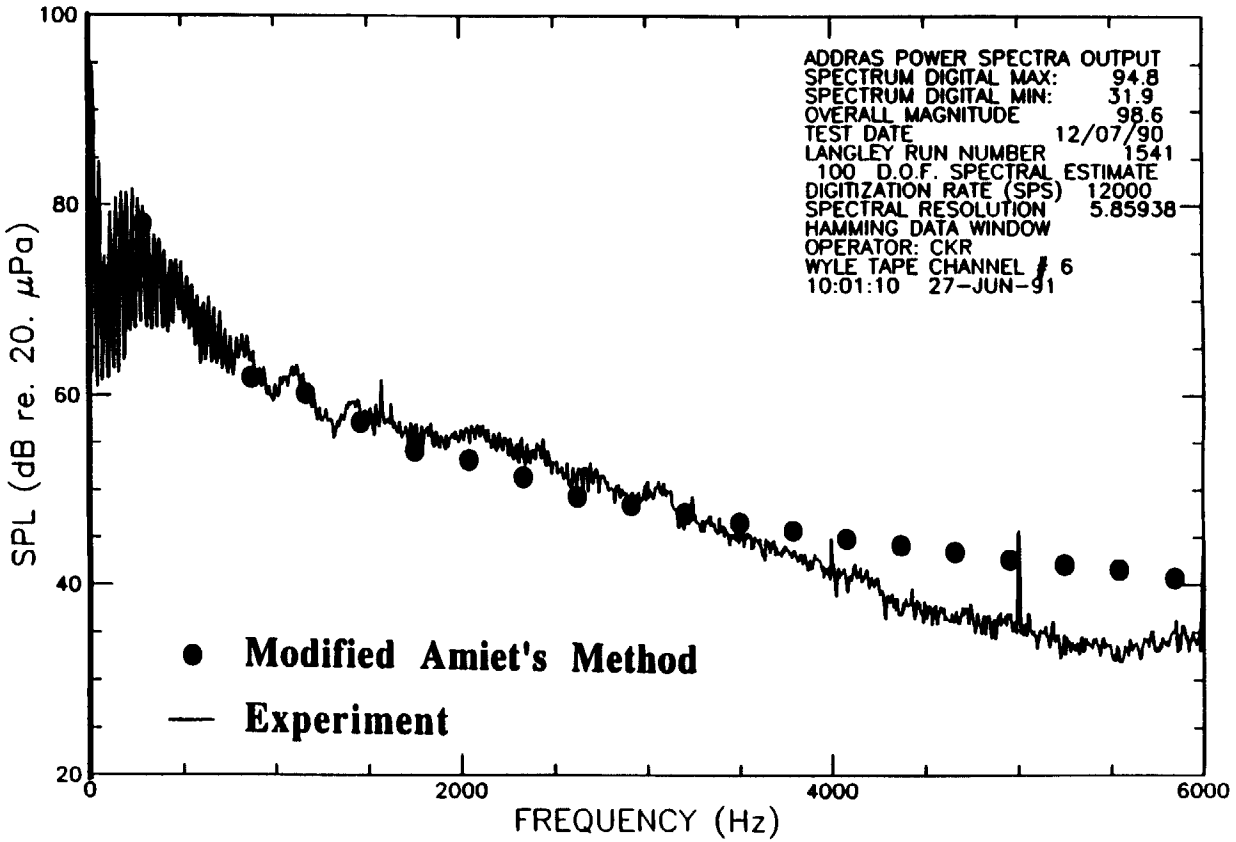

Figure 4.4c Comparison of experimental and predicted broadband noise spectra. Rear aircraft acoustics, $\theta = 23°$. Langley/Ames XV-15 ATB hover test.

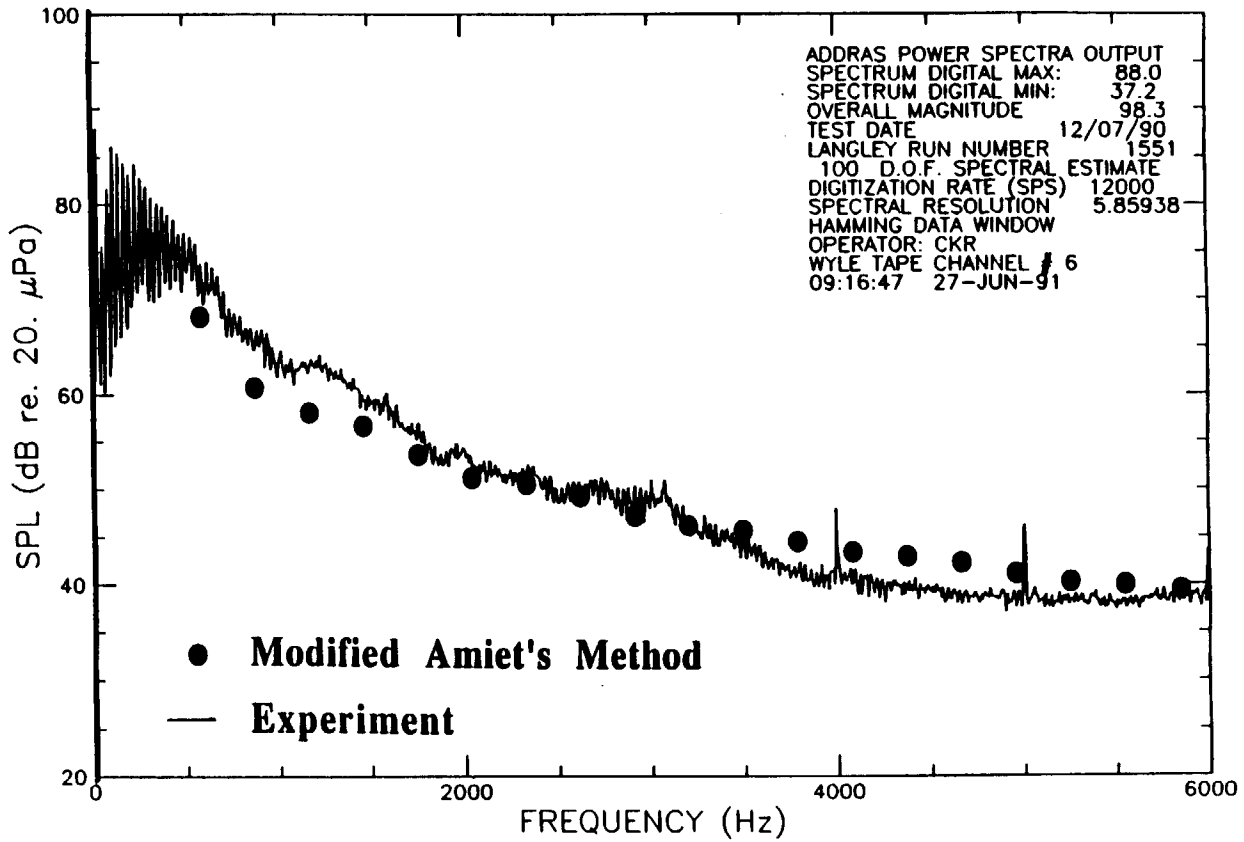

Figure 4.4d Comparison of experimental and predicted broadband noise spectra. Rear aircraft acoustics, θ = 45.7°. Langley/Ames XV-15 ATB hover test.

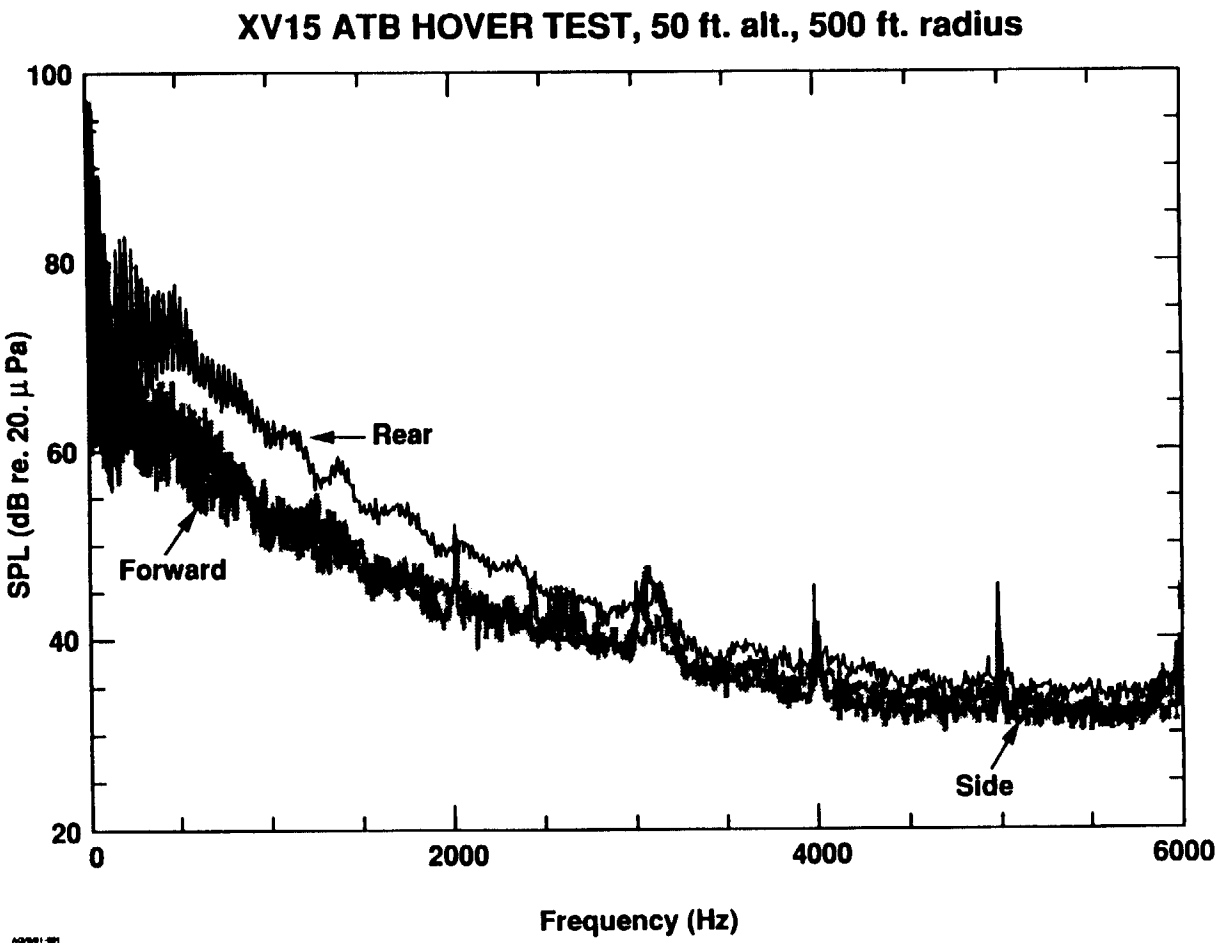

Figure 4.5.e Experimental broadband noise spectra. Front, rear, and side aircraft acoustics. θ=7.2°. Langley/Ames XV-15 ATB hover test.

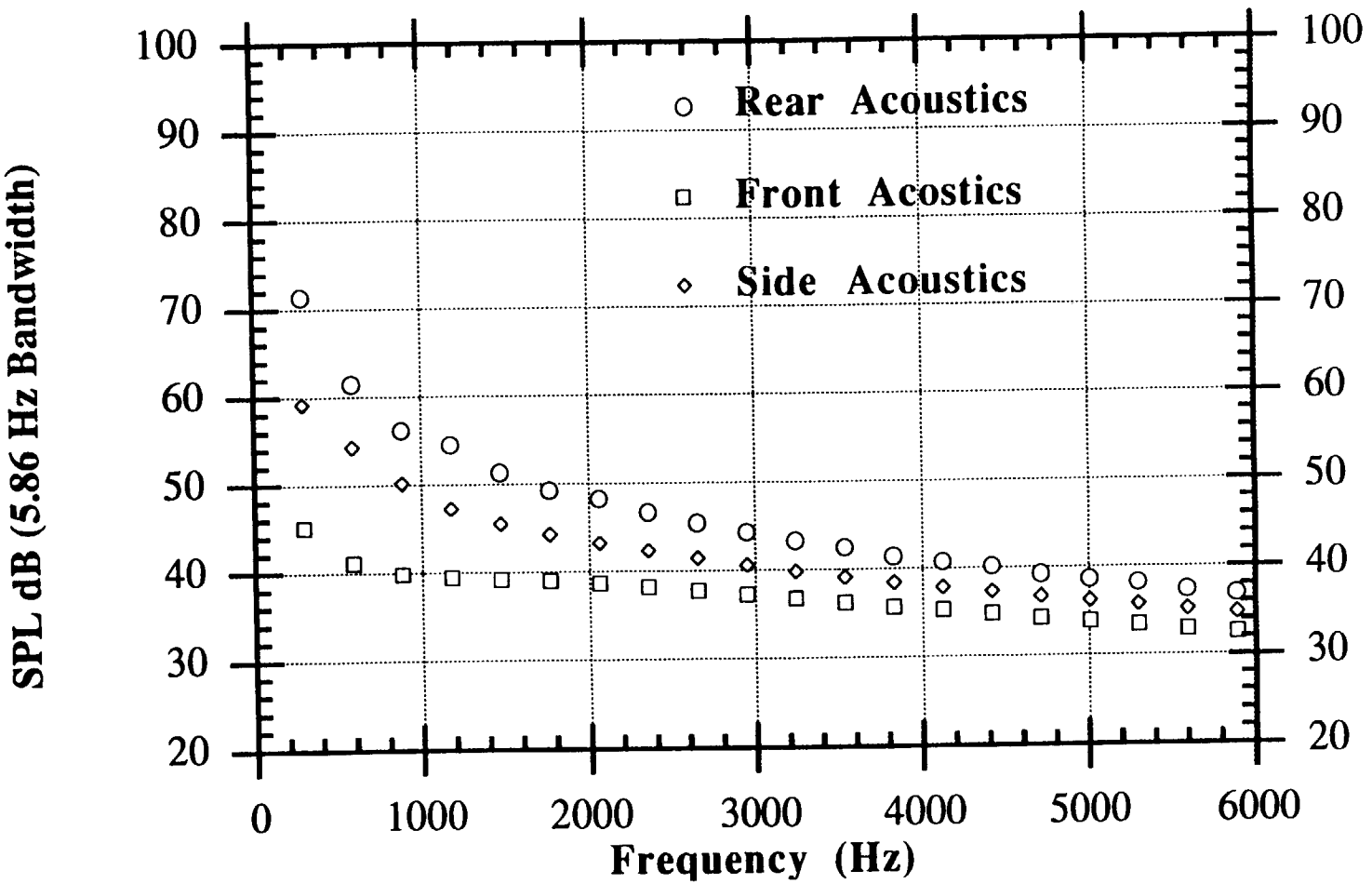

Figure 4.5.p Predicted broadband noise spectra. Front, rear, and side aircraft acoustics. $\theta=7.2°$. Langley/Ames XV-15 ATB hover test.

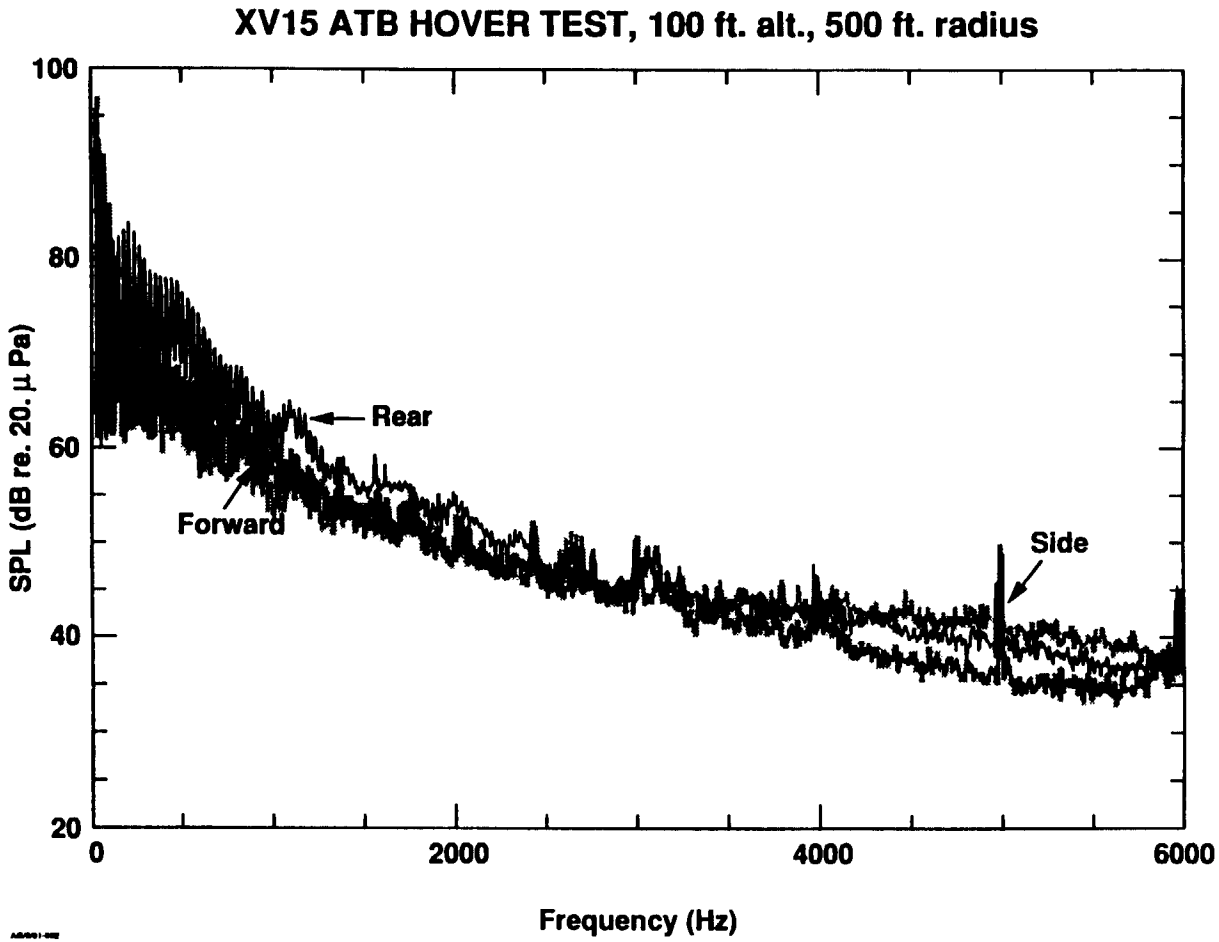

Figure 4.6.e Experimental broadband noise spectra. Front, rear, and side aircraft acoustics. θ=12.7°. Langley/Ames XV-15 ATB hover test.

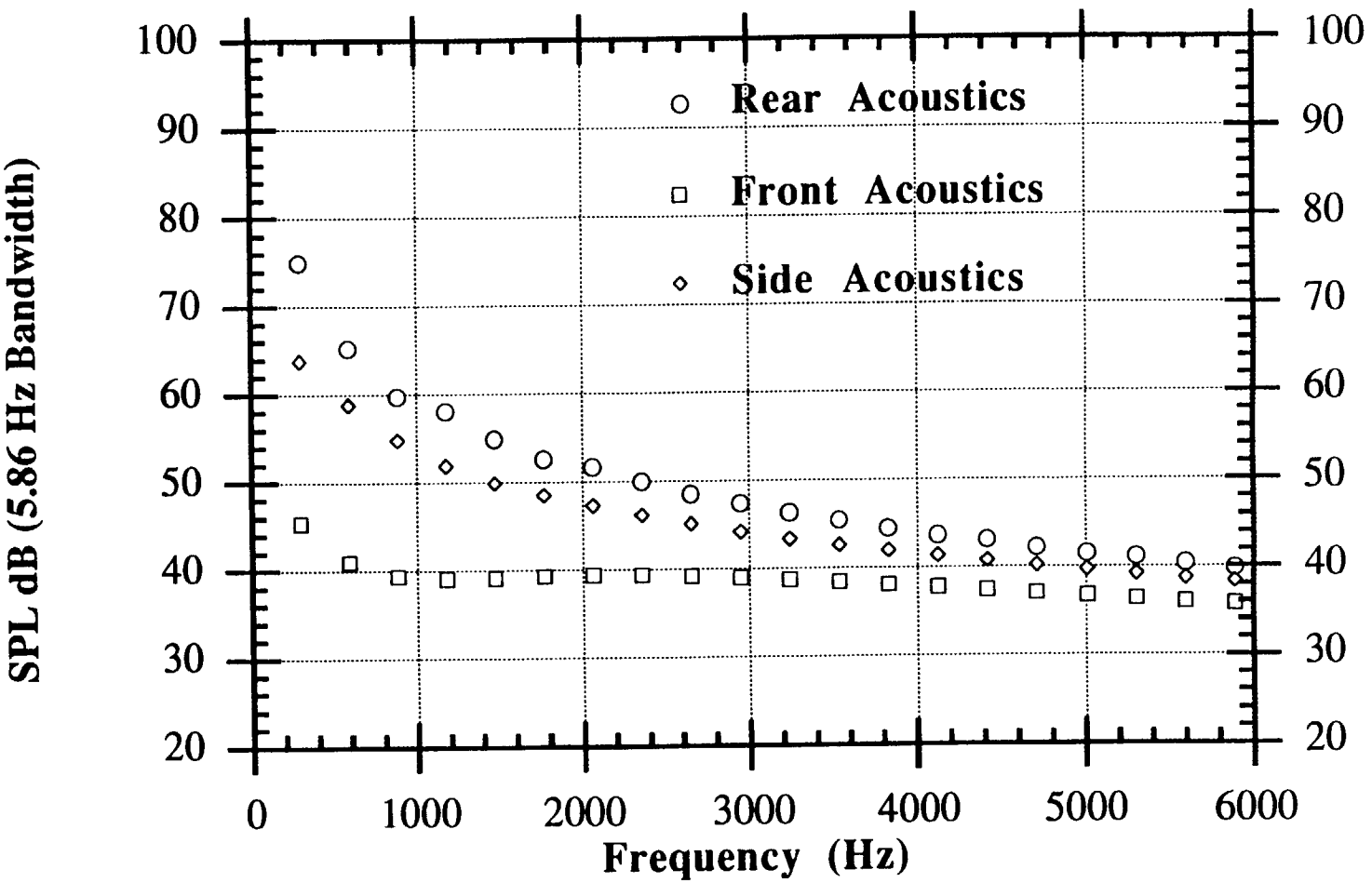

Figure 4.6.p Predicted broadband noise spectra. Front, rear, and side aircraft acoustics. θ=12.7°. Langley/Ames XV-15 ATB hover test.

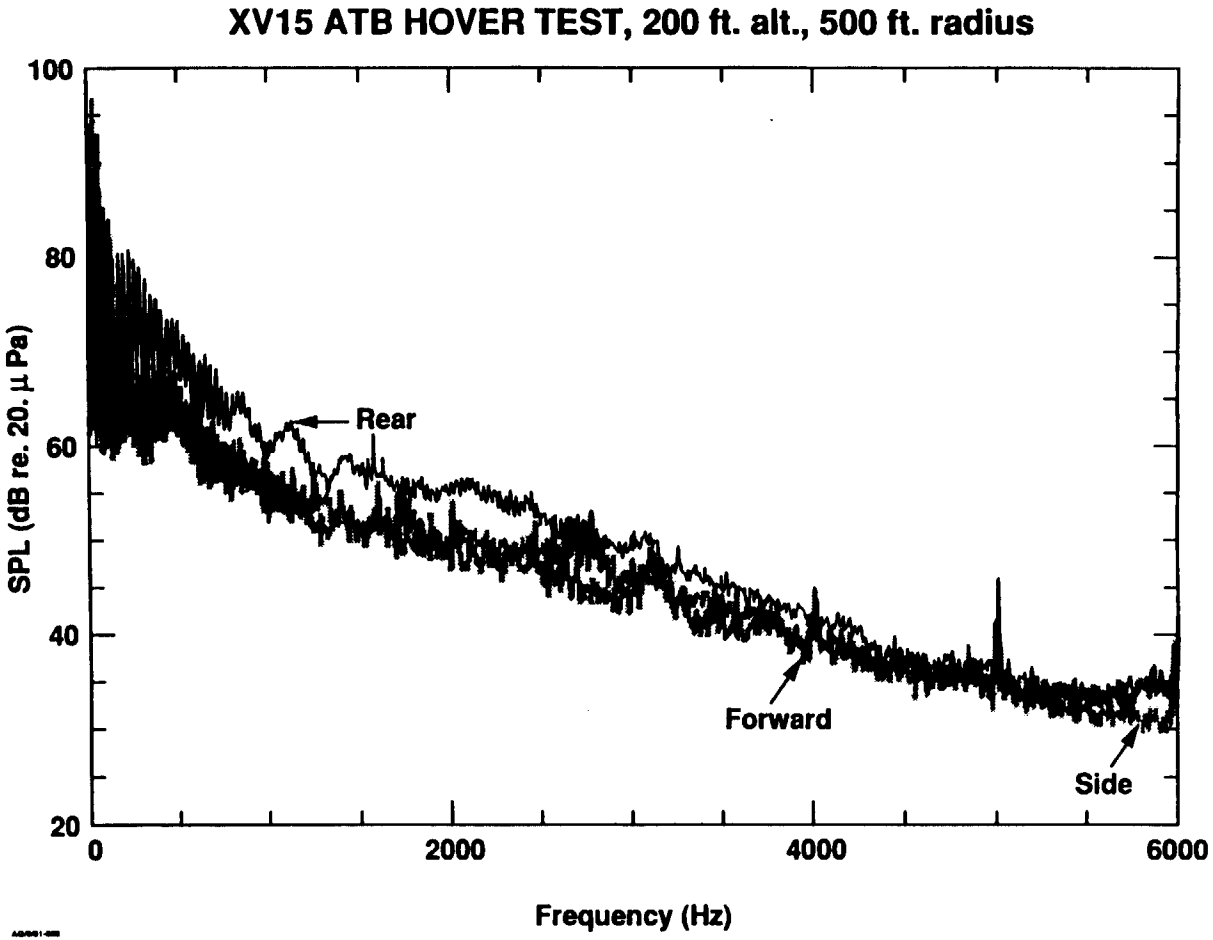

Figure 4.7.e Experimental broadband noise spectra. Front, rear, and side aircraft acoustics. θ=23°. Langley/Ames XV-15 ATB hover test.

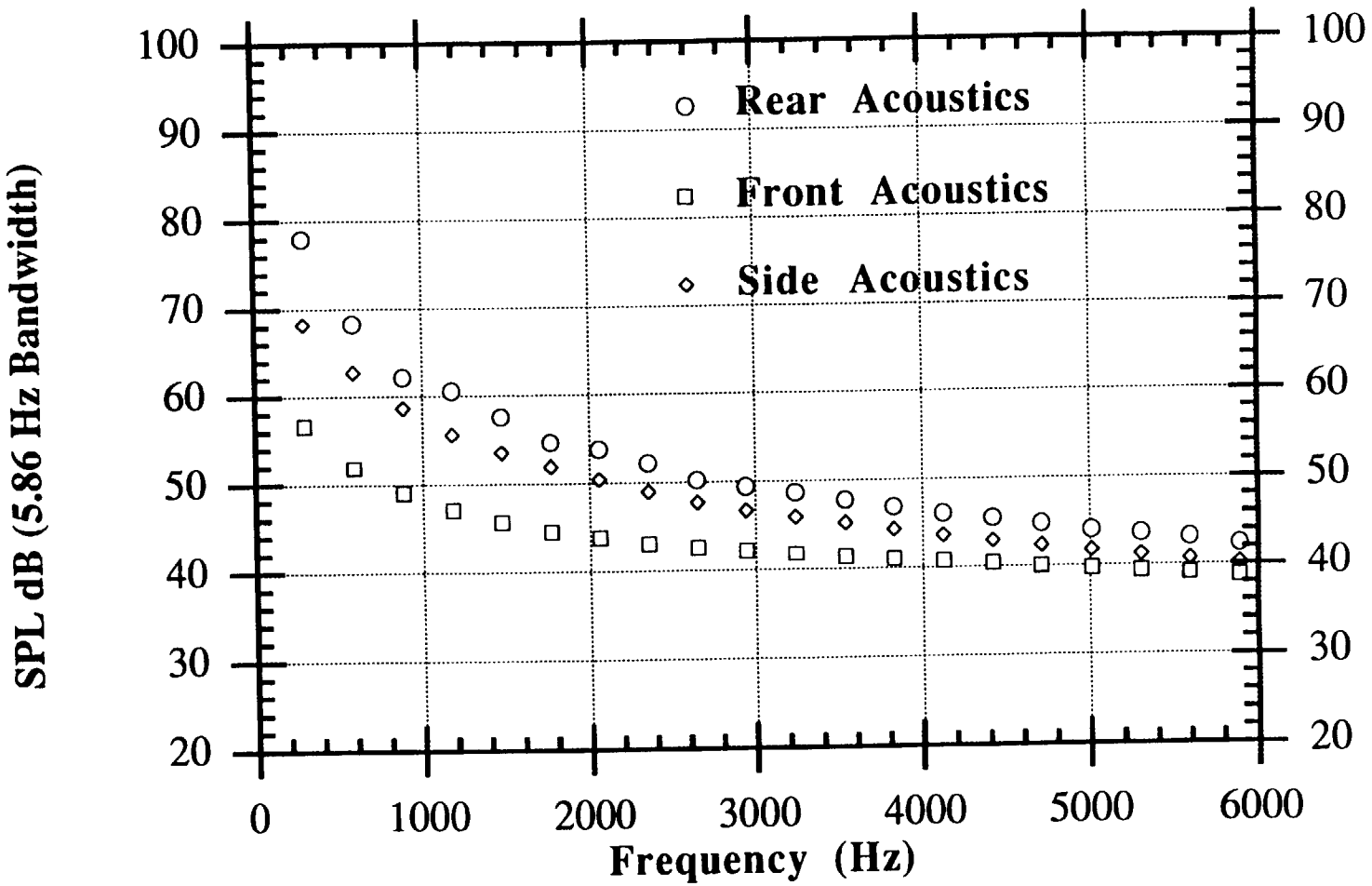

Figure 4.7.p Predicted broadband noise spectra. Front, rear, and side aircraft acoustics. $\theta=23°$. Langley/Ames XV-15 ATB hover test.

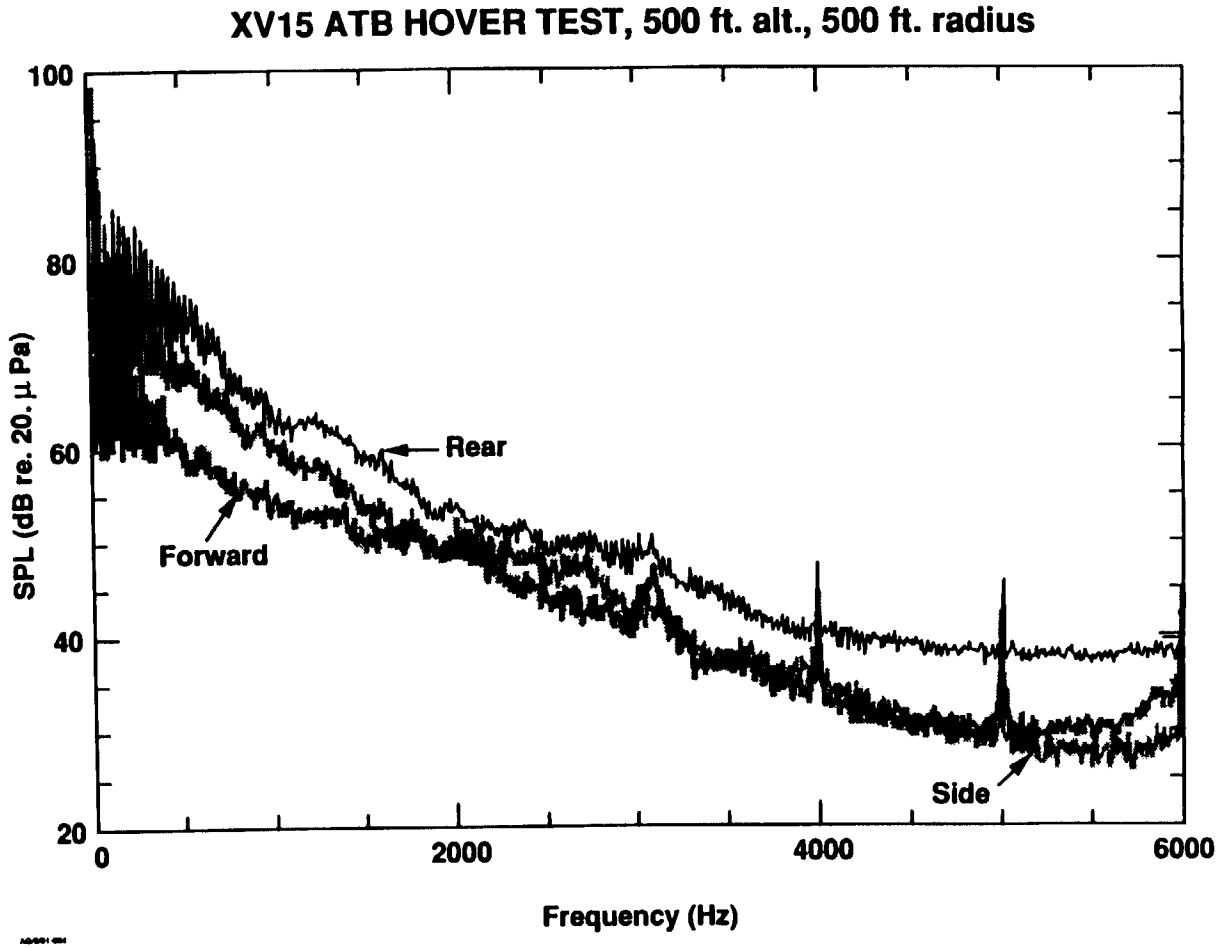

Figure 4.8.e Experimental broadband noise spectra. Front, rear, and side aircraft acoustics. θ=45.7°. Langley/Ames XV-15 ATB hover test.

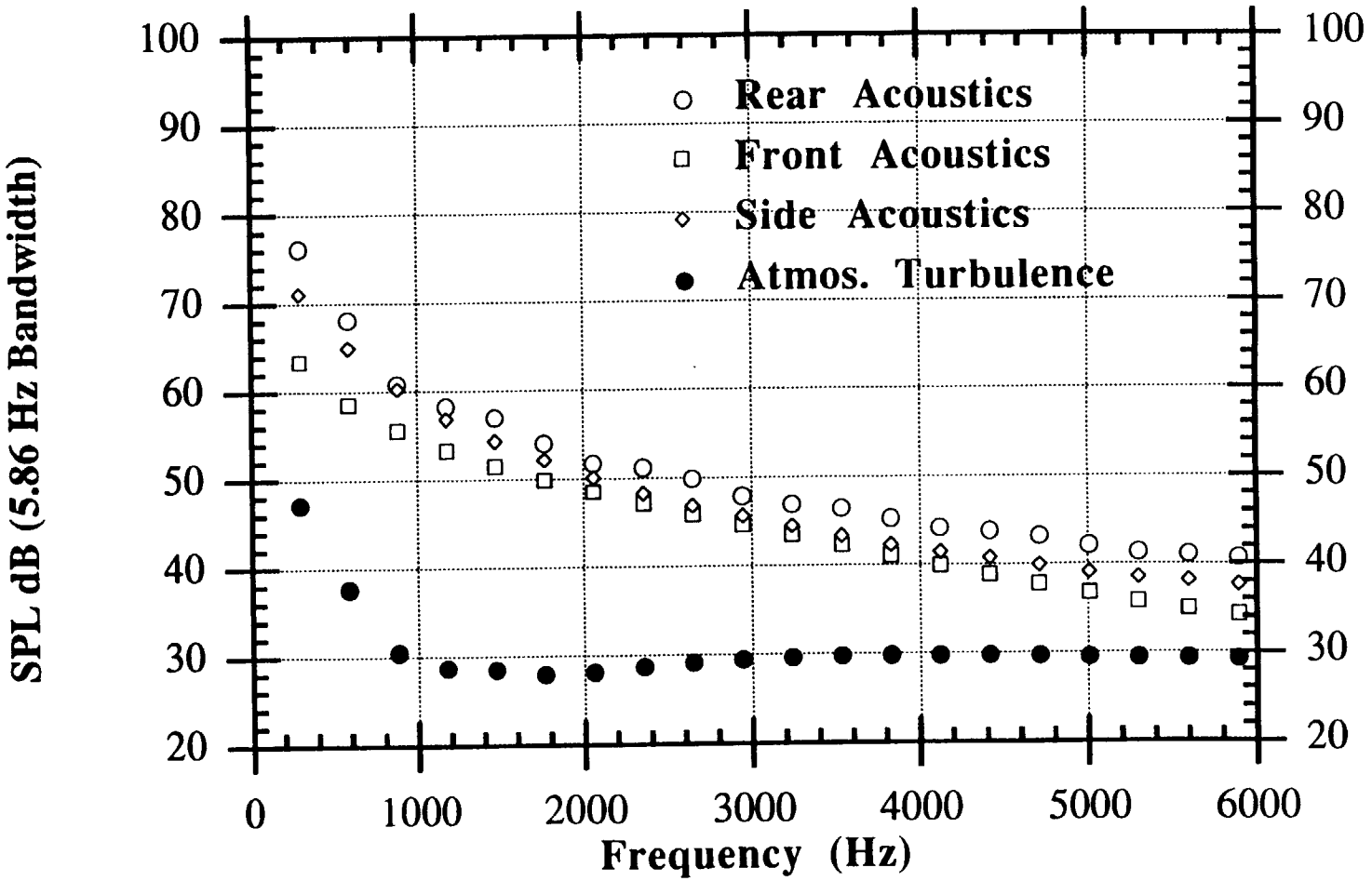

Figure 4.8.p Predicted broadband noise spectra. Front, rear, and side aircraft acoustics. θ=45.7°. Langley/Ames XV-15 ATB hover test.

also accurately predict the difference in dB levels for the three azimuthal observer locations. For the polar angle of 45.7°, the azimuthal dB difference is significantly greater at high frequency in the experiment than in the prediction.

Surprisingly, the accuracy of the predictions seems to decrease as the polar observer angle moves out of the rotor plane. The noise prediction method is based on a fluctuating lift dipole which radiates preferentially perpendicular to the rotor plane. The method also does not account for blade twist. Thus the assumptions of the prediction method tend to break down for polar angles less than 15°. Thus one would expect better accuracy for the out of plane cases.

This inconsistency may be explained by the fact that the modifications made to Amiet's method to account for azimuthally varying turbulence has not been 'tuned' to this experimental set of data. Better predictions could be obtained by decreasing the size of the reingestion zone as defined in the code. However, the modifications to Amiet's method used in the calculations were made independent of the calculations and therefore represent a best guess based on the available data. More extensive experimental testing would lead to better models and more accurate definitions of the flow characteristics required to make accurate modifications to Amiet's code.

These predictions do indicate that the broadband noise levels can be reasonably well predicted using the method of Amiet with modifications to account for high turbulence levels in the reingestion zone. Figure 4.8.p shows the predicted sound spectrum

using Amiet's method without modifications. This prediction is shown by the solid dots labelled "Atmos. Turbulence". This calculation shows that the unmodified method significantly underpredicts the broadband noise levels by 10 - 20 dB depending on frequency. Thus one can conclude that the high broadband noise levels for a hovering tilt rotor are indeed due to the high levels of inflow turbulence caused by the recirculating flow in the reingestion zone.

Chapter V.
Conclusions

This study has examined a broad range of issues which affect tilt rotor hover aeroacoustics. The main results of this study are described in the following sections.

5.1 Summary of 1/12 Scale Model Experiments

1. The recirculating fountain has been studied and recorded in photos and videos. This flow phenomenon is identified by opposing spanwise flows which meet at an unsteady separation point on the fuselage. The flow erupts over the rotor plane and is reingested.

2. Side views of the model indicate that an unsteady recirculating flow exists along and above the length of the fuselage. This aspect of the flow was previously unidentified and its characteristics warrant future study.

3. The fountain flow is an multi-directional phenomenon and efforts to study or model the flow in two dimensions will not capture all the important aspects of the flow.

4. The recirculating fountain is strongly time dependent as it tends to randomly shift about the aircraft's longitudinal axis. This

causes intermittency effects which cannot be studied by replacing one side of the model with an image plane.

5. The unsteadiness and intermittency of the fountain flow were observed with velocity time traces obtained using hotwire anemometry. The time traces also indicated much more turbulent flow over the rear of the aircraft than over the nose.

6. Turbulence spectra indicate that inflow turbulence in the re-ingestion zone over the rotor contains 5 - 10 time as much energy per unit frequency over a broad range of frequencies than is in the basic inflow turbulence of a single rotor with no fuselage or wing.

7. Contour plots of mean and rms velocities were generated at a height of one inch above the rotor plane. These contours indicate a velocity deficit in the axial component of the inflow velocity in the region over the wing. This deficit is due to the partial ground plane caused by the wing. The contour plot of rms velocity shows high values over part of the rotor. These high values are due to the highly turbulent flow being reingested. Both the inflow velocity deficit region and the reingestion region are clearly observed on the contour plots.

8. The results of this study are of a semi-quantitative nature. The Reynold's numbers are lower than for the XV-15 aircraft and the rotor blade geometries are not scaled precisely. Some moderate

assumptions were needed to reduce the hot wire velocity measurements. Future studies are planned under more rigorous conditions in order to study the details of the flow, further quantify it, and look for methods of altering the flow.

5.2 Summary of WOPWOP Discrete Noise Predictions

1. The fountain effect, which is due to the partial ground plane caused by the wing, is the dominant source of discrete frequency noise for a hovering tilt rotor. Mathematical modelling of this phenomenon has resulted in satisfactory noise predictions using WOPWOP. The calculations are accurate in predicting both approximate magnitudes and shape of the acoustic signal as well as capturing the directionality trends of the noise radiation.

2. The experimental results indicate that the fountain effect varies randomly in time and space. Acoustic time traces indicate that the entrance to the fountain region is well defined while the exit is not. Thus the mathematically deterministic model used in the predictions can only represent a characteristic instance of the fountain effect. This leads to scalloping in the predicted spectra and overpredictions of the negative peak pressures in the time domain.

3. Approximate chordwise loading distributions are shown to be acceptable for discrete frequency calculations. A triangular

loading distribution has been shown to give similar acoustic results as a chordwise accurate distribution.

4. Dynamic airfoil response should be included in the prediction scheme when the aeroacoustic mechanisms include impulsive blade loadings, such as from the fountain effect.

5. Comparisons between calculations using the ATB and metal blade rotor geometries indicate that the acoustic signal can be modified by changing the rotor geometry.

5.3 Summary of Broadband Noise Predictions

1. Modifications to Amiet's method have resulted in a means of predicting broadband rotor noise with azimuthally varying inflow turbulence characteristics. The azimuthally varying turbulence characteristics were extrapolated from 1/12 scale model experimental results.

2. Noise predictions based on this modified Amiet's method compare well with experimental results. The broadband noise levels are accurate to within a few dB and the directionality of the sound radiation is also predicted. Better predictions may be obtained through more accurate knowledge of the azimuthally varying turbulence characteristics.

3. The good correlation between the predictions and experiment indicate that the highly turbulent, reingested inflow is the dominant broadband noise mechanism for a hovering tilt rotor.

5.4 Final Remarks

While this study represents a first attempt to address many issues, its results are conclusive. The fundamentals of tilt rotor hover flow phenomena and noise mechanisms are now well understood. The primary issue is the interaction between the rotor, wing and rotor wake. Steps can now be taken to lessen the negative effects of this interaction. Doing so should result in quieter designs and improved hover configurations.

Appendix A

Rotor Propeties and Operating Conditions for Metal Blade Calculations

Rotor and Blade Properties

Station Number	Radial Station r/R	ft	Chord (ft)	Thickness Ratio t/c	Twist degrees	Airfoil Section
1	0.00	0.00	1.5167	0.35	0.00	NACA 64-935
2	0.17	2.15	1.2771	0.28	-10.392	NACA 64-528
3	0.19	2.33	1.2567	0.27	-11.278	*
4	0.25	3.13	1.1667	0.26	-15.104	*
5	0.40	5.00	1.1667	0.21	-24.167	*
6	0.45	5.63	1.1667	0.20	-26.337	*
7	0.50	6.25	1.1667	0.19	-29.130	*
8	0.53	6.63	1.1667	0.18	-29.922	NACA 64-118
9	0.60	7.50	1.1667	0.17	-31.771	*
10	0.70	8.75	1.1667	0.14	-34.413	*
11	0.81	10.13	1.1667	0.12	-37.318	NACA 64-(1.5)12
12	0.91	11.31	1.1667	0.10	-39.827	*
13	0.95	11.88	1.1667	0.09	-41.016	*
14	1.00	12.50	1.1667	0.08	-42.337	NACA 64-208

* Properties vary linearly between stated values

Rotor

Number of blades per rotor	3
Diameter	25.0 ft
Disc area per rotor	491 sq. ft
Solidity	0.089
Hub precone angle	2.5 degrees
delta 3	-15.0 degrees
Blade Lock number	3.83
Blade cut out radius	1.06 ft

Computational Operating Conditions

Speed of sound	343.0 m/s
Ambient density of air	1.21 kg/m^3
Velocity	0.0 m/s
Angle of descent	0 degrees
Observer distance to rotor	60.8 m
Elevation angle	10.81 degrees
Coefficient of thrust	0.0091
Rotor RPM	565
Nacelle angle	90 degrees
Aircraft gross weight	13000 lb

Appendix B

Explanation of Coefficient of Pressure Calculation

This calculation is based on the velocity addtion method of Abbott and Von Doenhoff presented in Theory of Wing Sections.[22] The theory of thin wing sections shows that the loading component of the pressure distribution of a thin airfoil section may be considered to consist of a basic distribution at the ideal angle of attack due to camber, a distribution proportional to the angle of attack as measured from the ideal angle of attack, and an additional distribution associated with the basic thickness form (symmetrical section) at zero angle of attack (pp. 75-76)

The load at a chordwise position is caused by a pressure difference between the upper and lower surfaces. It is assumed that the velocity increment on one surface is equal to the velocity decrement on the other surface. Using the method of velocity addition, the coefficient of pressure, S = 1-Cp, can be calculated by adding the velocity increment corresponding to camber, $\frac{\Delta v}{V}$, and the velocity increment corresponding to angle of attack, $\frac{\Delta v_a}{V}$, to the velocity increment due to the basic thickness form, $\frac{v}{V}$.

$$S = \left(\frac{v}{V} \pm \frac{\Delta v}{V} \pm \frac{\Delta v_a}{V}\right)^2 \qquad \text{(B.1)}$$

Values of the ratios corresponding to one value of $\frac{x}{c}$ are added together and the resulting value of the pressure coefficient S is

assigned to the surface of the wing section at the same value of $\frac{x}{c}$. The values of $\frac{\Delta v_a}{V}$ and $\frac{\Delta v}{V}$ are added on the upper surface and subtracted on the lower surface. In this way a pressure distribution about an airfoil can be calculated where C_p = 1-S.

A correction must be made as the pressure distribution is being calculated for an arbitrary c_l, not c_{li}. For this reason, the ratio $\frac{\Delta v_a}{V}$ must be corrected by multiplying by a factor, $f(\alpha)$. As a first approximation:

$$f(\alpha) = \frac{c_l - c_{li}}{c_{lo}} \tag{B.2}$$

$$c_l = c_{li} + \frac{dc_l}{d\alpha}(\alpha - \alpha_i) \tag{B.3}$$

$$f(\alpha) = \frac{dc_l}{d\alpha}\ \frac{\alpha - \alpha_i}{c_{lo}} \tag{B.4}$$

and c_{lo} is taken to be unity.

The ratio $\frac{\Delta v}{V}$ must also be corrected as the value of the design c_l will be higher than c_{li} of the camber line by an amount dependent on the thickness ratio of the basic thickness form. This discrepancy is caused by applying the values of $\frac{\Delta v}{V}$ obtained for the mean line to the sections of finite thickness where $\frac{v}{V}$ is greater than unity over most of the surface. So $\frac{\Delta v}{V}$ is multiplied by the design lift coefficient divided by the design lift coefficient of the mean line.

This method is known to be very accurate for thin airfoils with thin boundary layers and low drag coefficients. However, the data estimated for the 28% and 35% airfoils may be significantly in error.

The velocity addition method was applied to the input subroutine as no empirical data for the XV-15 rotor was available and any type of panel method would be computationally inefficient. The velocity addition method allows the fast and accurate calculation of the the pressure coefficients on the upper and lower surfaces at discrete chordwise locations at angles of attack when separation is not a problem.

Data for the 64 series thickness forms are tabulated in Appendix 1 and 2 of reference 22. These tables were entered as data statements in FORTRAN subroutines. Data had to estimated for the 28% and 35% airfoils from a 21% airfoil. $\frac{v}{V}$ was found by using equation. 6.5 of reference 22.

$$\left(\frac{v}{V}\right)t_2 = \left[\left(\frac{v}{V}\right) - 1\right]\frac{t_2}{t_1} + 1 \qquad \text{(B.5)}$$

$\frac{\Delta v_a}{V}$ was approximated by scaling the first 5% of the chord exponentially from several thinner airfoils and then using the same values as are given for the 21% airfoil. These values were used as it was noted qualitatively that these values changed little as thickness increased. As noted previously the velocity addition method is imprecise for thicker airfoils, the pressure distributions about these airfoils can be considered as approximate.

This tabulated data represents a two dimensional array of velocity ratios from which the desired values at a specific point on the rotor blade can be calculated by linearly interpolating from four surrounding defined data points. In this way a call to the FORTRAN subroutine identifies the four data points and then interpolates to produce the velocity ratios at the desired point.

Appendix C

Partial Ground Plane/Fountain Effect

Substantial loading noise is produced on the tilt rotor blades due to the partial ground plane caused by the wing below the rotor. The spatially varying velocity distribution was previously estimated based on smoke flow video tapes, and is substantiated by the hotwire results of chapter II. This analysis was used in the creation of a mathematical "fountain" model. This model defines the width of the the affected region to be approximately equal to 1/3 to 1/2 the wing chord. The partial ground effect is estimated to cause a 20% reduction in the inflow velocity over the affected region. The inflow velocity distribution was made to be symmetric about the rotor/rotor axis.

The following describes the mathematical model developed for determing the inflow velocity seen by a blade element as it passes through the fountain:

The distance from the rotor/rotor axis to the edge of the fountain is defined as:

$$\text{CHALF} = \frac{\text{RK1}}{2} \cdot \text{wing chord} + \frac{\text{RK2}}{2} \cdot \text{wing chord} \qquad \text{(C.1)}$$

and the width of the half sinusoid in the entry of the fountain is defined as:

$$\text{WHALF} = \text{RK2} \cdot \text{wing chord.} \qquad \text{(C.2)}$$

RK1 and RK2 are two defined constants. For the case of the sharp fountain, RK1 = 0.5 and RK2 = 0.1, and thus CHALF = 0.3•wing chord and WHALF = 0.1•wing chord. For the smooth fountain, RK1 = 0.5 and RK2 = 0.5, and thus CHALF = 0.5•wing chord and WHALF = 0.5•wing chord.

For a given blade element at a radial distance, r, from the hub, the inflow velocity is defined by four azimuthal angles. Ψ_1 is the angle swept out as the blade element rotates from $\Psi = 0$ to where the leading edge intersects the boundary of the fountain defined by CHALF. Ψ_2 is the angle swept out as the blade element rotates from $\Psi = 0$ to where the leading edge intersects the end of the fountain entrance region defined by CHALF - WHALF. Ψ_3, and Ψ_4 are the mirror image of Ψ_2 and Ψ_1 over the rotor/rotor axis. In summary:

$$\Psi_1 = \cos^{-1}\left(\frac{\text{CHALF}}{r}\right) \tag{C.3}$$

$$\Psi_2 = \cos^{-1}\left(\frac{\text{CHALF - WHALF}}{r}\right) \tag{C.4}$$

$$\Psi_3 = \cos^{-1}\left(\frac{\text{WHALF - CHALF}}{r}\right) \tag{C.5}$$

$$\Psi_4 = \cos^{-1}\left(\frac{\text{-CHALF}}{r}\right) \tag{C.6}$$

The spatially varying "fountain effect" was mathematically modeled by decreasing the inflow velocity, V_{inflow}, seen by a blade element as it passes through the fountain in the following manner:

$$\Psi_1 < \Psi < \Psi_2;\ V_{inflow} = V^* \cdot \left[1 - AMP \cdot \sin\left(\frac{\Psi - \Psi_1}{\Psi_2 - \Psi_1} \cdot \frac{\pi}{2} \right) \right] \tag{C.7}$$

$$\Psi_2 < \Psi < \Psi_3;\ V_{inflow} = V^* \cdot (1 - AMP) \tag{C.8}$$

$$\Psi_3 < \Psi < \Psi_4;\ V_{inflow} = V^* \cdot \left[1 - AMP \cdot \cos\left(\frac{\Psi - \Psi_3}{\Psi_4 - \Psi_3} \cdot \frac{\pi}{2} \right) \right] \tag{C.9}$$

Ψ is the azimuthal position of the blade element, AMP is the maximum fractional decrease of V^*, and V^* is the spatially uniform inflow velocity calculated from momentum theory. In the model used for the current calculations, AMP = 0.2, reflecting the 20% decrease in inflow at the mid-chord of the wing. At all other azimuthal positions, no change was made in the inflow velocity, thus the total inflow is not fully consistent with the momentum flux required by momentum analysis.

Appendix D

Modifications Made to Amiet's Code for Azimuthally Varying Turbulence

Modifications were made to the broad band noise prediction code of Amiet[27,28,29]. Amiet's method computes the sound levels by resolving the blades rotating motion into rectilinear segments. The sound generated by each segment is summed to calculate the sound generated by one blade rotation. It was possible to adapt the code such that each rectilinear motion has associated with it different turbulence characteristics. It is also possible to change the turbulence characteristics with radial station as Amiet's code sums over 20 radial stations.

Thus Amiet's code was modified such that the reingestion zone of the rotor disk was made to have higher turbulent intensities than the rest of the rotor disk. From looking at figure 2.22 which shows rms velocity inflow contours over the rotor plane, a reingestion zone was defined. 0° azimuth is defined by the blade being at the rear of the aircraft or at 6 o'clock looking down from the rear of the aircraft. The reingestion zone was defined as the region between azimuthal angles of 250° and 330° and between radial stations r/R = 0.4 and 1.0. Thus the rotor blade encounters the reingestion zone when it has rotated 250° from its starting point at zero azimuthal angle and exits the zone after 330° of rotation. The calculation of Amiet's code proceeds counter clockwise which corresponds to the starboard rotor on the model or the XV-15. The

contour plot of rms inflow velocity, figure 2.22, shows the port rotor of the model which rotates clockwise.

In the reingestion zone, the turbulent intensities encountered by the blade and their associated length scale correspond to the high turbulence levels due to the recirculating fountain. Over the rest of the disk the turbulent intensity is defined by the ambient turbulence for which the rms inflow velocity is generally accepted as 1 m/s. The length scale, λ_f, is defined as 90% of the hover height[32].

The code also had to be modified to accept different azimuthal observer locations. The code begins the calculation at blade position of 90° azimuth and sums blade motions through 450°, one revolution. In order to change the azimuthal observer location, the absolute angle at which the blade encounters the fountain had to be changed for each observer location. Thus the paradigm used here is that the observer is always on the minus y axis, 0° or 360° azimuth, and the blade motion begins on the positive x axis, 90°, and rotates counter clockwise. The observer location is implemented by altering the azimuthal angle at which the blade intersects the reingestion zone. In pseudo code the test for determining if the blade is in the reingestion zone is:

```
IF (GAMMA + OBS_ANGLE .GE. 250 .AND.
GAMMA + OBS_ANGLE .LE. 330 .AND.
r/R .GE. 0.4) THEN
      blade segment is in the reingestion zone
ELSE
      blade segment is not in the reingestion zone
END IF
```

GAMMA is the blade azimuthal location, 0° to 450°. OBS_ANGLE is the observer azimuthal angle for the noise prediction. For example, computing the rear acoustics requires setting OBS_ANGLE to 0°. Computing the front acoustics requires setting OBS_ANGLE to 180° etc. The observer angle is defined the user in the input deck.

Also, the I/O procedure Amiet's code was significantly modified to be run in batch mode on a Micro-Vax. The user is required to define the calculation via an input file, rather than key in data at screen prompts. This modification has obvious benefits to the user. A theory manual and a user manual exist for Amiet's unmodified code. These are NASA contractor reports[29,30].

Lastly, the output of Amiet's code has to be modified for a two rotor system. The simplest assumption, accurate at observer distances large compared to the hub separation distance, is to assume the two rotors are located at the same position at the center of the aircraft (intersection of the longitudinal and rotor/rotor axis). For observer locations in the longitudinal plane of symmetry, the sound power levels due to the two rotor system can be determined by doubling the power calculated for the one rotor system. This effectively adds 3 dB to the one rotor calculation. The doubling of the power is because the blade has the same Mach number component in the observer direction as it passes through the reingestion zone. This means that the two rotors are radiated the same sound power in the observer direction.

A slightly different approach is required for calculating the sound power radiated by the two rotor system in directions not in

the longitudinal plane of symmetry. These observer locations require two calculations, one calculation for the desired observer location and another calculation for an observer location which is the reflection of the desired observer location about the longitudinal plane of symmetry. The two rotor sound power level is then the sum of the two single rotor sound power level calculations.

The sound power levels predicted by Amiet's code must also be modified to compare to experiment. Ground plane microphones measure approximately twice the acoustic pressure which increases the measured sound power be approximately 6 dB at all frequencies. Also the measured data may not be normalized to a 1 Hz bandwidth. In this case the predicted values must be increased by 10 $\log_{10}(\Delta f)$, Δf = the bandwidth or spectral resolution of the experimental data.

For the case of the observer in the longitudinal plane of symmetry, the sound powers predicted by Amiet's code are increased by 16.7 dB; 3 dB to account for the two rotor system, 6 dB to account for the ground plane microphone, and 7.7 dB to account for the 5.86 Hz spectral resolution of the experimental data presented here.

Appendix E

Scaling of Model Inflow Turbulence to XV-15 Inflow Turbulence

The turbulence characteristics measured on the 1/12 scale model were scaled to the XV-15 so that they could be used as input for the broad band noise predictions. It was assumed that the turbulent fluctuating velocity, u_{rms}, and the turbulent convection velocity, V_c, would scale proportionally with the momentum inflow velocities. Thus the momentum inflow velocity for the two rotors is used as the scaling factor for scaling velocities between the model and the XV-15.

The momentum inflow velocity is defined as:

$$V_{momentum} = \sqrt{\frac{thrust}{2\rho Area}} \qquad \text{(E.1)}$$

The thrust is the lifting force generated by the rotor and Area is the area of the rotor disk. The thrust is known for the XV-15. The thrust generated by the model rotor was calculated by summing the contributions to the momentum flux at each grid point over the rotor disk. ie:

$$(thrust)_{model} = \sum_{i=1}^{N} \rho A_i V_i^2 \qquad \text{(E.2)}$$

And the momentum inflow velocity can be calculated:

$$(V_{momentum})_{model} = \sqrt{\frac{\sum_{i=1}^{N} \rho A_i V_i^2}{2\rho Area}} \qquad (E.3)$$

V_i is the vertical component of velocity measured 1" above the rotor plane at the i'th grid point and A_i is the area of one grid element. Because of the way in which the vertical component of velocity was calculated from the Cartesian hot wire measurements, only the non-zero V_i's were used in the sum. Thus the thrust is calculated from the momentum flux due to non-zero velocity grid points. As can be seen from figure 2.21b, the non-zero velocity grid points were generally inside of the rotor swept area. Also note that A_i is the same for each grid point. so the equation for the momentum inflow velocity of the model reduces to:

$$(V_{momentum})_{model} = \sqrt{\frac{\sum_{i=1}^{N} V_i^2}{2N}} \qquad (E.4)$$

where N is the number of non-zero grid points. There are 467 non-zero grid points and $\sum_{i=1}^{N} V_i^2 = 24{,}623\ m^2/s^2$. The momentum inflow velocity of the is 5.13 m/s.

The turbulent convection velocity of the model was approximated by the average measured vertical component of velocity measured 1" above the rotor plane. This was calculated by

summing the non-zero vertical velocity components V_i, and dividing by N. The average vertical component of velocity is 6.72 m/s.

The turbulent convection velocity V_c was scaled as follows:

$$\left(\frac{V_c}{V_{momentum}}\right)_{model} = \left(\frac{V_c}{V_{momentum}}\right)_{XV\text{-}15} \qquad \text{(E.5)}$$

The turbulent fluctuating velocity u_{rms} was scaled as follows:

$$\left(\frac{u_{rms}}{V_{momentum}}\right)_{model} = \left(\frac{u_{rms}}{V_{momentum}}\right)_{XV\text{-}15} \qquad \text{(E.6)}$$

These are the main results of this section.

The result of calculating the thrust of the model rotor is ~16.5 Newtons. This is approximately 3.7 lbs of thrust which is a reasonable result.

This analysis illustrates the deficiencies of using the momentum inflow velocity as the turbulent convection velocity, a common approximation. The average vertical velocity over the rotor disk is ~30% higher than the momentum inflow velocity. This means the turbulent intensity, $\frac{u_{rms}}{V_{convection}}$, will be ~30% higher if $V_{momentum}$ is used for $V_{convection}$. The turbulent intensity is a commonly used dimensionless parameter for describing the magnitude of the turbulent velocity fluctuations. This is an important consideration as reducing u_{rms} by 30% decreases the predicted sound levels by ~3 dB. Thus calculating u_{rms} from the

turbulent intensity may introduce a significant error if the wrong convection velocity is used.

Another problem with using $V_{momentum}$ instead of $V_{convection}$ is that is reduces the Mach number of the turbulent convection velocity. This lowers the predicted sound levels as the airfoil lift response function is a function of the turbulent convection velocity Mach number. Decreasing the turbulent convection velocity Mach number 30% decreases the predicted levels by ~1.5 dB.

The above analysis gives the following results for scaling the turbulence characteristics of the model to the XV-15. Figure 2.22 shows the rms velocity contours 1" above the rotor plane. A $u_z'^2$ value of 2 m^2/s^2 is approximately the characteristic value of the rms velocity fluctuations in the reingestion zone. From above, V_c ~6.72 m/s. From equations E.5 and E.6, $(V_c)_{XV\text{-}15}$ ~22.36 m/s and $(u_{rms})_{XV\text{-}15}$ ~4.71 m/s. Recall that $(V_{momentum})_{XV\text{-}15}$ = 17.07 m/s and $(V_{momentum})_{model}$ = 5.13 m/s. Thus the turbulent intensity, $\frac{u_{rms}}{V_c}$ = 0.21.

Matching the Von Karman Longitudinal Spectrum to the measured Longitudinal Spectrum (see appendix F) resulted in a length scale λ_f ~0.025 m, approximately the blade chord. The turbulent length scale for the XV-15 was scaled by the rotor chord and is 0.356 m. Of course λ_f may actually be physically related to other geometrical measures such as the wing or fuselage geometry which also affects the recirculation. However, these also scale linearly with size. The ratio of the blade chords is approximately

the scale of the model ~1/12, so scaling λ_f with chord is an accurate assumption.

These scaling calculations represent the most logical extrapolation of the experimental data. However, the analysis would be incomplete without considering the upper and lower bounds of the scaling calculations. A lower bound would be to use the lowest turbulent intensity available from the experimental data. In the reingestion zone defined in the noise prediction code, this value is ~0.16. An upper bound generated from the experimental data is ~0.31. This gives upper and lower bound of + or - ~30%. The predicted sound level is proportional to $(\frac{u_{rms}}{V_c})^2$. This means the upper and lower bounds on the noise predictions are ± 3 dB of the result found by logically scaling the experimental data. Thus the amount of uncertainty in the calculation is minimal on a dB scale.

Appendix F

Method for Comparing Measured Longitudinal Spectrum with Von Karman Longitudinal Spectrum

Calculation of $F_{11}(k)$ from measurements:

Data was taken using a hot wire 1" above the rotor plane, 2" from the tip over the rotor disk on the rotor/rotor axis. The hot wire was oriented parallel to the rotor disk and longitudinal plane of symmetry. The hot wire measured 30,000 voltages evenly spaced in time for one second, 30,000 samples per second. The voltages were converted to velocities via King's Law[17]. The power spectrum of this data stream was computed via the program SPCTRM in Numerical Recipes.[36] The output of this program is the power spectrum per calculated Fourier component. The power spectral density (per unit frequency) is found by dividing the above result by Δf, the spectral resolution. The correctness of this method was checked as follows; the first Fourier component, a_0, is the square of the measured mean velocity, and the area under the PSD curve is the square of the measured rms velocity.

The power spectral density of the hot wire measurement was reduced to the Longitudinal Spectrum, $F_{11}(k)$ by the following method. The PSD(f) was converted from frequency to wave number by the relation:

$$\frac{2\pi f}{U_{mean}} = k \qquad (F.1)$$

The amplitude of the PSD(f) was multiplied by $\frac{U_{mean}}{2\pi}$ and plotted as a function of wave number, k. As a final check, integrating the area under the calculated $F_{11}(k)$ gives the square of the measured rms velocity, 4 m^2/s^2. The above procedure was conducted for ten such data streams the results averaged to give a better estimate of $F_{11}(k)$.

The measured PSD was reduced to the Longitudinal Spectrum, $F_{11}(k)$, in order to compare the Von Karman energy spectrum, E(k) used in the broadband noise prediction code to measured spectra. This comparison is possible because a simple relation exists between the energy spectrum and the longitudinal turbulence spectrum for isotropic turbulence.[37]

$$E(k) = k^3 \frac{d}{dk}\left(\frac{1}{k}\frac{dF_{11}(k)}{dk}\right) \qquad (F.2)$$

The Von Karman Spectrum, E(k) is defined as

$$E(k) = \frac{I\, k^4}{\left[1 + \frac{k^2}{k_e^2}\right]^{17/6}} \qquad (F.3)$$

$$I = \frac{55}{9\sqrt{\pi}} \frac{\Gamma(5/6)}{\Gamma(1/3)} \frac{u'^2}{k_e^5} \qquad (F.4)$$

$$k_e = \frac{\Gamma(5/6)}{\Gamma(1/3)} \frac{\sqrt{\pi}}{\lambda_f} \qquad (F.5)$$

λ_f is the turbulent length scale and u' is the rms of the vertical component of velocity, the square root of the area under the $F_{11}(k)$ curve. For the model, u' = 2.0 m/s and λ_f = 0.025 m, the length of the rotor chord.

$F_{11}(k)$ for the Von Karman energy spectrum can be found by integration and setting the constants of integration to zero. The result is:

$$F_{11}(k) = \frac{9}{55} \frac{I\, k_e^4}{[1 + \frac{k^2}{k_e^2}]^{5/6}} \qquad \text{(F.6)}$$

And so $F_{11}(k)$ can be compared for the Von Karman and measured spectra.

REFERENCES

1. Coffen, C. D., George, A. R., Hardinge, H., and Stevenson, R. (1991). "Flow Visualization and Flow Field Measurements of a 1/12 Scale Tilt Rotor Aircraft in Hover," Proceedings of the American Helicopter Society Technical Specialists' Meeting. October, 1991.

2. Coffen, C. D. and George, A. R. (1990). "Prediction of XV-15 Tilt Rotor Discrete Frequency Aeroacoustic Noise with WOPWOP," Cornell University Mechanical and Aerospace Engineering Report FDA-90-10, January 1990.

3. Coffen, Charles D. and George, Albert R. (1990). "Analysis and Prediction of Tilt Rotor Hover Noise," Proceedings of the 46th Annual Forum & Technology Display of the American Helicopter Society, Washington, D.C., May 21-23, 1990.

4. Rutledge, C. K., Coffen, C. D., and George, A. R. (1991). "A Comparative Analysis of XV-15 Tiltrotor Hover Test Data and WOPWOP Predictions Incorporating the Fountain Effect," Proceedings of the American Helicopter Society Technical Specialists' Meeting. Valley Forge, Pennsylvania. October, 1991.

5. Ffowcs Williams, J. E., and Hawkings, D. L. (1969). "Sound Generated by Turbulence and Surfaces in Arbitrary Motion," Philosophical Transactions of the Royal Society of London, Series A, Vol. 264, No. 1151, pp. 321-342.

6. Rosenstein, H., and Clark, R. (1983). "Aerodynamic Development of the V-22 Tilt Rotor," AIAA Aircraft Systems, Design and Technology Meeting, October 1983, Paper No. AIAA-86-2678.

7. McVeigh, M. A., Rosenstein, H., and McHugh, F. J. (1983). "Aerodynamic Design of the XV-15 Advanced Compositie Tilt Rotor Blade," 39th Annual Forum of the American Helicopter Society, May 1983.

8. Paisley, D. J. (1987). "Rotor Aerodynamics Optimization for High Speed Tiltrotors," Proceedings of the 43rd Annual Forum of the American Helicopter Society, May 1987.

9. McCroskey, W. J., Spalart, P. H., Laub, G. H., Maisel, M. D., and Maskew, B. (1983). "Airloads on Bluff Bodies, With Application to the Rotor-Induced Downloads on Tiltrotor Aircraft," Paper No. 11, Ninth Europpean Rotorcraft Forum, September 13-15, 1983.

10. Felker, F. F., Maisel, M. D., Betzina, M. D. (1985). "Full-Scale Tiltrotor Hover Performance," Proceedings of the 41st Annual Forum of the American Helicopter Society, Fort Worth, Texas, May 1985.

11. McVeigh, M. A. (1985). "The V-22 Tiltrotor Large-Scale Rotor Performance/Wing Download Test and Comparison with Theory," Proceedings of the 11th European Rotorcraft Forum, London, England, September 1985.

12. Clark, D. R., and McVeigh, M. A. (1985). "Analysis of the Wake Dynamics of a Typical Tiltrotor Configuration in Transition Flight," Proceedings of the 11th European Rotorcraft Forum, London, England, September 1985.

13. Felker, F. F. and Light, J. S. (1986). "Rotor/Wing Aerodynamic Interactions in Hover," Proceedings of the 42nd Annual Forum of the American Helicopter Society, Washington, D. C., June 2-4, 1986.

14. Rutherford, J. W., and Morse, H. A. (1985). "The Tilt Rotor Download Investigation," Videotape, U. S. Army Aeroflightdynamics Laboratory, 7 x 10 Wind Tunnel, Ames Research Center, July 1985.

15. Fejtek, I. and Roberts, L. (1991). "Navier-Stokes Computation of Wing/Rotor Interaction for a Tiltrotor in Hover," AIAA Paper 91-0707, Proceedings of the 29th Aerospace Sciences Meeting, Reno, Nevada, January 7-10, 1991.

16. Ordway, D. (1971). "SAI Bubble Generator: Description and Operating Instructions," Sage Action Inc., Ithaca, New York.

17. Hinze, J. O. (1975). Turbulence, McGraw-Hill Inc., New York. pp.105-111.

18. George, Albert. R., Smith, Charles A., Maisel, Martin D., and Brieger, John T. (1989). "Tilt Rotor Aircraft Aeroaacoustics," Proceedings of the 45th Annual Forum & Technology Display of the American Helicopter Society, Boston, Massachusetts, May 22-24, 1989.

19. Brentner, K. S. (1986). "Prediction of Helicopter Rotor Discrete Frequency Noise: A Computer Program Incorporating Realistic Blade Motions and Advanced Acoustic Formulation," NASA Technical Memorandum 87721.

20. Farassat, F. (1981). "Linear Acoustic Formulas for Calculation of Rotating Blade Noise," AIAA Journal, Vol. 19, No. 9, pp. 1122-1130.

21. Maisel, M. (1975). "Tilt Rotor Research Aircraft Familiarization Document," NASA Technical Memorandum X-62, 407.

22. Abbott, I. H., and Von Doenhoff, A. E. (1959). Theory of Wing Sections, Dover Publications Inc., New York.

23. Kuethe, A. M. and Chow, C. Y. (1986). Foundations of Aerodynamics, John Wiley & Sons Inc., New York. pp. 134-136.

24. Leishman, J. G., and Beddoes, T. S. (1986). "A Generalized Model for Airfoil Unsteady Aerodynamic Behaviour and Dynamic Stall Using the Indicial Method," Proceedings of the 45th Annual Forum of the American Helicopter Society, Washington D. C., June, 1986.

25. Leishman, J. G., and Beddoes, T. S. (1989). "A Semi-Empirical Model for Dynamic Stall," Journal of the American Helicopter Society, Vol. 34, No. 3, pp. 3-17.

26. Bronwell, A. (1953). Advanced Mathematics in Physics and Engineering, McGraw-Hill Book Company Inc., New York. pp. 432-434.

27. Amiet, R. K. (1976). "Noise Produced by Turbulent Flow into a Propeller or Helicopter Rotor," AIAA Paper 76-560

28. Amiet, R. K. (1989). "Noise Produced by a Turbulent Flow Into a Rotor: Theory Manual for Noise Calculation," NASA Contractor Report 181788.

29. Amiet, R. K., Egolf, C. G., and Simonich, J. C. (1989). "Noise Produced by a Turbulent Flow Into a Rotor: Users Manual for Noise Calculation," NASA Contractor Report 181790.

30. George, A. R., and Chou, S.-T. (1984). "Comparisons of Broadband Noise Mechanisms, Analyses, and Experiments on Rotors," Journal of Aircraft, Vol. 29, No. 9, pp. 407-420.

31. Lowson, M. V. (1965). "The Sound Field of Singularities in Motion", Proceedings of the Royal Society of London, Series A, Vol. 286, pp. 559-572.

32. Homicz, G. F., and George, A. R. (1974). "Broadband and Discrete Frequency Radiation from Subsonic Rotors," Journal of Sound and Vibration, Vol. 36, pp. 151-177.

33. George, A. R., and Kim, Y. N. (1977). "High-Frequency Broadband Rotor Noise," AIAA Journal, Vol. 15, No. 4, pp. 538-545.

34. LightHill, M. J. (1954). "On Sound Generated Aerodynamically I. General Theory," Proceedings of the Royal Society of London, Series A, Vol. 222, No. 1148, pp. 1-32

35. Johnson, H. K. and Katz, W. M. (1972). "Investigation of the Vortex Noise Produced by a Helicopter Rotor," USAA MRDL Technical Report 72-2.

36. Press, W. H., Flannery, B. P., Teukolsky, S. A., and Vetterling, W. T. (1989). Numerical Recipes, Cambridge University Press, Cambridge, pp.420-430.

37. Tennekes, H., and Lumley, J. L. (1972). A First Course in Turbulence, MIT Press, Cambridge, Massachusetts, pp. 248-256.

REPORT DOCUMENTATION PAGE

Form Approved
OMB No. 0704-0188

1. AGENCY USE ONLY *(Leave blank)*	2. REPORT DATE	3. REPORT TYPE AND DATES COVERED
	June 1992	Contractor Report

4. TITLE AND SUBTITLE

Tilt Rotor Hover Aeroacoustics

5. FUNDING NUMBERS

NAG-2-554

6. AUTHOR(S)

Charles David Coffen

7. PERFORMING ORGANIZATION NAME(S) AND ADDRESS(ES)

Cornell University
Ithaca, NY 14850

8. PERFORMING ORGANIZATION REPORT NUMBER

A-92143

9. SPONSORING/MONITORING AGENCY NAME(S) AND ADDRESS(ES)

Ames Research Center
Moffett Field, CA 94035-1000

10. SPONSORING/MONITORING AGENCY REPORT NUMBER

NASA CR-177598

11. SUPPLEMENTARY NOTES

Point of Contact: Marianne Mosher, Ames Research Center, MS T-042, Moffett Field, CA 94035-1000, (415) 604-4560 or FTS 464-4560

12a. DISTRIBUTION/AVAILABILITY STATEMENT

Unclassified-Unlimited
Subject Category – 71

12b. DISTRIBUTION CODE

13. ABSTRACT *(Maximum 200 words)*

This paper presents the methodology, results and conclusions of a study of tilt rotor hover aeroacoustics and aerodynamics.

Flow visualization and hot wire velocity measurements were performed on a 1/12-scale model of the XV-15 Tilt Rotor Aircraft in hover. The wing and fuselage below the rotor causes a complex recirculating flow. Results indicate the physical dimensions and details of the flow including the relative unsteadiness and turbulence characteristics of the flow.

Discrete frequency harmonic thickness and loading noise mechanism were predicted using WOPWOP for the standard metal blades and the Advanced Technology Blades. The recirculating flow created by the wing below the rotor is a primary sound mechanism for a hovering tilt rotor. The effects of dynamic blade response should be included for fountain flow conditions which produce impulsive blade loading.

Broadband noise mechanisms were studied using Amiet's method with azimuthally varying turbulence characteristics derived from the measurements. The recirculating fountain flow with high turbulence levels in the recirculating zone is the dominant source of broadband noise for a hovering rotor.

This study shows that tilt rotor hover aeroacoustic noise mechanisms are now understood. Noise predictions can be made based on reasonably accurate aerodynamic models developed here.

14. SUBJECT TERMS	15. NUMBER OF PAGES
Tilt rotor, Aeroacoustics, Aerodynamics, Acoustic measurements, Computer modeling	213
	16. PRICE CODE: A10

17. SECURITY CLASSIFICATION OF REPORT	18. SECURITY CLASSIFICATION OF THIS PAGE	19. SECURITY CLASSIFICATION OF ABSTRACT	20. LIMITATION OF ABSTRACT
Unclassified	Unclassified		

NSN 7540-01-280-5500

Standard Form 298 (Rev. 2-89)
Prescribed by ANSI Std. Z39-18
298-102

END DATE NOV 13, 1992